2010

Novel measurement based load modeling and demand side control methods for fault induced delayed voltage recovery mitigation

Hua Bai
Iowa State University

Recommended Citation

Bai, Hua, "Novel measurement based load modeling and demand side control methods for fault induced delayed voltage recovery mitigation" (2010). *Graduate Theses and Dissertations*. 11710.
https://lib.dr.iastate.edu/etd/11710

Novel measurement based load modeling and demand side control methods for fault induced delayed voltage recovery mitigation

by

Hua Bai

A dissertation submitted to the graduate faculty
in partial fulfillment of the requirements for the degree of
DOCTOR OF PHILOSOPHY

Major: Electrical Engineering

Program of Study Committee:
Venkataramana Ajjarapu, Major Professor
Chen-Ching Liu
Manimaran Govindarasu
Li-Zhi Wang
John R. Schroeter

Iowa State University
Ames, Iowa
2010

TABLE OF CONTENTS

LIST OF FIGURES

LIST OF TABLES

CHAPTER 1 INTRODUCTION

1.1 Power System Short-Term Voltage Stability

Power system voltage stability is concerned with the ability of a system to maintain acceptable voltages throughout the system under normal and contingent conditions [1]. Voltage collapse is typically associated with the reactive power demands of loads not being met because of limitations on the production and transmission of reactive power. Limitations on the production of reactive power include generator and SVC reactive power limits and the reduced reactive power production by capacitors at low voltages. The primary limitations on the transmission of power are the high reactive power loss on heavily loaded lines, as well as possible line outages that reduce transmission capacity. Reactive power demands of loads increase with load increases (examples include additional motor load and increased air conditioning use with increasing temperature), changes in voltage, motor stalling, or changes in load composition. It has long been known that the representation of loads can significantly impact power system simulation results. The voltage and frequency dependence of a power system load greatly affects its dynamic behavior, including small-disturbance stability, transient stability, oscillation damping, and voltage stability.

During large disturbances the transmission system voltage can fall below a critical threshold, resulting in induction motors dropping out (control devices disconnecting the motors) or motor stalling. Voltage collapse can occur when stalled motors remain connected to the system, or motors previously disconnected are automatically reconnected causing a large, mostly reactive, starting current. Furthermore, motors at power plants can drop out or stall upon low voltage, thus leading to tripping of generators as well. Such a disturbance is classified as a short-term voltage instability phenomenon, with a time frame in the order of seconds [1].

A typical short-term voltage instability scenario would be a fault resulting in a significant, momentary drop in voltage. Motors can react to the voltage drop in several ways depending on several factors, such as the type of motor, the type of load, and the motor controls. Residential window air conditioning units typically have very simple controls. Thus, if the voltage drops and reduces the electrical torque below the mechanical load torque, the motor may stall, and eventually be disconnected by the motor thermal overload. Residential split system air conditioners usually have contactors to control the compressor motor. On low voltage, the contactor will usually disconnect the motor before it stalls. However, once the fault is cleared and voltage is restored, the contactor may close to restart the motor. The starting motor has a highly reactive inrush current, typically 4 to 6 times full load. The high reactive power demands from motors in starting conditions may cause short-term voltage stability problem or even voltage cascading if the system is already close to its maximum reactive power limit. Air conditioners with mechanical thermostats are most likely to restart immediately upon restoration of voltage. Air conditioners with electronic thermostats often have a time delay that will postpone restarting the compressor motor after voltage is restored for, typically, 5 minutes [39].

Factors such as increased use of low inertia compressor motors, air conditioning, heat pumps, and refrigeration, increased use of voltage-insensitive power electronic loads, and increased use of capacitor banks for reactive compensation, and more intensive use of transmission systems, are increasing the likelihood of short-term voltage instability [2]. Because of the load model uncertainties and impact of dynamic load behavior on critical system characteristics, the short-term voltage instability phenomenon must be studied by examining the dynamic interactions between the loads and the power grid. Although the industry has made great strides in investigating the related phenomena, there is still a great deal of work to be done in the areas of aggregate load modeling, understanding short-term voltage instability mechanism and developing mitigation methods against voltage instability.

1.2 Power System Load Modeling

Dynamic load behavior under severe system contingencies could drive power system to voltage collapse. Accurate load modeling can avoid costly system design miscalculations and erroneous system operations [3] – [7]. It is important to have accurate load model parameters which influence critical system characteristics, such as damping [8] and voltage stability limits. Different load models may cause completely contrary conclusions on system stability [9] [10]. It is reported that using “standard” load parameters, the load model could not replicate the unstable behavior for a fault event reconstruction [5]. However, exhaustive investigations illustrated that the correct behavior could be predicted by altering load parameters by small amounts.

1.2.1 *Difficulty of Aggregate Load Modeling*

An extensive literature is available for identifying load model parameters [12]. However, obtaining accurate aggregate load models is very complicated due to the following issues:

- Loads are time variant and stochastic
- Issues related to aggregate loads
  - Large number of diverse load components
  - New load components penetration into the system
  - Lack precise composition information for certain loads
  - Level of details to represent various load components
- Load models must be verified with actual measurements

The latter two are due to the large number and types of loads connected at the transmission system level, which makes the consideration of each separate load numerically impractical and provides no insight into the bulk power system analysis.

Regarding the first issue, it is known that the load in real time system is time variant. Not only individual load percentages will change from time to time, other parameters of the aggregate load will also change in practical systems. Large amount of real time field measurement data are needed to capture the time variant characteristic of load. However, even with enough real time load measurement data, it is still difficult to capture the time variant characteristic with measurement-based load modeling methods. Measurement-based method applies multi-samples of the measurement to optimize the load parameters and derive the optimal parameter set that minimizes the load model output error. Actually, the measurement-based method is not mainly used to deal with the time variant characteristic of power system load. Instead, it is mainly used to accurately adjust the parameters of load model given the real time load measurement data. The derived load model by measurement-based approach is usually incorporated in the system models to conduct time domain simulation for system dynamic analysis. Since the measurement based load model has more accurate load parameters, the system stability margin calculation and other system stability related information can be obtained more accurately and the system dynamic stability study results will be more reliable.

Because the time interval of the load measurement data used for load parameter identification is from 1s to 10s, the measurement-based method generally assumes the load characteristics do not change during the time interval that measurements were taken. In our load modeling process, we assume the percentages of dynamic load and static load keep constant during the period that measurement data was recorded.

1.2.2 *Motivation for Aggregate Load Modeling*

Recently, load modeling improvement is required by the fact that high percentages of air conditioner load are increasing in some areas. The unique characteristics of air conditioner load could cause short-term voltage instability, fast voltage collapse, and delayed voltage recovery. Examples include the voltage collapse incidents occurred in Southern California Edison (SCE) and Florida Power & Light Company [11]. High load currents and reactive power demands by air conditioner loads caused delays up to 30 seconds for voltage to recover following a fault clearing operation.

As load characteristics change from traditional incandescent light bulbs to power electronics-based loads, and as the characteristics of motors change with the emergence of high-efficiency, low-inertia motor loads, it is critical to understand and model load responses to ensure stable operations of the power system during different contingencies. Developing "better" load models, therefore, has been an important issue for power system analysis and control. It is necessary to take advantage of the state-of-the-art techniques for load modeling and develop a systematic approach to establish accurate, aggregate load models for bulk power system stability studies.

1.3 Fault Induced Delayed Voltage Recovery

Recently, “Workshop on Residential Air Conditioner (A/C) Stalling” of Department of Energy (DOE) reported that fault-induced delayed voltage recovery is now a national issue since residential A/C penetration across U.S. is at an all time high and growing rapidly [37].

Various studies have shown that FIDVR usually occurs in the areas dominated by induction motors with constant torque. These motors can stall in response to sustained low voltage and draw excessive reactive power from the power grid [39]-[42]. Since no under voltage or stall protection is equipped with A/Cs, they can only be tripped by thermal protection which takes 3 to 20 seconds. Severe FIDVR event could lead to fast voltage collapse.

1.3.1 *NERC’s Definition of FIDVR*

According to NERC’s definition [38], FIDVR is defined as the phenomenon whereby system voltage remains at significantly reduced levels for several seconds after a fault in transmission, subtransmission, or distribution has been cleared.

1.3.2 *Existing Events of FIDVR*

FIDVR has occurred in many utilities across U.S. and one severe case happened following a fault cleared in as little as 3 cycles [38]. Fig. 1-1 shows a FIDVR event on July 13, 2004 at Devers Substation of Southern California Edison (SCE) [11]. In this incident, high load currents and large reactive power demands caused delay up to 30 seconds for voltage to recover after a fault clearing.

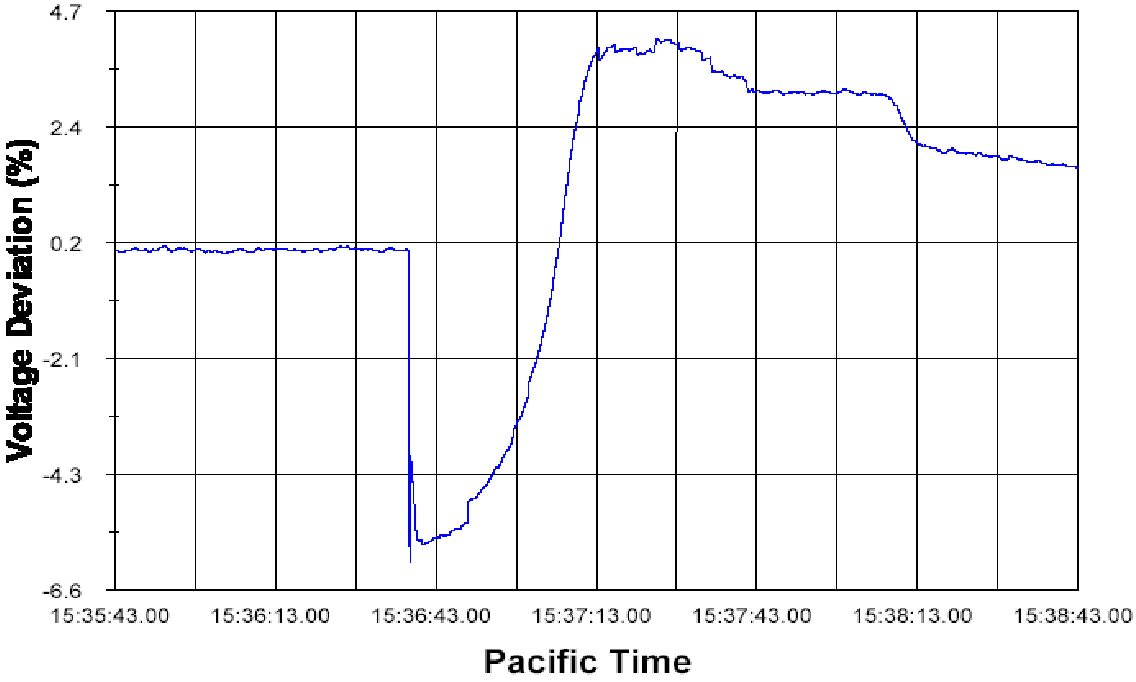

Fig. 1-1. Delayed voltage recovery on July 13, 2004 at Devers Substation

Some typical FIDVR events are summarized as follows [38].

- *FIDVR Event in Florida Power and Light Company (FPL) on August 18, 1988.*

A bolted 3-phase fault at the Flagami 230-kV switchyard initiated the event. Although the fault was cleared in 3.5 cycles, approximately 825 MW of load was disconnected in the Miami area, almost all due to customer equipment protection. Area voltage was depressed for ten seconds after fault isolation.

- *Multiple FIDVR Events in Southern California Edison (SCE) since 1988.*

  First FIDVR event in SCE was observed in 1988. At least 53 subsequent events have occurred. Especially, multiple FIDVR events occurred in SCE’s desert regions during the peak air-conditioning period, including a major incident in June, 1990, which affected a 1000 square mile area of Riverside County.

- *First FIDVR Event in Southern Balancing Authority on July 30, 1999.*

  A bus work in the Union City 230kV substation (Metro Atlanta) initiated an event that included three separate faults and two breaker failure operations. As a result, delayed voltage recovery of up to 15 seconds was observed over a large portion of North Georgia. 1900 MW of load and seven small generating units were tripped. This event showed that the local transmission system had evolved to a state where FIDVR events are possible.

- *FIDVR Event in Egypt.*

  In 1990, “Voltage Instabilities Subsequent to Short-circuit Recoveries,” was submitted by M. Z. El-Sader, a faculty member of the Electrical Engineering Department of Assuit University, Assuit (Egypt). Clearly, FIDVR was a concern beyond North America – reaching across the globe to areas of high induction motor load penetration.

CHAPTER 2 LITERATURE REVIEW AND SCOPE OF THE WORK

2.1 Literature Review

2.1.1 *Measurement based Load Modeling*

Load modeling methods can be classified into two categories: component-based approach [13] and measurement-based approach which gives a closer look at the real-time loads and their dynamic characteristics [14].

Theoretical foundation of measurement-based approach is system identification. Identification techniques are well established for linear models. However, modeling and identification of nonlinear dynamic system are challenging tasks, since nonlinear processes are unique in the sense that they do not share many properties. A major goal for any nonlinear system modeling and identification scheme is the capability of describing a wide class of structurally different systems.

Nonlinear system identification problems generally have the following properties [15]:

- Many local optima exist,
- The surface in the neighborhood of a local optimum can be approximated by a hyperparabola,
- No analytic solution exists,
- An iterative algorithm is required,
- They can hardly be applied online.

Nonlinear global optimization problems, which are more complex than the nonlinear local optimization problems, typically fulfill one or more of the following properties [15]: multi-modal, non-continuous derivatives of the loss function, non-continuous parameters, and structure optimization problems. All nonlinear global optimization methods require some tradeoff between the extent of the global character and the convergence speed. No method can guarantee to find the global solution for complex practical applications (in finite time).

In the power system load modeling field, there are three kinds of approaches for nonlinear system identifications:

1. *Analytical based approach* – Analytical based approach derives parameters determinately according to test results. In 1977, Dr. Shackshaft et al. made a series of field tests and proposed a simple method for deriving the parameters of a simplified induction motor load model [16]. This kind of approach can be used in a special test such as step/staged/controlled test. However, it is extremely sensitive to measurement error.
2. *Optimization based approach* – The main procedure of an optimization based approach is to search the best parameters, which minimizes an error function between the measured output variables and simulated ones. Search algorithms have been applied in this type of approach. Examples of these search algorithms include:
   - Search algorithms using statistical techniques:
     - Least Square Based Parameter Estimation [17]
     - Weighted Least Square Based Parameter Estimation [18]
     - Instrumental Variable Based Parameter Estimation [21]

    - Maximum Likelihood Based Parameter Estimation [22]
    - Gradient Based Parameter Estimation [23]
  - Search algorithms using heuristic techniques:
    - Simulated Annealing Based Parameter Estimation [19]
    - Neural Network Based Parameter Estimation [26]
    - Genetic Algorithm Based Parameter Estimation [28]

3. *Stochastic Based Approach* – These approaches are limited to assumptions of the error function [27].

Reference [17] used least square method to find parameters of induction motor models. Reference [18] applied weighted least square method to derive load parameters. Weighted least square was used to solve the problem of unequal variances of errors. It weighed each observation based on its variability. Thus, high variability effects can be reduced. Difficulty of this method is to find proper weights. Weighted least-square also increases the complexity of the algorithm.

Reference [19] used the adaptive simulated annealing to identify load parameters. Reference [20] proposed a multistage algorithm for load parameter identifications. The above two references applied the input-output parametric model as the load model which is not physical based. The model parameters could vary dramatically during different fault conditions and system configurations. It is difficult to constrain the parameters.

Reference [21] applied the Instrumental Variable (IV) algorithm and the Minimization of Sum of Absolute Residues (MSAR) algorithm to identify load parameters. These two algorithms are suitable for linear problems or those that can be converted to linear problems.

Since it is difficult to convert the nonlinear aggregate load model to linear models, these two algorithms are not appropriate for aggregate load modeling.

Reference [22] applied maximum likelihood identification scheme for load modeling. In the maximum likelihood method, a likelihood function must be defined and this usually requires knowledge of the probability density function of observations. Computation for this method is rather complex.

Reference [23] applied the gradient based method which could give erroneous parameter estimates since it is possible to be trapped in one local solution depending on the initial guess. Reference [24] reported that gradients based methods could not deal well with problems of local minima and data pollution. They tend to diverge when applied for real systems.

Reference [25] showed that the nonlinear parameters were calculated straightforward from the linear identification results. However, the basic assumption of this approach is that large disturbances do not affect the system. However, this assumption can hardly be true for practical power systems.

Artificial Neural Network (ANN) [26] based load modeling can use measurements to train and update models adaptively. It does not need the pre-defined load model structure and the load composition information. However, it has several shortcomings such as difficult to set learning parameters, slow convergence rate and training failures due to local minima, etc.

Reference [28] demonstrated the suitability of applying GA for the aggregate load modeling. One of the main obstacles in applying GA to complex problems has often been the high computational cost. Many efforts have been devoted to improve GA for load modeling, such as, population diversity based GA (PDGA) [29], adaptively adjusted GA [30]. However, the main reason of GA’s slower convergence rate than that of local search techniques (e.g., steepest descent) is that it does not use much local information to determine the most promising search direction. Consequently, a GA explores a wider frontier in the search space in a less directional fashion. An effective strategy to make use of GA’s global search abilities is to combine GA with a complementary local search technique. Because of GA, the hybrid approach is less likely to be trapped in a local optimum than a pure local search technique is. Due to its local search, the hybrid approach often converges faster than the pure GA does. Generally, the hybrid approach can explore a better trader-off between computational cost and the global optimality of the solution found. Searching in the open sources of load modeling methods, hybrid methods that combine GA with a local search technique were not found.

2.1.2 *Mitigation Methods for FIDVR*

To mitigate FIDVR events, two categories of efforts have been mainly devoted: one effort focuses on improving the load modeling of A/C motors to capture and study FIDVR [43]-[47]; another effort is dedicated to develop control solutions to reduce the impacts of FIDVR [48]-[55]. Control solutions can be classified as supply-side solutions and demand-side solutions. The most popular supply-side solution applied by utilities is the implementation of FACTS devices including SVC [51]-[54] and STATCON [55] to increase reactive power support. However, these devices are very expensive and cost approximately \$20-50 million per installation. Since a large number of these devices would have to be installed, it could be very costly. Furthermore, it has been reported that FACTS devices may not be fully effective in preventing the extremely fast voltage collapse following a transmission fault [37].

Demand-side solutions that use protection system to rapidly disconnect motors under low voltage conditions are effective and economic to tackle FIDVR [37]. In [48], a slope-permissive under-voltage load shed relay was proposed based on rate of voltage recovery and predicted time to recover. In [49], a MVA-Volt index was proposed for steady-state screening of buses to identify FIDVR. SCE recently proposed an under voltage protection scheme using a 78% of the motor rated voltage as the stalling protection threshold voltage to tackle FIDVR [50]. The above three methods are representatives of demand-side solutions developed so far to solve FIDVR (based on available literature in open sources).

2.2 Scope of Work and Objectives

The research presented in this dissertation is directed towards:

1. Providing a systematic methodology to derive aggregate load models at the high voltage level (transmission system level) using measurement-based approach.
2. Developing a novel parameter identification technique via hybrid learning for deriving load model parameters accurately and efficiently.
3. Revealing the mechanism of fault-induced delayed voltage recovery by analyzing stalling characteristics of induction motors and relationship between FIDVR and motor kinetic energy.
4. Developing a derivation method of equivalent motor speed for online evaluation of motor stalling status.

5. Developing a novel online demand side control method for disconnecting stalling motors at the transmission level to mitigate FIDVR and fast voltage collapse.

2.3 Organization of This Dissertation

The rest of the dissertation is organized as follows.

In Chapter 3, a systematic methodology for aggregate load modeling is presented. The systematic methodology includes selection of aggregate load modeling structure, load parameter identification and analysis of the load parameter search space. The introduction and comparison of the two traditional load modeling methods are also provided.

In Chapter 4, a novel parameter identification technique, hybrid learning algorithm, is proposed for deriving load parameters. The two main procedures and the overall picture of the algorithm are presented. Validation of the proposed technique is done using both simulation data and field measurement data.

In Chapter 5, the static modeling and *P*-*S* and *Q*-*V* characteristics of induction motor are provided to investigate the FIDVR mechanism. Based on the analysis, the motor kinetic energy is proposed to tackle the FIDVR problem and a method using online measurement is provided for motor kinetic energy derivation.

In Chapter 6, an online demand side control strategy making use of the motor kinetic energy is proposed to disconnect the stalling motors at the transmission level. Validations of the proposed methodology are provided to show its effectiveness. The traditional UVLS is also applied to tackle the FIDVR problem as a comparison.

In Chapter 7, several issues regarding the practical implementation of the proposed online demand side control for FIDVR mitigation are tackled and discussed. It includes the study of incorporating UVLS relay in large induction motors, practical implementation of the proposed method to large power systems and comparison with traditional UVLS scheme.

The conclusion and further research direction are presented in chapter 8.

CHAPTER 3 POWER SYSTEM AGGREGATE LOAD MODELING

3.1 *Introduction*

Load characteristics have long been known to have a critical effect on system performance, and voltage stability results are known to be highly dependent upon the load models applied. In order to derive dependable voltage stability study results, it is desired to develop more accurate load models which will be used in power system simulation programs.

In this chapter, a systematic methodology for aggregate load modeling is presented. The systematic methodology includes selection of aggregate load modeling structure, load parameter identification and analysis of the load parameter search space. The introduction and comparison of the two traditional load modeling methods are also provided.

3.2 *Aggregate Load Modeling Methods*

3.2.1 *Component Based Method*

A component based approach involves building up the load model from information on its constituent parts [7]. The load supplied at a bulk power delivery point is categorized into load classes such as residential, commercial, industrial, agricultural, and mining. Each load class is represented in terms of load components such as lighting, air conditioning, space heating, water heating, and refrigeration. The characteristics of individual component have been studied in detail and typical data have been developed for load composition and characteristics for each class of load. Techniques have been developed to aggregate individual component to produce a composite load model.

The challenge in component based approach is in collecting and aggregating the load components into a model that is appropriate for system simulations. Only in relatively rare cases is the load composition known to a high degree of confidence such as the auxiliary load in a power plant. Furthermore, the interaction of various load components during the transient and extended term period following a disturbance is not captured in the component based approach, since each component is treated independently of each other. For example, the impact of motors stalling and re-starting over the course of a transient introduces voltage fluctuations that affect the response of other load components. The resultant dynamic characteristic is a combination of responses of the various components, not necessarily equal to the sum of their contributions.

3.2.2 *Measurement Based Method*

Measurement based load modeling approach takes use of measurement data obtained from various system locations to develop the aggregate load models. Generally, measurement based method includes three steps for load modeling: load model structure selection, load parameter identification and load model validation. Among the three steps, the identification of load parameters is the most critical task for accurate load modeling.

Load parameter identification can be defined as a process aimed at extracting a set of parameters which is able to accurately represent the relationship between input variables and output variables. The objective function for load parameter identification is usually defined as the minimization of the difference between load model outputs and load measurements.

For measurement based load modeling, the input variables are the measured voltage and frequency and the output variables are the estimated load real power and reactive power. The overall procedure of measurement based load modeling is that measured voltage is imported to actual load and load model to obtain actual measured powers and estimated power outputs. Objective function is then calculated to evaluate whether the load model accuracy criterion is satisfied. If not, optimization technique will be applied to optimize the load parameters and update the load model. This procedure is repeated until the load model accuracy is satisfactory and the corresponding parameters are considered as the optimal set of load parameters.

The advantage of measurement based load modeling method is that it directly measures the actual load behavior during system disturbances and the direct measurement data is used to derive accurate load model parameters which can be conveniently applied in power system simulation programs. In the absence of precise information about a power system load, one of the most reliable ways to obtain an accurate load model is to apply the measurement-based approach. If field measurement data are available which adequately describe the load behavior, a dynamic and/or static equivalent of the load can be obtained by analyzing functional relationships between these quantities using parameter identification techniques.

Measurement based load modeling method also has some shortcomings. When recording field measurement data, it is often necessary to monitor the system for a long time to consider different variations in system configurations and load patterns. To obtain a better load model, we need measurement data recorded during large disturbance that can lead to significant changes of voltage and frequency. However the large disturbances are rare events in practical power systems. Hence, it could be difficult to identify and develop “generic” parameters that must be used for dynamic and transient studies with a small set of measurements from these rare events.

3.3 Aggregate Load Model Structure

Different load model structures may make stability study results totally different or even ambivalent [31]. Static loads can be represented in term of either a polynomial expression (ZIP) or an exponential form. Dynamic loads can be represented in term of either an induction motor model (differential equation based) or an input-output model (difference equation based). Aggregate load model is the combination of static load model and dynamic load model. There are four model structures for aggregate load model:

- ZIP augmented with Induction Motor (3-state)
- ZIP augmented with Difference Equation (2nd order)
- Exponential augmented with Induction Motor (3-state)
- Exponential augmented with Difference Equation (2nd order)

However, for a specific set of measurement data, one model structure may be better than the others. It is also true that one model structure that gives the best results for one set of measurement data may not be the best model structure for a different set of measurement data. In this research, ZIP augmented with induction motor is selected as the load model structure. The frequency dependent part of the load is ignored. Aggregate load model can be generally presented as follows,

$$\begin{cases} P_s = \alpha_1 * P_{ZIP} + \beta_1 * P_{MOT} \\ Q_s = \alpha_2 * Q_{ZIP} + \beta_2 * Q_{MOT} \end{cases} \tag{3.1}$$

where P_s, P_{ZIP} and P_{MOT} represent the real power of aggregate load, ZIP load and induction motor load; α and β are static and dynamic load percentages.

The ZIP model is expressed as follows,

$$\begin{cases} P_{ZIP} = P_0[a_p(\frac{V}{V_0})^2 + b_p(\frac{V}{V_0}) + c_P] \\ Q_{ZIP} = Q_0[a_q(\frac{V}{V_0})^2 + b_q(\frac{V}{V_0}) + c_q] \end{cases} \tag{3.2}$$

where P_0 and Q_0 represent the real and reactive load power in the steady state; $a_P + b_P + c_P = 1$ and $a_q + b_q + c_q = 1$.

The induction motor static model is shown as Fig. 3-1, where R_s is the stator resistance; X_s is the stator leakage reactance; X_m is the magnetizing reactance; X_r is the rotor leakage reactance R_r is rotor resistance; $s = (\omega_s - \omega)/\omega_s$ is the rotor slip.

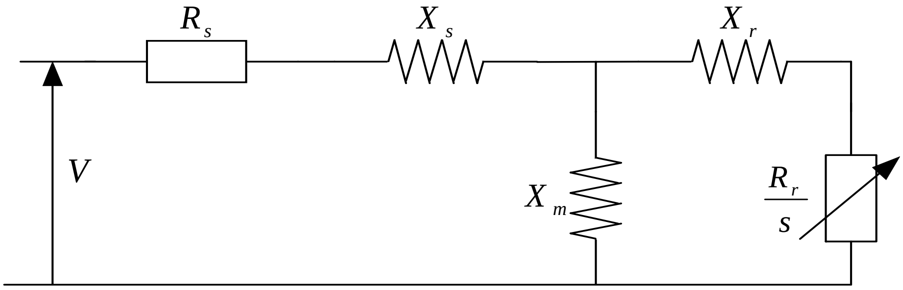

Fig. 3-1. Static model of induction motor

The mathematical formulation of induction motor model can be described as follows [7],

$$\begin{cases} \dfrac{dE_d^{'}}{dt} = -\dfrac{1}{T^{'}}\left[E_d^{'} + \left(X - X^{'}\right)I_q\right] - (\omega - 1)E_q^{'} \\ \dfrac{dE_q^{'}}{dt} = -\dfrac{1}{T^{'}}\left[E_q^{'} - \left(X - X^{'}\right)I_d\right] + (\omega - 1)E_d^{'} \\ \dfrac{d\omega}{dt} = -\dfrac{1}{2H}\left[T_0(A\omega^2 + B\omega + C + D\omega^E) - \left(E_d^{'}I_d + E_q^{'}I_q\right)\right] \end{cases} \tag{3.3}$$

$$\begin{cases} I_d = \dfrac{1}{R_s^2 + X^{'2}}\left[R_s\left(U_d - E_d^{'}\right) + X^{'}\left(U_q - E_q^{'}\right)\right] \\ I_q = \dfrac{1}{R_s^2 + X^{'2}}\left[R_s\left(U_q - E_q^{'}\right) - X^{'}\left(U_d - E_d^{'}\right)\right] \end{cases} \tag{3.4}$$

Load torque equation is expressed as,

$$T_L = T_0(A\omega^2 + B\omega + C + D\omega^E) \tag{3.5}$$

where $X^{'}=X_s+\left(X_mX_r\right)/\left(X_m+X_r\right)$ is the transient reactance and is equal to the blocked-rotor (short-circuit) reactance, $X=X_s+X_m$ is the motor no-load (open-circuit) reactance and $T^{'}=\left(X_r+X_m\right)/\left(\omega_sR_r\right)$ is the transient open-circuit time constant; H is rotor inertia constant; T_0 is steady state mechanical torque; ω is rotor rotation speed; $E_d^{'}$ and $E_q^{'}$ are d-axis and q-axis transient EMF of motor; U_d and U_q are d-axis and q-axis bus voltage, I_d and I_q are d-axis and q-axis stator currents; A, B, C, D, E are coefficients in load torque equation in terms of motor rotation speed, and satisfy $C=1-A\omega_0^2-B\omega_0-D\omega_0^E$.

In addition to accurately model individual load, it is critical to determine the percentages of each individual load in the aggregate load. This was recognized in a study conducted for the model validation and analysis of WSCC system oscillations on August 4, 2000 [32]. Fig. 3-2 shows the bus voltage oscillations of a 500kV bus in the WSCC system with different percentages of induction motors. The study suggests increasing percentages of induction motors in selected areas for system stability studies.

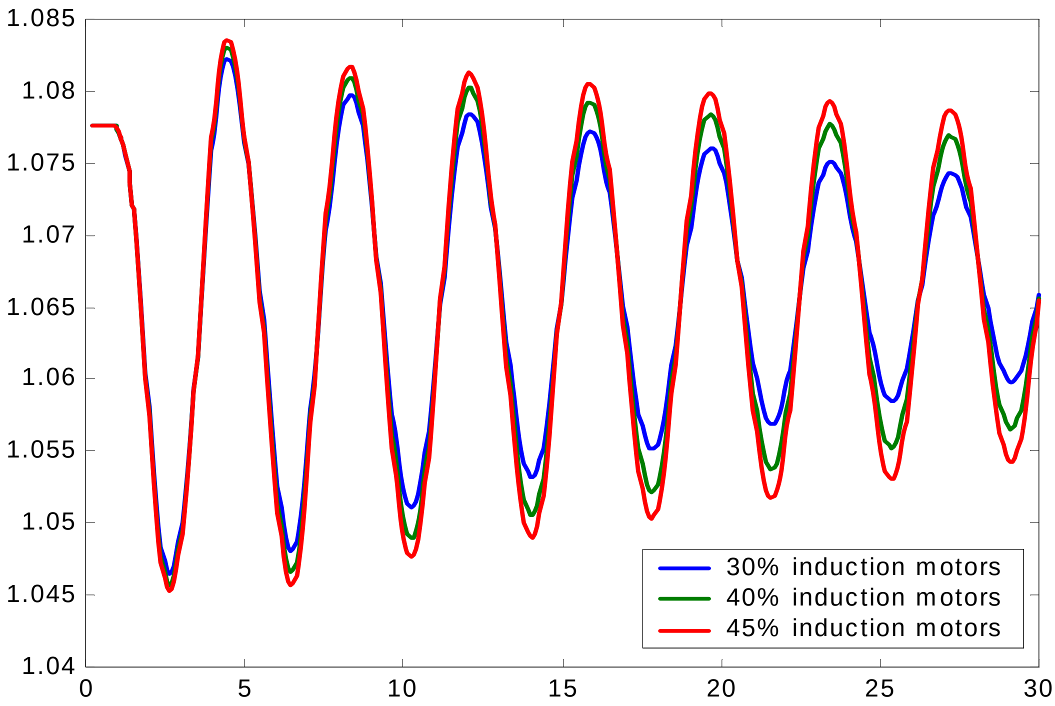

Fig. 3-2. Impact of induction motors on system oscillation

3.4 Load Parameter Identification

Load parameters are classified as: dependent parameters: $\beta_1, \beta_2, c_p, c_q, C$; independent parameters: $\alpha_1, \alpha_2, a_p, b_p, a_q, b_q, R_s, X_s, X_m, R_r, X_r, H, A, B, D, E$, summarized in Table 3-1.

Objective function for parameter identification is defined as the difference between load model outputs and measurements. The mathematical formulation is as follows,

$$\min \frac{1}{n}\sum_{k=1}^{n} \varepsilon_k^2(\theta) = \min \frac{1}{n}\sum_{k=1}^{n} [(P_{km}(\theta) - P_{ks}(\theta))^2 + (Q_{km}(\theta) - Q_{ks}(\theta))^2] \tag{3.6}$$

where $P_{km}(Q_{km})$ and $P_{ks}(Q_{ks})$ are measured and simulated power; θ represents independent parameters; $\varepsilon(\theta)$ represents the load model output error.

Table 3-1. Parameters to be derived for the aggregate load model

Load Model Structure	Parameters to be Derived
$\alpha * (ZIP) +$ $\beta * (Induction\ \ Motor)$	Load composition: $\alpha_1, \alpha_2, \beta_1, \beta_2$ ZIP model: $a_p, b_p, c_p, a_q, b_q, c_q$ Induction motor model: $R_s, X_s, R_r, X_r, X_m, H, A, B, C, D, E$

Load parameter identification is aimed to find load model parameters that results in the best fit between measurement samples and load model outputs. Fig. 3-3 is the procedure for load parameter identification. Measured voltage is the input to actual load and load model to derive output powers. Objective function is then calculated to evaluate whether the accuracy criterion is satisfied. If not, optimization algorithm is applied to optimize the load parameters and update the load model.

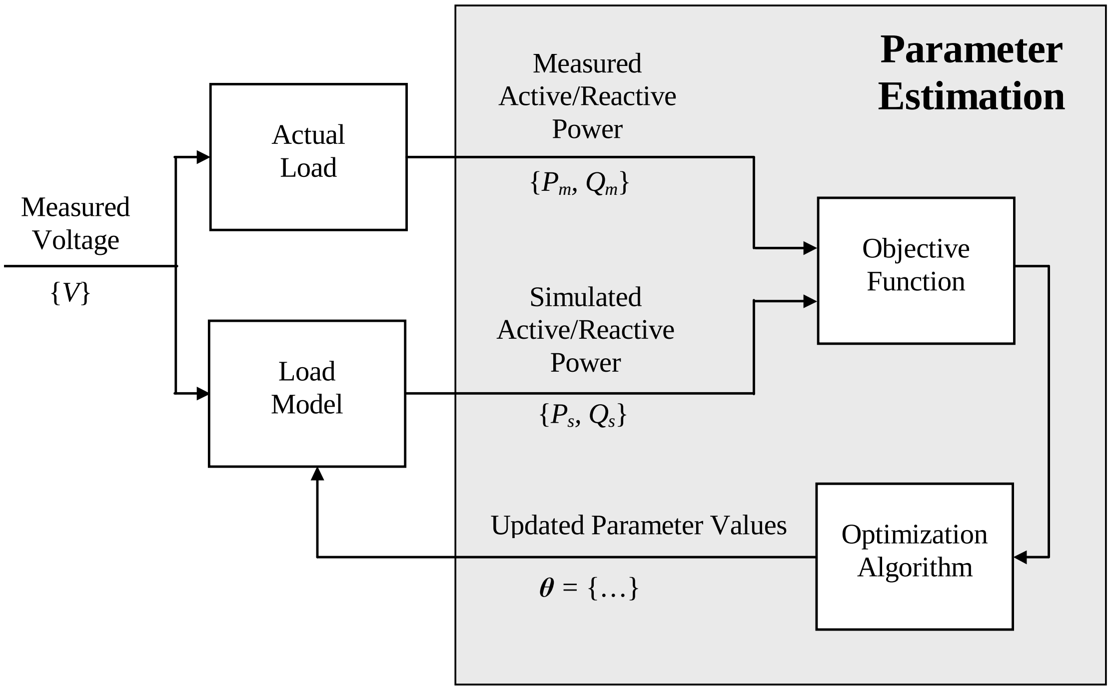

Fig. 3-3. Procedure for the load parameter identification

3.5 Load Parameter Search Space Analysis

In numerical search for load model parameters, a list of possible solutions is searched in order to locate the solution that minimizes the objective function. If two load parameters, R_r and X_r are selected, one could try a large number of combinations, calculate the objective function value $\varepsilon(\theta)$ and produce a surface plot with R_r, X_r and $\varepsilon(\theta)$ (Fig. 3-4). Such a plot is a representation of the load parameter search space which can be of very complex topography. Figs. 3-4 and 3-5 illustrate that the load parameter search space could have numerous peaks of varying heights, separated from each other by valleys on all scales. The lowest minimum is referred to as the global optimum, the lesser minima as local optima.

In general, finding the "correct" load model parameters is difficult partly due to the existence of many local optima in a multidimensional search space.

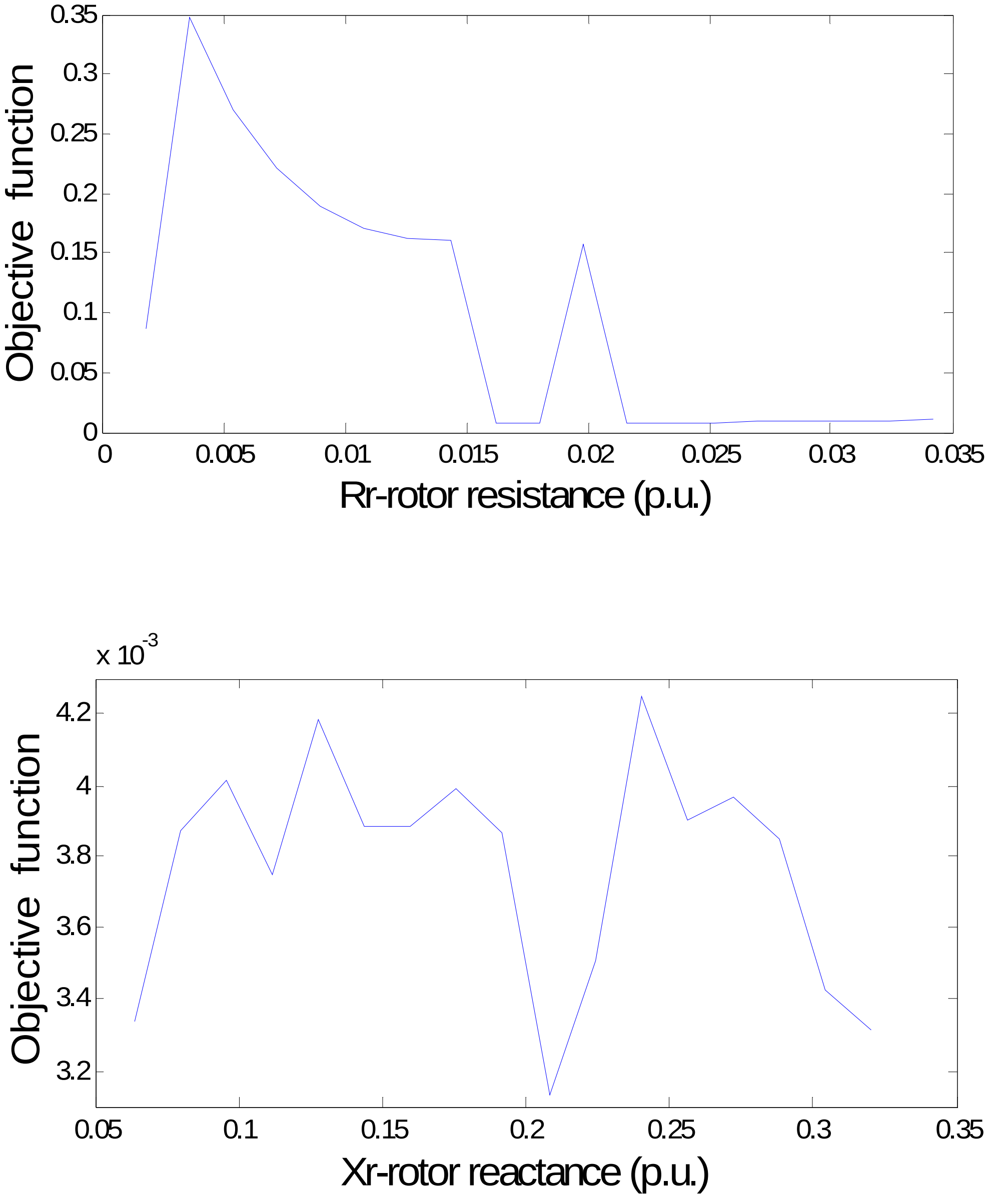

Fig. 3-4. Nonlinear relationships between load parameters R_r , X_r and $\varepsilon(\theta)$

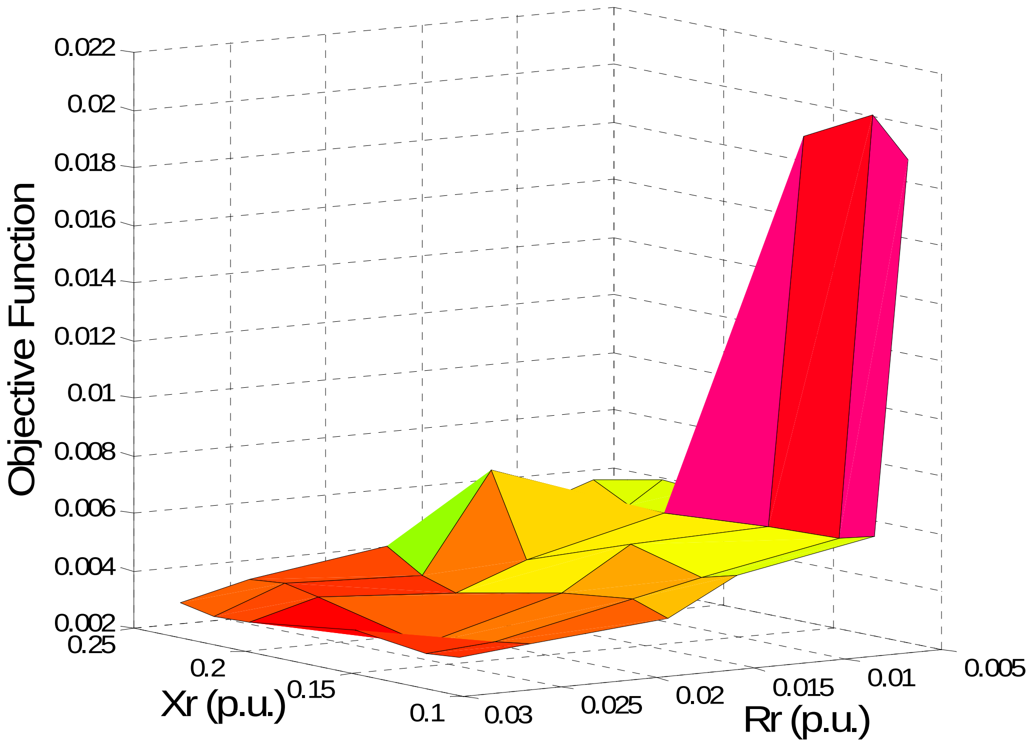

Fig. 3-5. Load parameter search space with R_r, X_r and $\varepsilon(\theta)$

CHAPTER 4 HYBRID LEARNING ALGORITHM

4.1 Introduction

In this chapter, a novel parameter identification technique, hybrid learning algorithm, is proposed for deriving load parameters. First of all, an overview of hybrid learning algorithm is provided. It includes the motivation for coming up with the hybrid approach and the traditional two procedures for combining global search and local search. Then, the details and overall steps of hybrid learning algorithm are presented. Validation of the proposed algorithm is conducted using both simulation data and field measurement data.

4.2 Hybrid Learning Algorithm Overview

Hybrid learning algorithm combines the genetic algorithm and the nonlinear Levenberg–Marquardt algorithm. Because of the stochastic nature, GA can quickly steer their searches within the region close to the true optimum. However, converging to the exact optimum may be best achieved if a local search technique is used for the solution obtained by GA [33]. The hybrid learning algorithm takes advantages of the global search ability of GA and the local search ability of Levenberg–Marquardt algorithm, which is a more powerful search technique. The most important issues when designing a hybrid learning algorithm include the choice of GA model, the way of incorporating local search into GA, and the balance between global search and local search [34].

Two procedures are mainly used to combine GA with local search: 1) use local search during GA generations, 2) use local search at the end of a GA run. In the first procedure, parent population is operated by the usual genetic operations and then followed by local search to create the new population. In the second procedure, local search is applied to solutions obtained by the complete run of a GA. According to reference [35], it is likely to have a lesser computational cost for the second procedure, which is applied in this dissertation to design the hybrid learning algorithm.

In the following subsections, details of the global search and local search of the proposed algorithm are provided.

4.3 Global Search of Hybrid Learning Algorithm

1) Problem Representation: In the problem, each load parameter is coded in a binary substring. All substrings are concatenated into a full string. Every string in the population corresponds to a set of load parameters.

2) Elitist Strategy: A common selection operator is the fitness-proportional selection. With this approach the probability of selection is proportional to an individual's fitness. However, fitness-proportional selection does not guarantee the selection of any particular individual, including the fittest. Unless the fittest individual is much, much fitter than any other, it will occasionally not be selected. Thus with fitness-proportional selection the best solution discovered so far can be regularly thrown away. To overcome this drawback, the elitist strategy is applied which requires that the fittest individual is selected and a copy of it is not disrupted by crossover or mutation.

3) Adaptive Crossover and Mutation Rates: Crossover and mutation rates have great impacts on the performance of a GA. Crossover provides a method whereby information for differing solutions can be melded to allow the exploration of new areas in the search space. Mutation is used to ensure that the population maintains both possible bit values (0 and 1) at all loci. During later stages of the run, when hopefully the majority of the population is in the vicinity of the global optimum, there might be advantages in confining crossover and mutation to lower rates. Conversely, during earlier stages, crossover and mutation with higher rates will help in the full exploration of the search space. Therefore, we apply the adaptive crossover and mutation rates.

When $(f_{\max} - f_{avg}) / f_{avg} > k$, where k is a constant; $f_{\max}$ and f_{avg} are the maximum and average fitness values, generation is in the early stage. Thus, larger rates of crossover and mutation are applied. The crossover rate P_c and mutation rate P_m are chosen as follows, where P_{c0} and P_{m0} are their initial values.

$$\begin{cases} P_c = P_{c0} \times e^{(\frac{f_{\max} - f_{avg}}{f_{avg}} - k)/(\frac{f_{\max} - f_{avg}}{f_{avg}})} \\ P_m = P_{m0} \times e^{(\frac{f_{\max} - f_{avg}}{f_{avg}} - k)/(\frac{f_{\max} - f_{avg}}{f_{avg}})} \end{cases} \tag{4.1}$$

When $(f_{\max} - f_{avg}) / f_{avg} \leq k$, the generation is in the late period of evolution, in which the majority of population is in the vicinity of the global optimum. Thus, smaller rates of crossover and mutation are applied as follows,

$$\begin{cases} P_c = P_{c0} \times e^{\left(\frac{f_{\max} - f_{avg}}{f_{avg}} - k\right)/k} \\ P_m = P_{m0} \times e^{\left(\frac{f_{\max} - f_{avg}}{f_{avg}} - k\right)/k} \end{cases} \tag{4.2}$$

The adaptive rate is proposed based on the exponential form. The reasons can be summarized as follows. First, due to the variety of the generation and the stochastic nature of GA, the range of individuals’ fitness values is very large and it is also hard to be determined. Meanwhile, the values of crossover and mutation rates are very small. Thus, to express the crossover and mutation rates as functions of the fitness values, the exponential form is a good choice. Second, our aim of applying adaptive crossover and mutation rates is to apply smaller crossover and mutation rates during later stages of the GA run, and to use larger crossover and mutation rates during earlier stages of the GA run. Based on the characteristic curve of the exponential function e^x (where e is the base of the natural logarithm and it equals approximately 2.718281828), it can be obtained that when $(f_{\max} - f_{avg})/f_{avg} > k$, P_c belongs to $(P_{c0}, 2.718\,P_{c0})$ which is a larger rate that should be used during earlier stages of the GA run; when $(f_{\max} - f_{avg})/f_{avg} \le k$, P_c belongs to $(0.37\,P_{c0}, P_{c0})$ which is a smaller rate that should be used during later stages of the GA run.

4) Stopping Criterion: The GA stops after a given number of generations.

4.4 Local Search of Hybrid Learning Algorithm

Local search is performed on the set of parameters obtained by the global search. Generally, GA is inefficient in fine-tuning around the local optima. Local search helps a GA fine-tune and improves the convergence rate. Local search in the proposed algorithm uses Levenberg–Marquardt algorithm [36], an approximate second-order gradient descent method. It can avoid problems with singular or poorly-conditioned Jacobians.

In the local search, the optimal load parameter set θ^* will be obtained to minimize $\varepsilon(\theta)$ (the error between load model outputs and measurements). Local search takes a set of initial parameters as input, and outputs a locally optimized set of parameters. After the global search in the load parameter space, GA provides diverse sets of initial parameters for the nonlinear Levenberg-Marquardt algorithm. θ^* can be found by the local search as follows,

$$\theta^* = \arg\min_{\theta} \left\| \varepsilon(\theta) \right\| \tag{4.3}$$

Parameter updating method of the local search is explained in the following part. In the traditional gradient based approach, the parameter is updated as,

$$\theta_{i+1} = \theta_i + \alpha_i h_i \tag{4.4}$$

where α is the step size and h is the direction which makes that $\varepsilon(\theta_{i+1}) \leq \varepsilon(\theta_i)$. Usually, the Newton method is used to determine the update direction h as,

$$h_i = \frac{1}{N} H^{-1} J^T \varepsilon \tag{4.5}$$

where J is the Jacobian matrix obtained by taking the partial derivatives of the estimated outputs with respect to the parameters; H is the Hessian matrix which is obtained by taking the partial derivatives of the Jacobian matrix.

For Levenberg–Marquardt algorithm, an approximate Hessian is applied and defined as follows,

$$H = (J^T J + \alpha_i I) \tag{4.6}$$

where α_i is the adaptive step size, I is the identity matrix.

Levenberg–Marquardt algorithm updates parameters as,

$$\theta_{i+1} = \theta_i + (J^T J + \alpha_i I)^{-1} J^T \varepsilon \tag{4.7}$$

The approach in [36] was used to obtain α_i, which is chosen adaptively based on the distance to the optimal solution.

4.5 Hybrid Learning Algorithm

Step 0. *Initialization:* Randomly generate an initial population of N_{pop} solutions.

Step 1. *Evaluation:* Calculate the fitness value of each solution in the current population.

Step 2. *Selection:* Select $(N_{pop} - N_{elite})$ pairs of parents. The selection probability $P_S(\theta)$ of each solution θ in the population Ψ is specified by the roulette wheel selection scheme with the linear scaling:

$$P_S(\theta) = \frac{f_{\max}(\Psi) - f(\theta)}{\sum_{y \in \Psi} (f_{\max}(\Psi) - f(y))} \tag{4.8}$$

where $f_{\max}(\Psi)$ is the maximum (i.e., worst) fitness value among the current population Ψ .

Step 3. *Crossover and mutation:* Apply a crossover operation to each of the selected $(N_{pop} - N_{elite})$ pairs of parents with the crossover probability P_c . A new solution is generated from each pair. When the crossover operation is not applied, one parent is randomly chosen and handled as a new solution. Then apply a mutation operation to each new solution with the mutation probability P_m .

Step 4. *Elitist strategy:* Maintain elite members. Select the fittest N_{elite} solutions from the population. Then add their copies to the $(N_{pop} - N_{elite})$ solutions generated in Step 3 to construct a population of N_{pop} solutions.

Step 5. If the number of generations equals to the maximum generation number then go to Step 6, otherwise return to Step 1.

Step 6. *Local search:* After the global search by GA in the parameter space, the top n fittest solutions in the final generation are selected to be further optimized by the local search. The local search using Levenberg–Marquardt algorithm is applied to all the selected solutions. The fittest solution among the n selected solutions is the final optimal set of load parameters which will be obtained when the local search process is completed.

In the local search part (i.e., Step 6) of this algorithm, if n is set to be 1 the fittest solution from the global search will be used in the local search.

4.6 Numerical Test Results

To test the proposed method, the simulation data from a 23-bus system and the New England 39-bus system and the field measurement data from a utility are applied to construct the load models. For GA in the hybrid learning algorithm, the parameters are set as follows: Population size = 200; Initial crossover probability $P_{c0} = 0.8$; Initial mutation probability $P_{m0} = 0.05$; Elitists size $N_{elite} = 6$.

In section 4.6.1 and section 4.6.2, two test systems are applied to test the accuracy performance of the proposed algorithm for load modeling. In section 4.6.3, field measurement data is used to derive load models for testing both the accuracy and computation time performances of the proposed algorithm.

Both the Levenberg–Marquardt algorithm and genetic algorithm are applied to compare with the proposed hybrid learning algorithm. Load modeling process is commonly completed off-line to derive the accurate measurement-based load models for the power system planning and operation. Accurate load models are very important for both transient stability analysis and long-term stability analysis. Since the load modeling research in this dissertation does not consider the implementation for on-line load parameter identification, the speed feature of parameter identification technique is not the main concern. As the load model accuracy is the key factor to affect the system planning and operation and it still needs improvements [14], we mainly focus on the accuracy performance of the proposed algorithm. Levenberg–Marquardt algorithm, which is a nonlinear least-square based optimization algorithm, has been widely accepted and used by existing software tools exploited in the industry [11]. Our overall objective is to develop a systematic load modeling methodology such that it could be directly and fully useable by industry. Therefore, the proposed hybrid learning algorithm is mainly compared to the industry applied Levenberg–Marquardt algorithm to show the accuracy improvement for measurement-based load modeling.

4.6.1 *Test with Simulation Data of 23-bus Test System*

The 23-bus test system consists of 6 generators, 8 loads and 23 branches (see Fig. 6-2 for the system one-line diagram). The aggregate load at bus 153 consists of 50% static load (ZIP) and 50% dynamic load (Induction Motor). The static load consists of 40% constant power, 30% constant current, and 30% consistent impedance. The total active and reactive power of load 153 is 200MW and 100 MVar. Two different system disturbances were applied for the purposes of load parameter identification and load model validation.

4.6.1.1 Load Parameter Identification

A three phase fault at bus 152, initialed at 1s and cleared after 5 cycles, was applied to record the system disturbance data for load parameter identification. Load parameters to be identified include: 1) percentages of static and dynamic loads, 2) coefficients of static load and 3) individual parameters of dynamic load. Hybrid learning algorithm is applied to search for the optimal parameter set. Levenberg–Marquardt (L-M) algorithm is also applied for parameter identification as a comparison, in which an arbitrary initial point (within the permissible range) was used.

System disturbance data consists of bus voltage, real power, and reactive power of aggregate load 153. Table 4-1 provides the identified load parameters of the aggregate load model. Fig. 4-1 presents the power outputs of derived load models compared with the measurements. Root mean square (RMS) errors are calculated as Equation (4.9) to evaluate the accuracy of derived load models. Table 4-2 shows simulated model output errors in term of percentages with respect to the total load. Fig. 4-1 and Table 4-2 illustrate that the derived load model by hybrid learning presents smaller errors than the results obtained by L-M algorithm. Table 4-1 also indicates that hybrid learning based load parameters are closer to the values of actual load than L-M based results.

$$\begin{cases} \varepsilon_p(\theta) = \dfrac{1}{n}\sqrt{\sum_{k=1}^{n}[P_{km}(\theta) - P_{ks}(\theta)]^2} \\ \varepsilon_q(\theta) = \dfrac{1}{n}\sqrt{\sum_{k=1}^{n}[Q_{km}(\theta) - Q_{ks}(\theta)]^2} \end{cases} \tag{4.9}$$

Table 4-1. Load parameters by hybrid learning and L-M algorithm

	Hybrid learning	L-M algorithm	Actual Load
Dynamic Load	Per Unit	Per Unit	Per Unit
R_s	0.0488	0.0483	0.031
R_r	0.0679	0.0532	0.036
X_s	0.1037	0.2460	0.120
X_r	0.5671	0.3904	0.320
H	0.7195	0.7320	0.700
X_m	3.3231	3.9790	3.200
A	0.9895	0.9244	1.000
B	-0.0104	0.0057	0.000
D	-0.0104	0.0449	0.000
E	1.8630	1.9126	2.000
Static Load	Per Unit	Per Unit	Per Unit
"a_p" (P)	0.4281	0.3854	0.300
"b_p" (P)	0.2467	0.3927	0.300
"c_p" (P)	0.3252	0.3296	0.400
"a_q" (Q)	0.1562	0.4217	0.300
"b_q" (Q)	0.1433	0.0753	0.300
"c_q" (Q)	0.7005	0.0641	0.400
% Dyn. (P)	0.5820	0.4256	0.500
% Dyn. (Q)	0.4175	0.6640	0.500

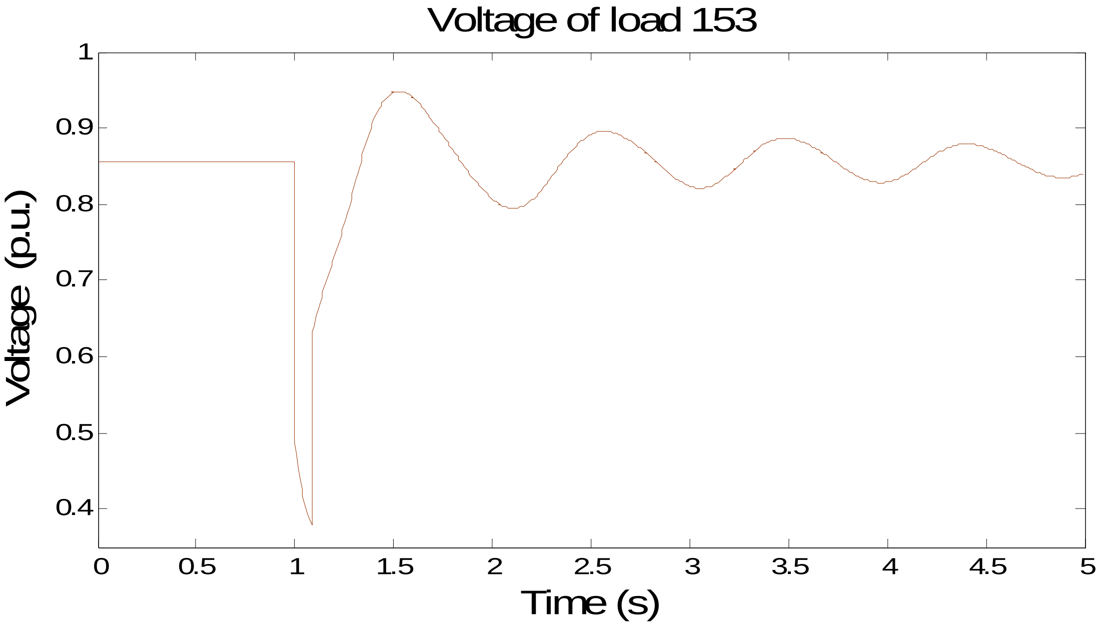
Voltage of load 153
Voltage (p.u.)
1
0.9
0.8
0.7
0.6
0.5
0.4
0
0.5
1
1.5
2
2.5
3
3.5
4
4.5
5
Time (s)

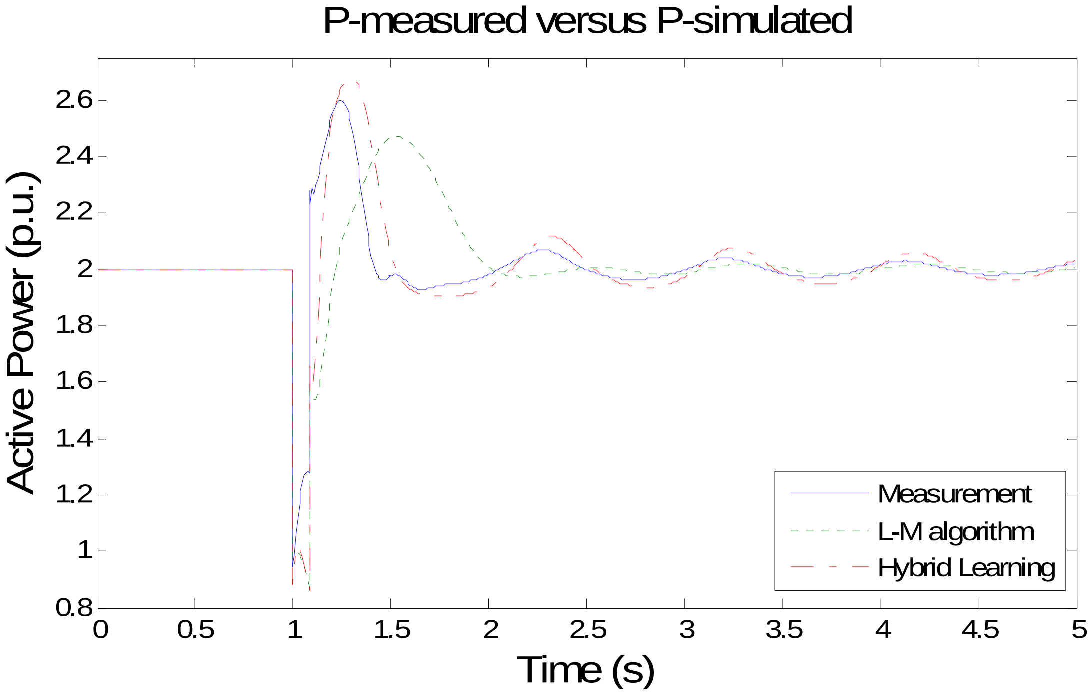
P-measured versus P-simulated
Active Power (p.u.)
2.6
2.4
2.2
2
1.8
1.6
1.4
1.2
1
0.8
0
0.5
1
1.5
2
2.5
3
3.5
4
4.5
5
Time (s)
Measurement
L-M algorithm
Hybrid Learning

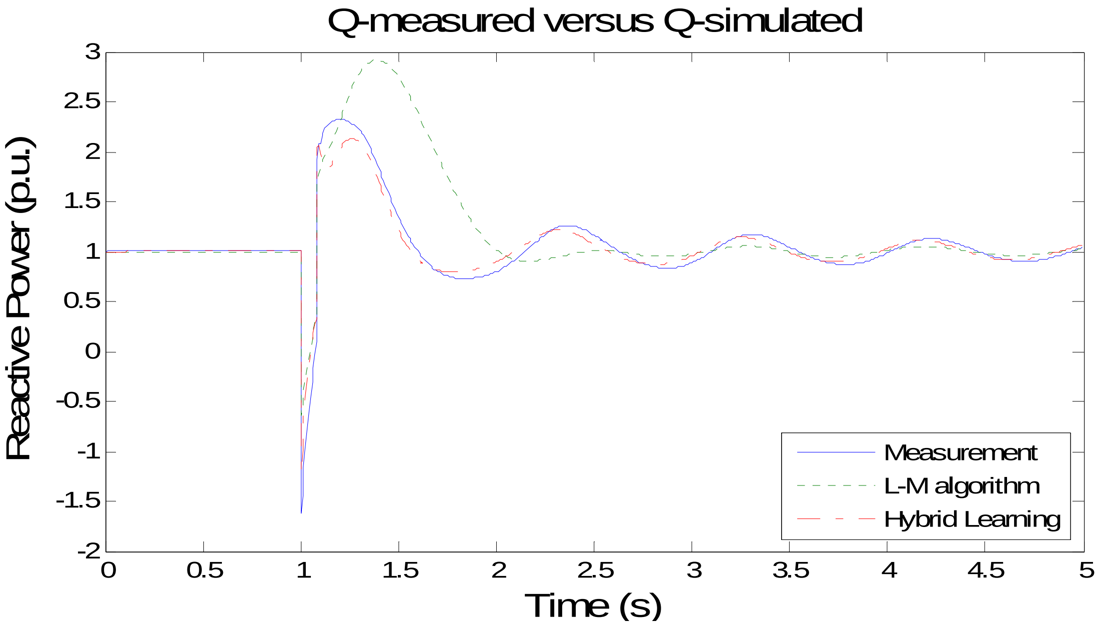

Fig. 4-1. Voltage and power of load 153 based on the disturbance at bus 152

Table 4-2. Errors between the simulated outputs and measurement

Error / Algorithm	RMS Error	
	P	Q
Hybrid learning algorithm	0.26%	0.49%
Levenberg–Marquardt algorithm	0.49%	2.08%

4.6.1.2 Validation of Derived Load Model

To validate the derived load model, a disturbance at bus 3005 was applied which is different from the one used for parameter identification. Fig. 4-2 shows the voltage and simulated powers of the derived load model at bus 153. Table 4-3 provides simulated output errors of the derived load model.

Voltage of bus 153 shows three large variations happened at 1s, 2s and 3s respectively. Plots of the power outputs show that the derived load model by hybrid learning satisfactorily provided the load responses with the variations of bus voltage. Due to the random and complex nature of power system loads and the nonlinear and non-convex search space of load parameters, the simulated load model can only be a close approximation to the real load and it cannot fit every measurement of the real load exactly. Actually, the simulated load model should present general characteristics of loads instead of fitting one or two sets of measurements very well, otherwise the model may lose the capability to capture other measurements. Since the disturbance used for the validation was not applied to derive the model, it is called an unseen system disturbance for the load model [27]. Validation results illustrate that the hybrid learning based load model is able to capture the unseen system disturbance, which indicates that the derived load model has a good generalization capability.

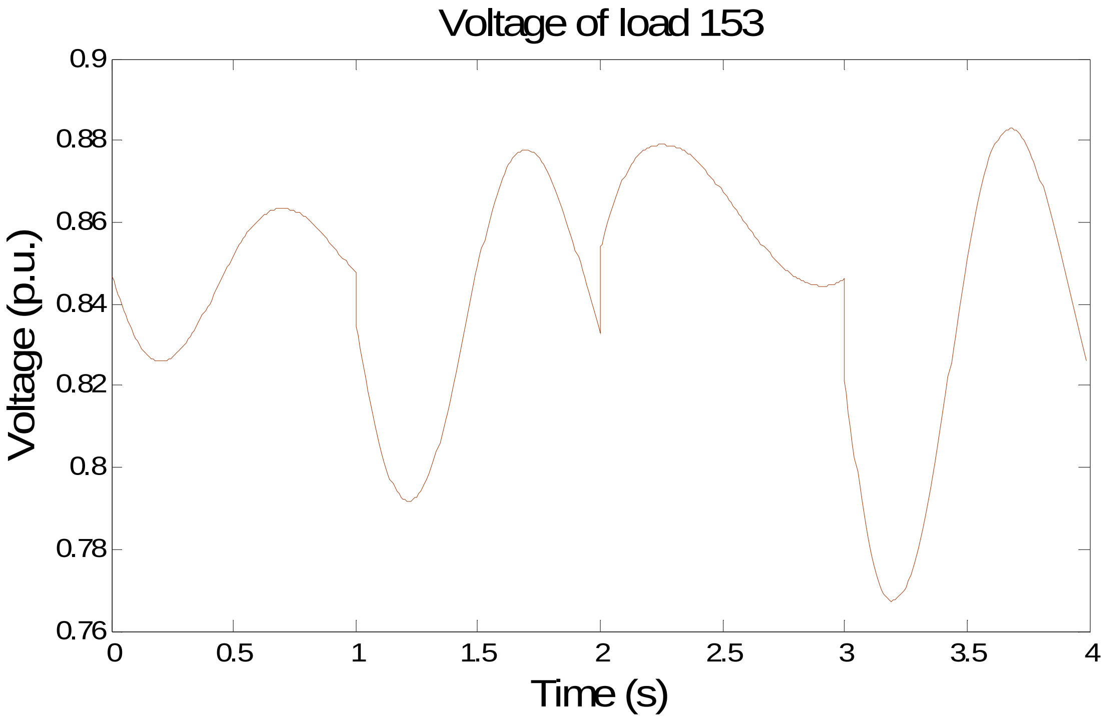
Voltage of load 153
Voltage (p.u.)
0.9
0.88
0.86
0.84
0.82
0.8
0.78
0.76
0
0.5
1
1.5
2
2.5
3
3.5
4
Time (s)

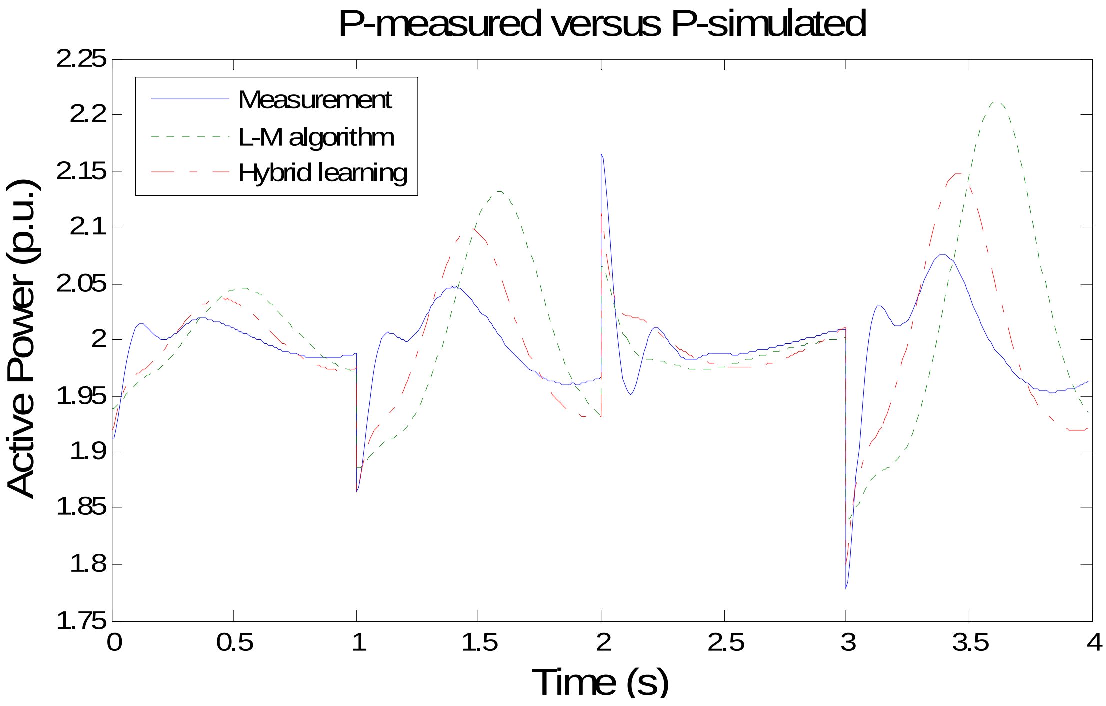
P-measured versus P-simulated
Active Power (p.u.)
Measurement
L-M algorithm
Hybrid learning
2.25
2.2
2.15
2.1
2.05
2
1.95
1.9
1.85
1.8
1.75
0
0.5
1
1.5
2
2.5
3
3.5
4
Time (s)

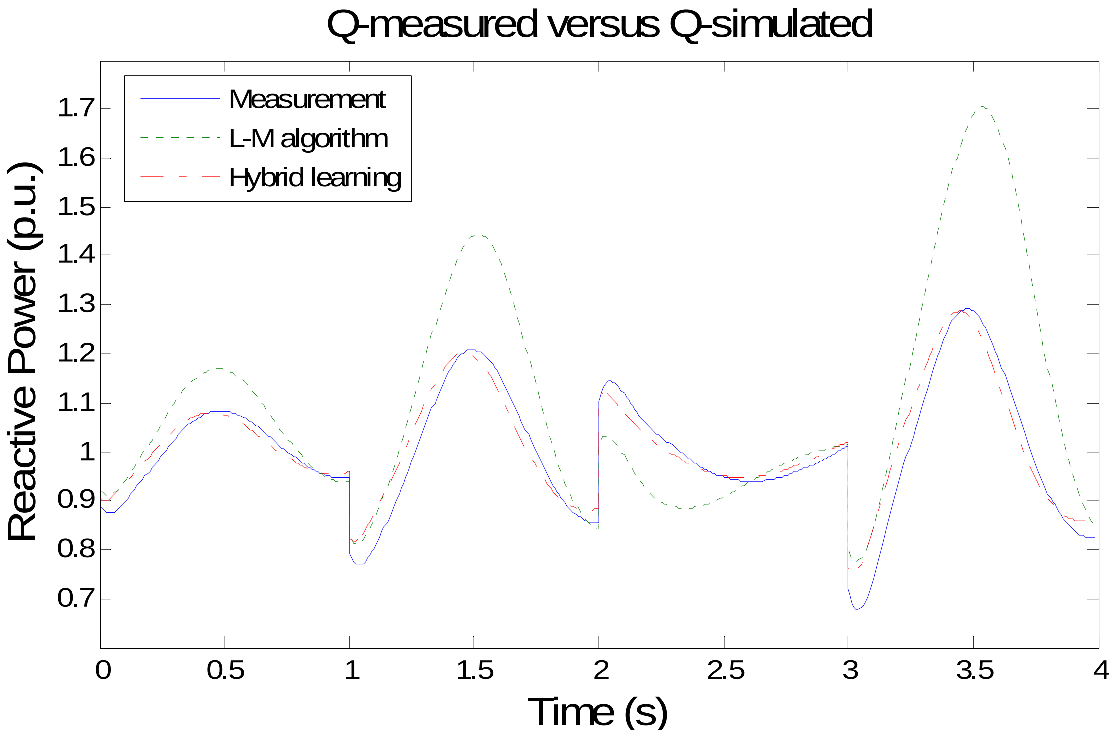

Fig. 4-2. Voltage and power of load 153 based on the disturbance at bus 3005

Table 4-3. Errors between the simulated outputs and measurement

Error Algorithm	RMS Error	
	P	Q
Hybrid learning algorithm	0.069%	0.13%
Levenberg–Marquardt algorithm	0.14%	0.60%

4.6.2 *Test with Simulation Data of New England 39-bus System*

New England 39-bus system consists of 46 branches, 10 generators, and 31 loads. Load modeling was performed for the load including induction motors at bus 16. A three phase fault was applied at bus 15 to record the measurement data, which was used to identify the load parameters.

To validate the derived load models, we applied a contingency in which the short term voltage instability and the induction motor stalling were created for testing purposes. The contingency is as follows: a three phase fault occurred on the line between buses 17 and 16, close to bus 17; fault was cleared after 7 cycles by opening the two circuit breakers and removing the faulted line; there was no reclosure. Voltage and power of the load during the pre-fault, fault and post-fault periods are shown in Fig. 4-3. It illustrates that the voltage of load 16 never recovered to an acceptable value after the fault and this led to the induction motor slowdown and eventually stalling as shown in the power and motor speed plots. The load model derived by hybrid learning accurately captured the induction motor stalling phenomenon and presented smaller output errors than those by L-M algorithm. Table 4-4 gives the simulated output errors of the two algorithms in terms of P, Q and motor speed.

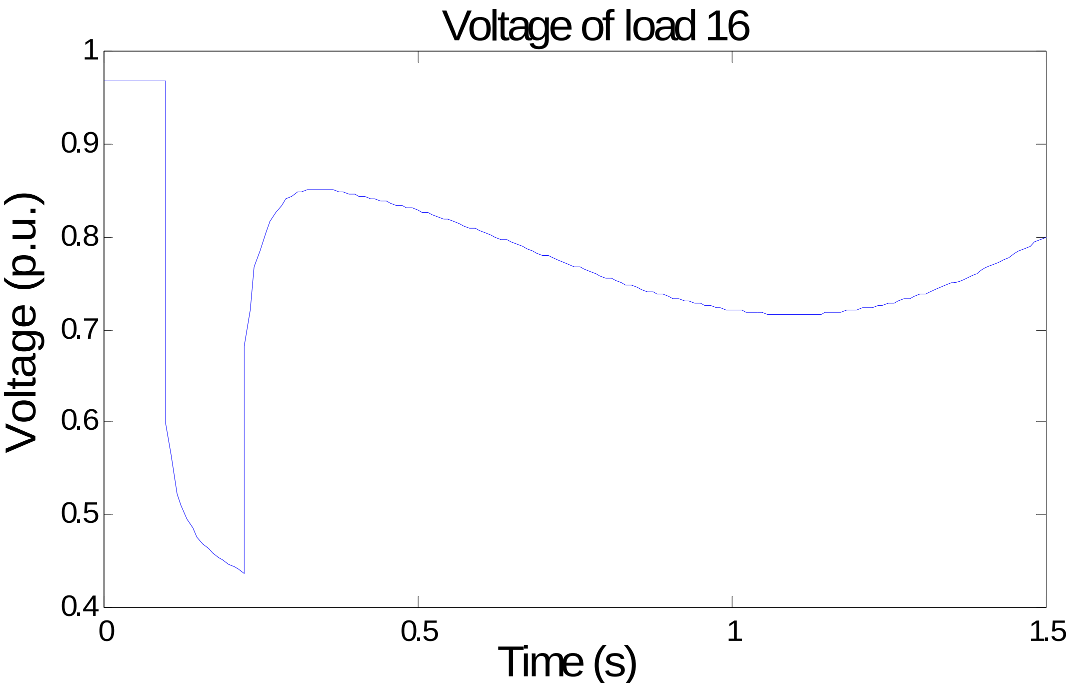
Voltage of load 16
Voltage (p.u.)
1
0.9
0.8
0.7
0.6
0.5
0.4
0
0.5
1
1.5
Time (s)

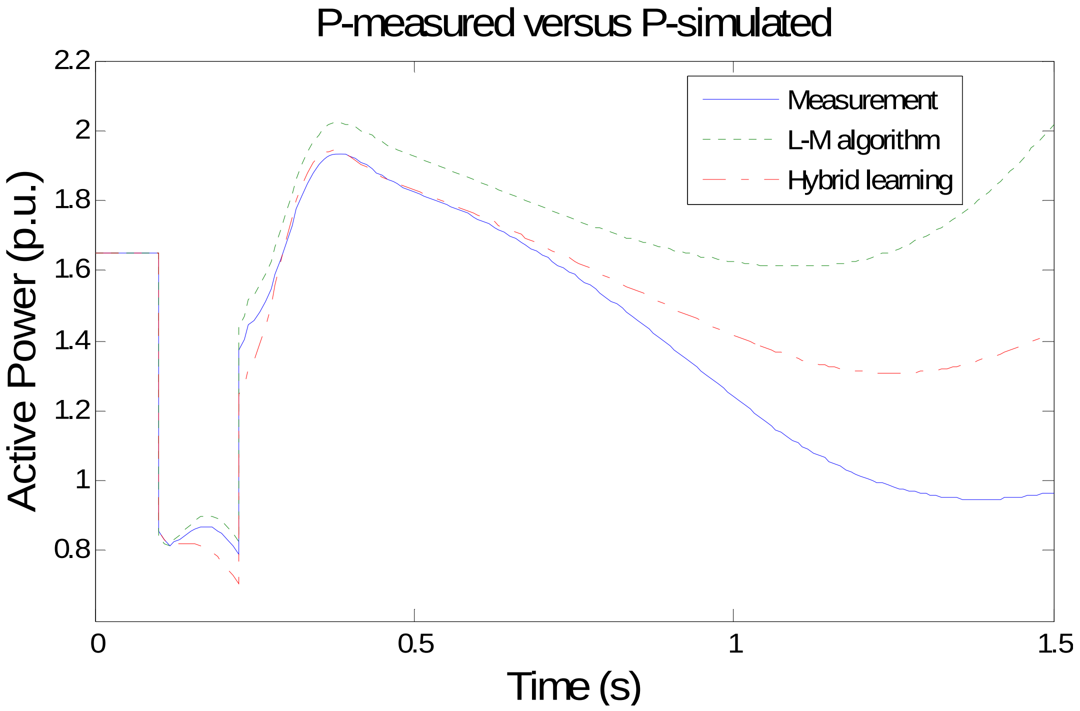
P-measured versus P-simulated
Active Power (p.u.)
2.2
2
1.8
1.6
1.4
1.2
1
0.8
0
0.5
1
1.5
Time (s)
Measurement
L-M algorithm
Hybrid learning

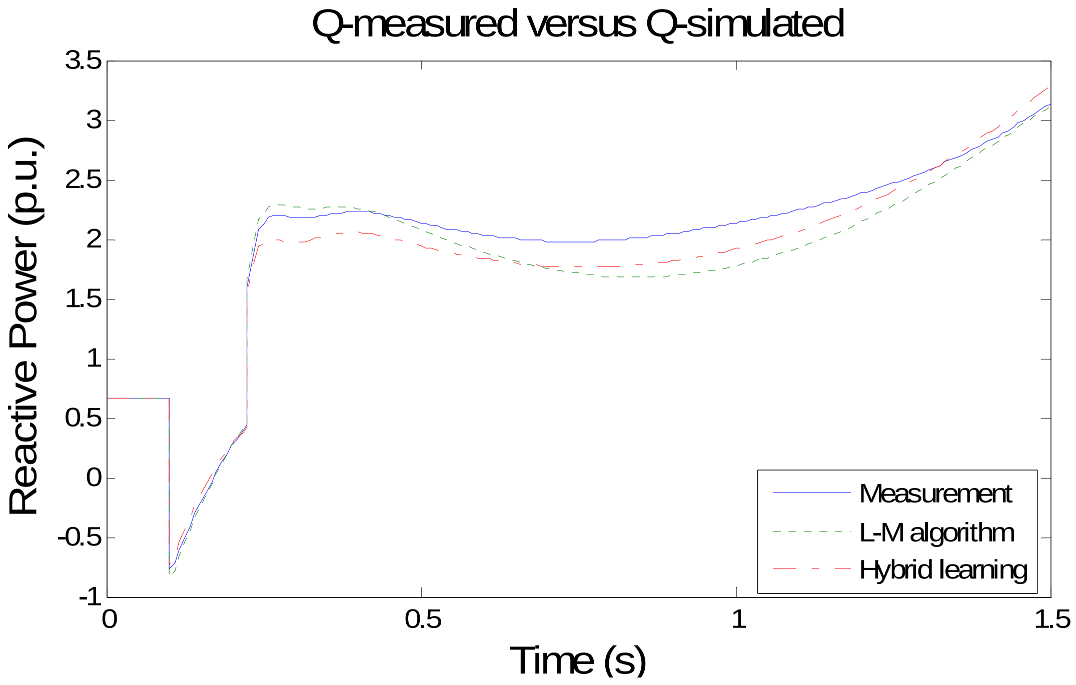

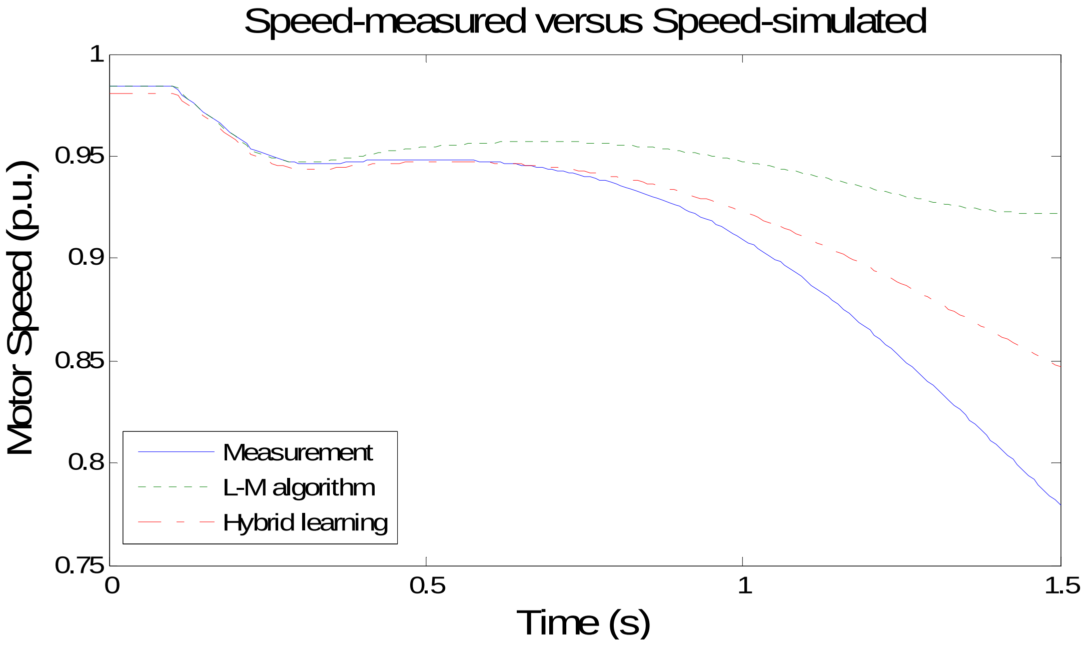

Fig. 4-3. Voltage, power and motor speed of load 16 after a three phase fault

Table 4-4. Errors between the simulated outputs and measurement

Error Algorithm	RMS Error		
	P	Q	Speed
Hybrid learning algorithm	0.89%	1.83%	0.18%
Levenberg–Marquardt algorithm	1.94%	2.26%	0.39%

4.6.3 *Test with Field Measurement Data of a Utility*

To further test the accuracy and computation time performances of the proposed algorithm, field measurement data from an international utility were used to derive the load models. The data were taken from field test results carried out at one of the 69kV substations. In this substation, feeders supply industrial loads. Load voltage and current data were recorded by an IED (Intelligent Electronic Devices). Sequentially, real power and reactive power were calculated using the recorded voltage and current. Fig. 4-4 shows load characteristics in one disturbance on 12/21/2006. From Fig. 4-4 and Table 4-5, we see that outputs of the derived load model by hybrid learning closely match the field measurements and present smaller output errors than results obtained by L-M algorithm. Also, it clearly shows that with noise in the field measurements, the hybrid learning algorithm can still accurately model the system load and capture the real time load characteristics properly.

For illustrating the computation time performance, the proposed algorithm is compared with GA, which has the same parameter settings as shown at the beginning of section 4.6 and its stop criteria is that GA stops when a chromosome reaches a specified fitness level. Two sets of measurement data from the substation mentioned above were applied to model loads using the two techniques. Table 4-6 demonstrates the load parameter identification results. The computation time and RMS error from both techniques (GA and hybrid learning algorithm) are provided in the table. It shows that both techniques can accurately derive the load model parameters. Load parameters derived by GA have the smallest RMS error percentage as 0.26% and the value by the proposed algorithm is 0.21%. Computation time is the main factor to distinguish the two techniques. Time performance testing was carried out using an Intel Pentium processor based PC (2.0GHz, 1.0 GB RAM). To identify one set of load parameters, GA needs the shortest time as 1728s while the time for the hybrid learning algorithm is 86.3s. As expected, GA requires a very long computation time to obtain the load parameters since it does not use much local information to determine the most promising search direction. Therefore, the hybrid learning algorithm provides a major advantage over GA in term of computational cost.

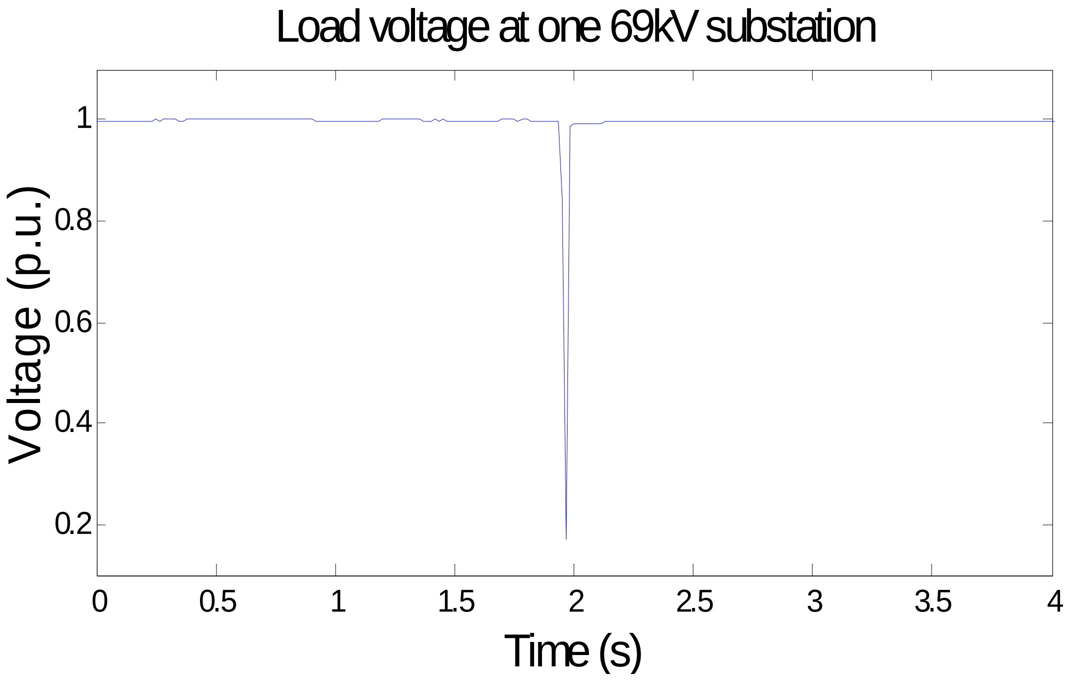
Load voltage at one 69kV substation
Voltage (p.u.)
1
0.8
0.6
0.4
0.2
0
0.5
1
1.5
2
2.5
3
3.5
4
Time (s)

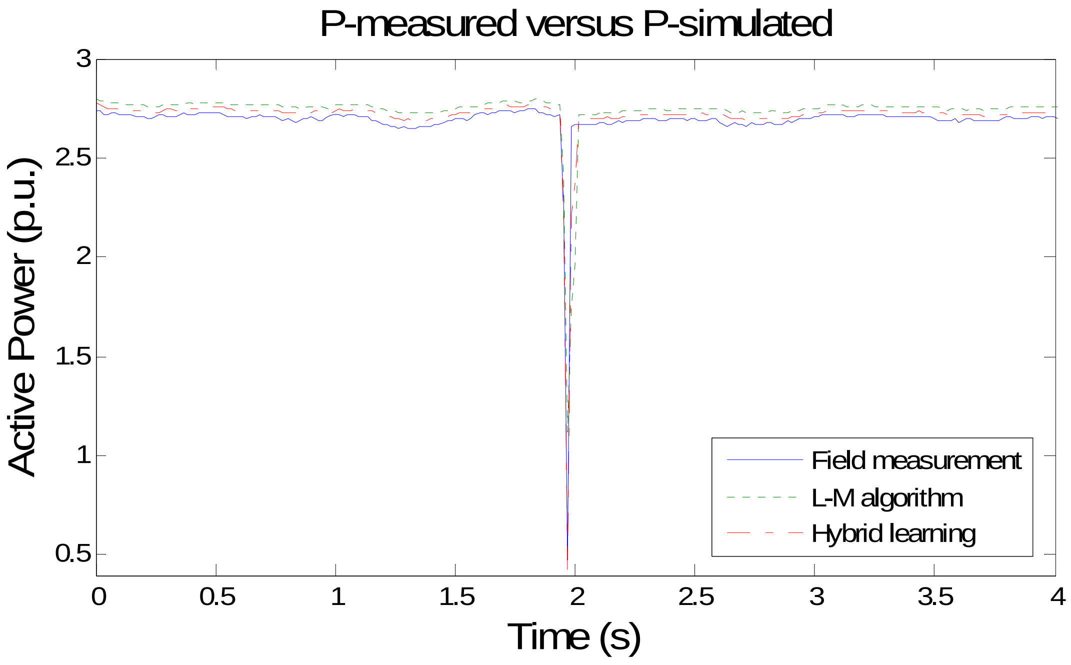
P-measured versus P-simulated
Active Power (p.u.)
3
2.5
2
1.5
1
0.5
0
0.5
1
1.5
2
2.5
3
3.5
4
Time (s)
Field measurement
L-M algorithm
Hybrid learning

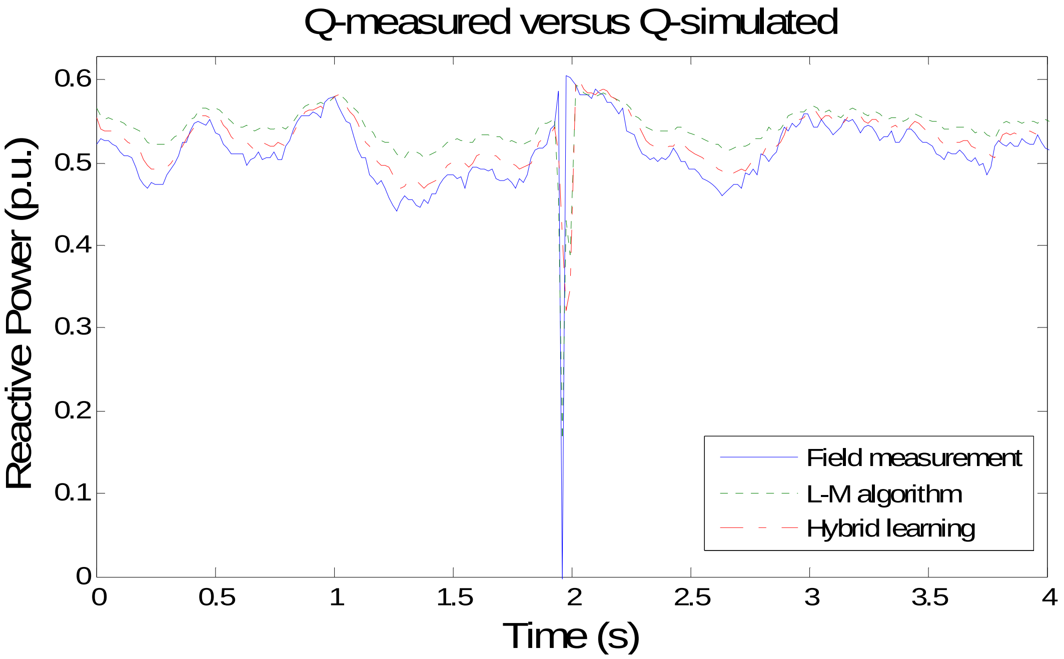

Fig. 4-4. Voltage and power of load at one 69kV substation on 12/21/2006

Table 4-5. Errors between the simulated outputs and measurement

Error / Algorithm	RMS Error	
	P	Q
Hybrid learning algorithm	0.11%	0.26%
Levenberg–Marquardt algorithm	0.24%	0.51%

Table 4-6. Parameter identification results for hybrid learning and GA

Field Data	Computation Time		Accuracy (RMS Error)			
	GA	Hybrid learning	GA		Hybrid-learning	
			P	Q	P	Q
Data 1	2435s	125.2s	0.26%	0.58%	0.21%	0.62%
Data 2	1728s	86.3s	0.63%	1.67%	0.49%	1.14%

4.6.4 *System Stability Analysis based on Derived Load Models*

Most Power system failures are not initiated by instability, but rather by unanticipated protection operation. The ability to predict operation of protection devices, and hence potential protection-induced cascading failures, can be greatly affected by load model fidelity [8].

System stability analysis is performed using the 23-bus system incorporated with the derived load model at bus 153. The test fault is a three-phase fault at bus 152, on line 152-153, which is subsequently cleared by opening circuit breaker at bus 152 end in five cycles and opening the remote end in 7.5 cycles. The whole simulation time is five seconds. Fig. 4-5 and Fig. 4-6 present the apparent impedance locus seen by relay 152-153 versus protection zones in the R-X plain. Seen from the two figures, the measurements based apparent impedance locus entered the zone-1 area during the fault which caused the relay to trip that line simultaneously. Fig. 4-5 shows that the hybrid learning based load model properly captured the fault event and the simulated apparent impedance locus entered the zone-1 area.

However, Fig. 4-6 shows that only the zone-2 area was entered based on the L-M algorithm derived load model which means the relay did not trip that line simultaneously. Thus, the L-M algorithm based load model did not response accurately to the fault. This proves that the reliability of system stability study results can be improved by having more accurate aggregate load models.

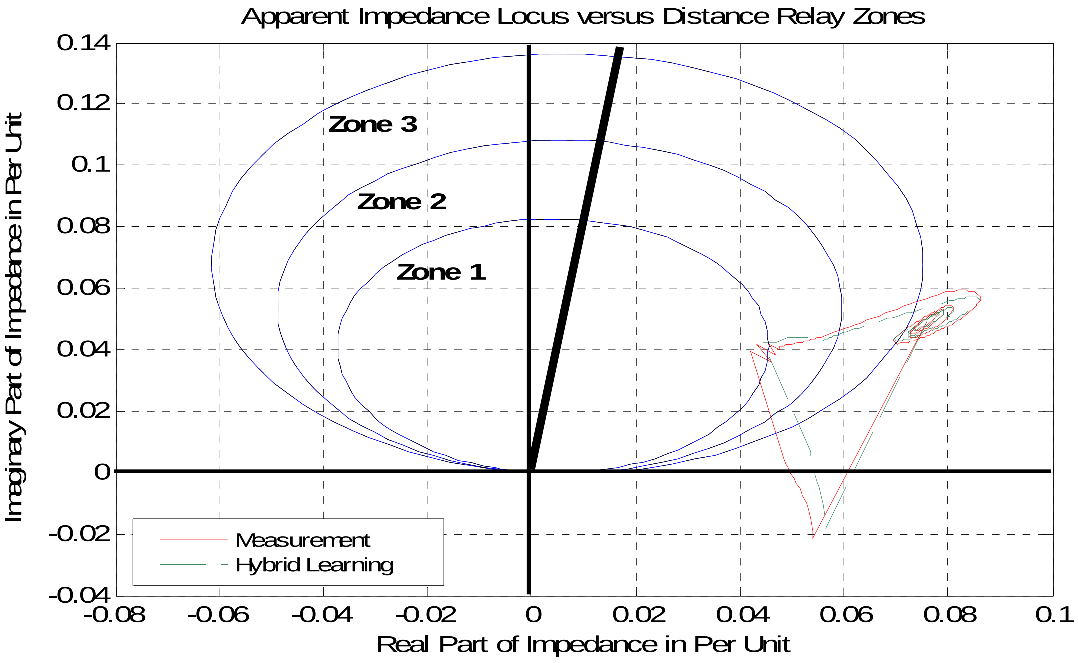

Fig. 4-5. 3-Zone protection on line 152-153 based on the measurements and the derived load model by hybrid learning algorithm

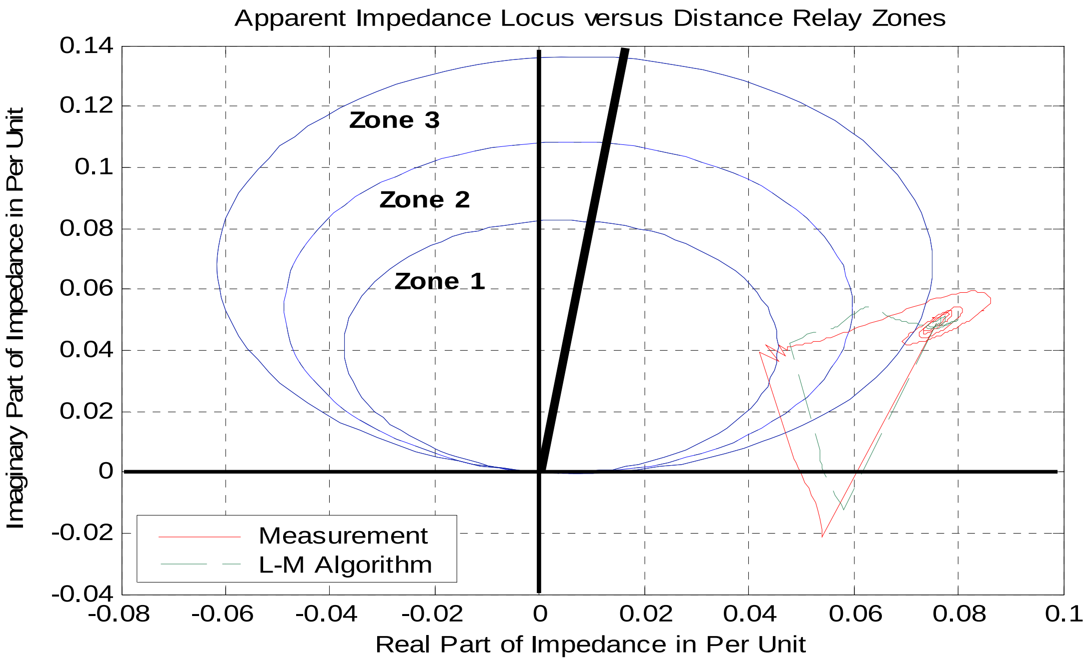

Fig. 4-6. 3-Zone protection on line 152-153 based on the measurements and derived load model by L-M algorithm

4.7 Summary

It is difficult and complex to set up an aggregate load model for a large scale of power system. In the absence of precise information about a power system load, one of the most reliable ways to obtain an accurate load model is to apply the measurement-based approach. If field measurement data are available which adequately describe the load behavior, a dynamic and/or static equivalent of the load can be obtained by analyzing functional relationships between these quantities using parameter identification techniques. There are also some shortcomings of this approach. When recording field measurement data, it is often necessary to monitor the system for a long time to consider different variations in system configurations and load patterns. To obtain a better load model, we need measurement data recorded during large disturbance that can lead to significant changes of voltage and frequency. However the large disturbances are rare events in practical power systems. Hence, it could be difficult to identify and develop "generic" parameters that must be used for dynamic and transient studies with a small set of measurements from these rare events. However, this approach is still preferred over the approach that uses pre-defined parameters for load models, since it can yield more accurate load parameters. Regarding choosing the load model structure, the physical based dynamic load model (induction motor model) describes load compositions in terms of physical devices. Such models can potentially provide better representations of loads over a wide range of system conditions. However, the parameters of the input-output based dynamic load model do not have any physical meanings and can vary dramatically during different fault conditions and system configurations. Although the model structure and objective function formulation are relatively straightforward, and can be particularly useful when the load composition is complex, it is very difficult to constrain the parameters. Developing generic models with this model structure is next to impossible.

Our research is aimed at developing generic load models, if possible, that can be applied over wide variety of disturbances and system configurations. Measurement-based approach has certain advantages over component-based approach in that it reflects actual load behaviors during disturbances. Tests using simulation data and field measurement data clearly enumerate the ability of the hybrid learning algorithm to identify load model parameters accurately and efficiently under various system operating conditions. Especially, the load dynamic responses during large voltage variations and induction motor stalling were captured appropriately. Hybrid learning algorithm can be further improved for load parameter identifications in several ways, such as the way to combine global search and local search, the strategy to set parameters, the balance between global search and local search.

CHAPTER 5 FAULT-INDUCED DELAYED VOLTAGE RECOVERY

5.1 Introduction

In this chapter, the static modeling and *P*-*S* and *Q*-*V* characteristics of induction motor are provided to investigate the FIDVR mechanism. Induction motor kinetic energy deviation has been shown to be identical to the integral of power imbalance. Based on the analysis, the motor kinetic energy is proposed to be used for FIDVR mitigation. In order to derive kinetic energy, the equivalent inertia and the speed of the induction motor are needed. A methodology is proposed to obtain these variables through online measurements.

5.2 Static Modeling of Induction Motor

Appropriate machine modeling is necessary to understand induction motor characteristics. Induction motor is represented using traditional steady state model as Fig. 5-1 (a) [56].

R_s and X_s are stator resistance and reactance; R_r and X_r are rotor resistance and reactance; X_m is magnetizing reactance; ω is rotor speed; $s=(\omega_s-\omega)/\omega_s$ is slip. Since R_s is small and $X_m >> X_s$, model is simplified as Fig. 5-1 (b), where $X_{eq}=X_s+X_r$ and $R_{eq}=R_r$ are equivalent reactance and resistance.

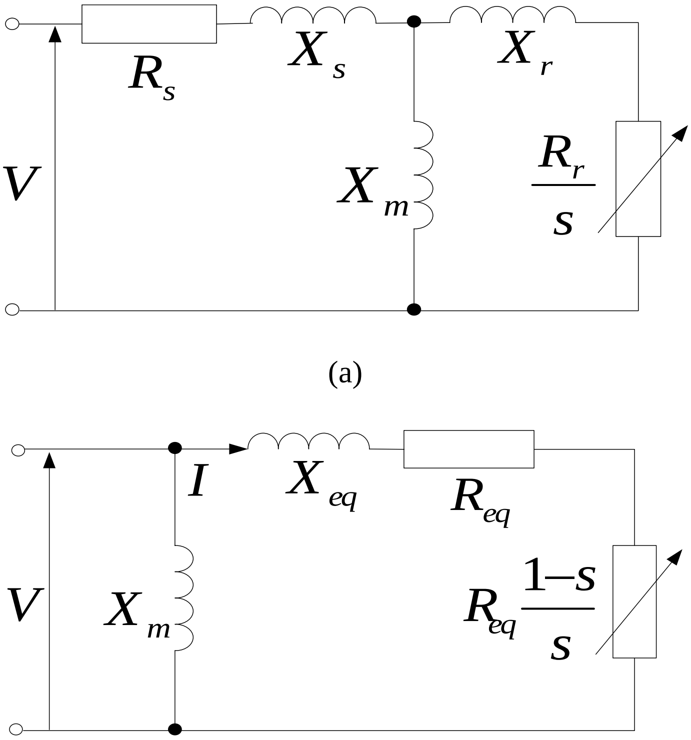

(a)

(b)

Fig. 5-1. Traditional and simplified steady state induction motor models

5.3 P-S and Q-V Characteristics of Induction Motor

Using simplified model as Fig.5-1 (b), motor current I and power are obtained by equations 5.1-5.3. P_l and Q_l are real and reactive powers by mechanical load, Q_m and Q_{TL} represent reactive power by magnetizing reactance and total load. Critical slip s_c is obtained by differentiating P_l with respect to s in (5.2). It should be noted that s_c does not depend on the voltage.

$$I^2 = \frac{V^2}{X_{eq}{}^2 + (R_{eq}/s)^2} \tag{5.1}$$

$$P_l = I^2 \frac{R_{eq}}{s} = V^2 \frac{R_{eq}s}{R_{eq}{}^2 + (X_{eq}s)^2}, \quad s_c = \frac{R_{eq}}{X_{eq}} \tag{5.2}$$

$$Q_l = I^2 X_{eq} = V^2 \frac{X_{eq}s^2}{R_{eq}{}^2 + (X_{eq}s)^2}, \quad Q_m = \frac{V^2}{X_m}, \quad Q_{TL} = Q_m + Q_l \tag{5.3}$$

Figure 5-2 (a) shows P_l - s curves under different voltages, where V_0 and V_{stall} are rated and motor stalling voltages. It can be proved that the motor stable operating region is to the left of the peak in Fig. 5-2 (a), where $s < s_c$. Figure 5-2 (b) shows Q_{TL}, Q_m and Q_l as functions of voltage. Q_l gradually increases as voltage decreases until $V = V_{stall}$, where Q_l is increased greatly.

Observing $Q_{TL} - V$ curve, it is found: (1) when voltage is close to the rated value, slope of the curve is positive (voltage decrease causes reduced reactive power demand); (2) curve between rated voltage and stalling voltage is relatively flat (low voltage sensitivity); (3) when voltage is reduced beyond the stalling value, reactive power demand is increased tremendously to a very large value

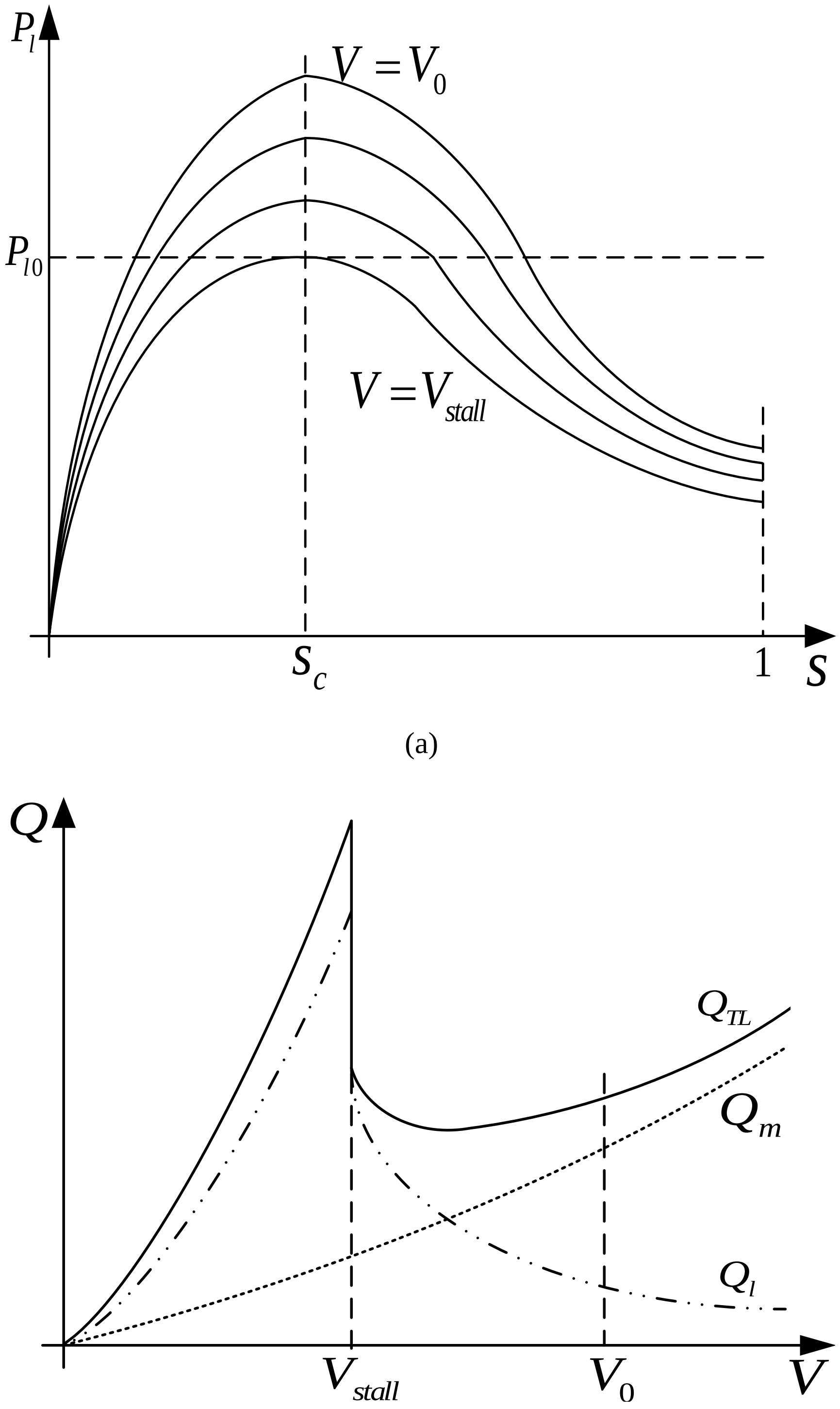

(a)

(b)

Fig. 5-2. *P*-*S* and *Q*-*V* characteristics of induction motor

5.4 Mechanism of FIDVR

After clearing faults in induction motor dominated areas, low voltages could be sustained beyond a certain time range (maybe a few cycles or several seconds). Then induction motors start stalling. When motor stalls, it is under the locked-rotor condition which consumes 5 to 6 times the steady state motor current and thus demands largely increased reactive power instantaneously (shown in above *Q*-*V* analysis). Even though stalled motors can be disconnected by thermal protections with an inverse time-overcurrent characteristic, it takes 3-20 seconds. If local reactive power resources are exhausted and remote reactive power cannot be delivered at that time, voltage cannot be recovered and it may be reduced further. Then, the delayed voltage recovery may spread to nearby regions and cause generators to be tripped or generator reactive power outputs to be reduced by over-excitation limiters. Eventually, system voltage collapse would occur.

5.5 Applied Transient Voltage Recovery Criterion

To evaluate system voltage recovery, a transient voltage recovery criterion (TVRC) is needed. TVRC for generators have been developed considering generator protection settings and susceptible auxiliary equipments [57] [48]. TVRC for transmissions have also been proposed based on generator TVRC [57] [48], however, they do not necessarily consider the particular issues (motor stalling) in transmission system. The transmission TVRC (see Fig. 5-3) developed by studying the transmission system of PJM [58] seems to be adequate for mitigating FIDVR and thus it is applied in this dissertation.

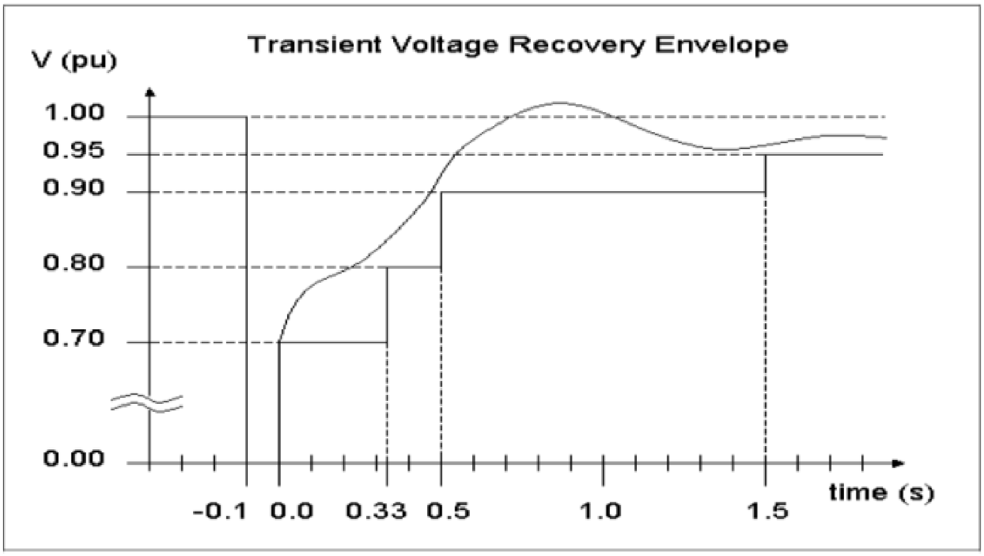

Fig. 5-3. Transient voltage recovery criterion for transmission system [58]

5.6 Motor Kinetic Energy Derivation

Derivation of equivalent motor kinetic energy consists of obtaining equivalent motor inertia and estimating equivalent motor speed using measurements. Since it is not feasible to separate dynamic and static loads under one transmission bus of practical power systems, the total load at one transmission bus is treated as an equivalent induction motor in order to evaluate each load bus's contribution in the FIDVR event. Therefore, measurements of the total bus load will be used to derive the equivalent motor inertia and motor speed.

5.6.1 *Inertia Derivation of Equivalent Induction Motor*

Inertia is a very critical motor parameter affecting induction motor performance. Motors with small inertias are considered as "prone to stall" motors, such as the compressor motors of A/C, which decelerate and stall at fault voltages below about 60% assuming five-cycle fault clearing time [39]. With slower fault clearing, they may stall at higher fault voltages.

In this dissertation, equivalent motor inertia is derived by measurement-based load modeling approach. Main procedure for load parameter derivation can be described as follows. Measured voltage is first input to actual load and load model to derive measured and simulated real/reactive power. The difference between load model outputs and measurements is then calculated to evaluate whether the accuracy criterion is satisfied. If not, optimization algorithm is applied to optimize the load parameters and update the load model. Detailed load parameter derivation is provided in [59]. Formulation of induction motor model is described as follows [7],

$$\begin{cases} \dfrac{dE_d^{'}}{dt} = -\dfrac{1}{T^{'}}\left[E_d^{'} + \left(X - X^{'}\right)I_q\right] - (\omega - 1)E_q^{'} \\ \dfrac{dE_q^{'}}{dt} = -\dfrac{1}{T^{'}}\left[E_q^{'} - \left(X - X^{'}\right)I_d\right] + (\omega - 1)E_d^{'} \\ \dfrac{d\omega}{dt} = -\dfrac{1}{2H}\left[T_0(A\omega^2 + B\omega + C + D\omega^E) - \left(E_d^{'}I_d + E_q^{'}I_q\right)\right] \end{cases} \tag{5.4}$$

$$\begin{cases} I_d = \dfrac{1}{R_s^2 + X^{'2}}\left[R_s\left(U_d - E_d^{'}\right) + X^{'}\left(U_q - E_q^{'}\right)\right] \\ I_q = \dfrac{1}{R_s^2 + X^{'2}}\left[R_s\left(U_q - E_q^{'}\right) - X^{'}\left(U_d - E_d^{'}\right)\right] \end{cases} \tag{5.5}$$

where $X^{'} = X_s + (X_m X_r)/(X_m + X_r)$ is the transient reactance and is equal to the blocked-rotor (short-circuit) reactance, $X = X_s + X_m$ is the motor no-load (open-circuit) reactance and

$T' = (X_r + X_m)/(\omega_s R_r)$ is the transient open-circuit time constant; H is rotor inertia constant; T_0 is steady state mechanical torque; E_d' and E_q' are d-axis and q-axis transient EMF of motor; U_d and U_q are d-axis and q-axis bus voltage, I_d and I_q are d-axis and q-axis stator currents; A, B, C, D, E are coefficients of load torque in terms of motor rotation speed, and satisfy $C = 1 - A\omega_0^2 - B\omega_0 - D\omega_0^E$.

For measurement-based load modeling, it is suggested that care must be taken to interpret the applicability of the derived model parameters for operating or disturbance conditions that are very different from what have been used to derive the load parameters [59]. For example, the parameters derived based on measurement data acquired during summer seasons may not be accurate or correct for use in winter seasons. Therefore, a thorough sensitivity study for derived load parameters (especially inertia *H*) is provided in this section. Trajectory sensitivity method is applied to determine the sensitivities associated with load parameters [60] - [62]. Load model equations can be generally formulated as follows:

$$\begin{cases} \dot{x}(\theta,t) = f(x(\theta,t), y(\theta), \theta) \\ 0 = g(x(\theta), y(\theta), \theta) \end{cases} \tag{5.6}$$

where x is the state variable and y is the algebraic variable; θ represents load parameters. To identify the trajectory sensitivity, a small disturbance λ is added to θ to obtain the perturbed load parameters $\theta' = \theta + \lambda$, and (5.6) is rewritten as,

$$\begin{cases} \dot{x}(\theta',t) = f(x(\theta',t), y(\theta'), \theta') \\ 0 = g(x(\theta'), y(\theta'), \theta') \end{cases} \tag{5.7}$$

Expand (5.7) into Taylor series (higher order terms neglected),

$$\begin{cases} \dot{x}(\theta,t) + \dfrac{\partial \dot{x}(\theta',t)}{\partial \theta'}\Big|_{\theta'=\theta} \cdot \lambda = f(x(\theta,t), y(\theta), \theta) + \dfrac{\partial f}{\partial \theta'}\Big|_{\theta'=\theta} \cdot \lambda \\ 0 = g(x(\theta,t), y(\theta), \theta) + \dfrac{\partial g}{\partial \theta'}\Big|_{\theta'=\theta} \cdot \lambda \end{cases} \tag{5.8}$$

Coefficients of λ with the same order should be equal,

$$\begin{cases} \dfrac{\partial \dot{x}(\theta',t)}{\partial \theta'} = \dfrac{\partial f}{\partial \theta'} = \dfrac{\partial f}{\partial x} \cdot \dfrac{\partial x}{\partial \theta'} + \dfrac{\partial f}{\partial y} \cdot \dfrac{\partial y}{\partial \theta'} + \dfrac{\partial f}{\partial \theta'} \\ 0 = \dfrac{\partial g}{\partial \theta'} = \dfrac{\partial g}{\partial x} \cdot \dfrac{\partial x}{\partial \theta'} + \dfrac{\partial g}{\partial y} \cdot \dfrac{\partial y}{\partial \theta'} + \dfrac{\partial g}{\partial \theta'} \end{cases} \tag{5.9}$$

Therefore, the parameter trajectory sensitivities will be obtained by solving the time-variant linear equations (5.9).

Figure 5-4 presents the trajectory sensitivities of six critical motor parameters using the IEEE Type 6 Model (Appendix A) subjected to a typical fault-induced 35% voltage drop at the motor bus. It is known that parameter trajectory sensitivities are affected by the initial values and trajectories. However, studies with various initial values and different trajectories indicate that parameter sensitivity rankings in most cases are the same as the one based on IEEE Type 6 Model, which has also been proved in [60]. Studies (see Fig. 5-4) have also shown that motor inertia (*H*) has a very small sensitivity value which means obtained inertia is not sensitive to measurement variations. Thus, the equivalent inertia derived by measurement-based load modeling approach can be applied over a relatively wide variety of disturbances.

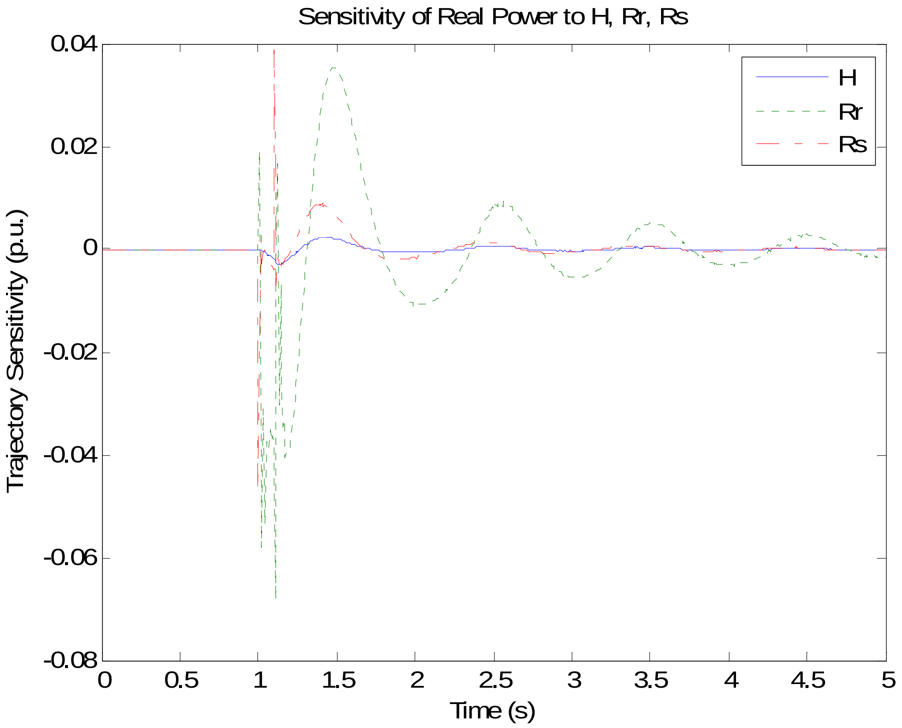

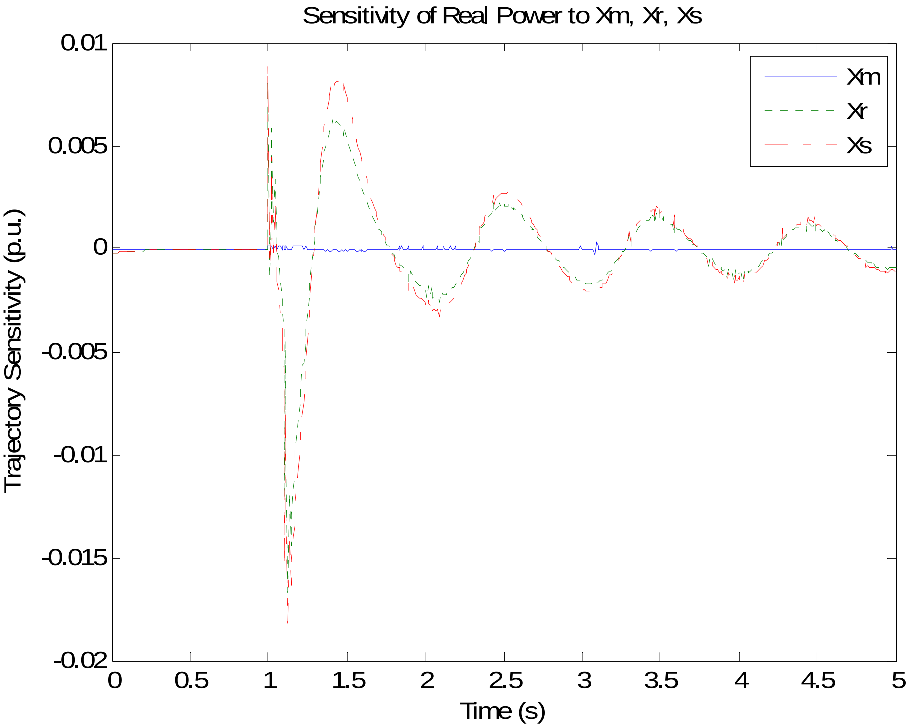
Sensitivity of Real Power to Xm, Xr, Xs
Trajectory Sensitivity (p.u.)
Time (s)
0.01
0.005
0
-0.005
-0.01
-0.015
-0.02
0
0.5
1
1.5
2
2.5
3
3.5
4
4.5
5
Xm
Xr
Xs

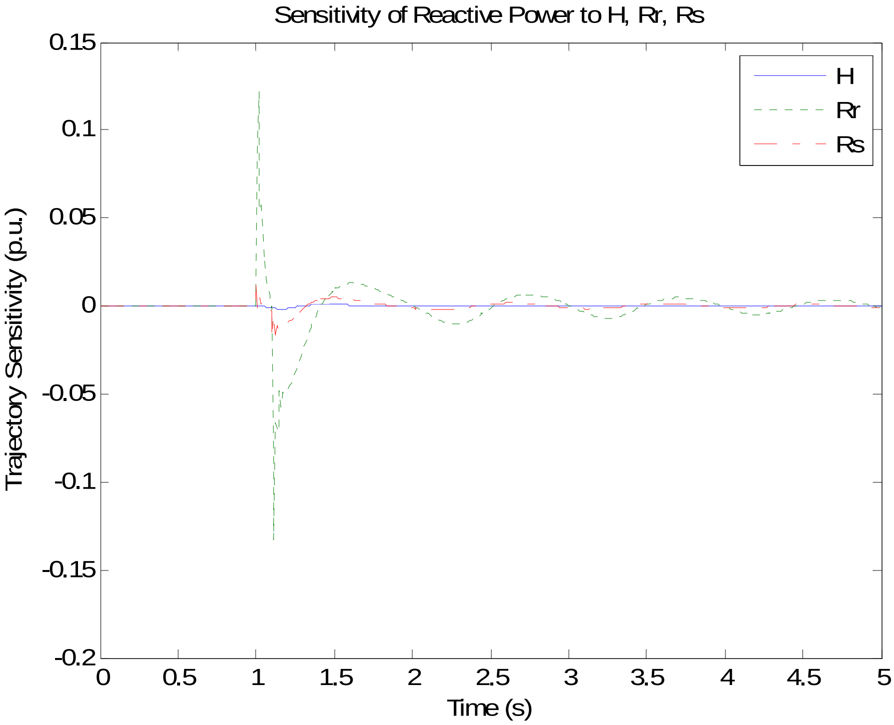
Sensitivity of Reactive Power to H, Rr, Rs
Trajectory Sensitivity (p.u.)
Time (s)
0.15
0.1
0.05
0
-0.05
-0.1
-0.15
-0.2
0
0.5
1
1.5
2
2.5
3
3.5
4
4.5
5
H
Rr
Rs

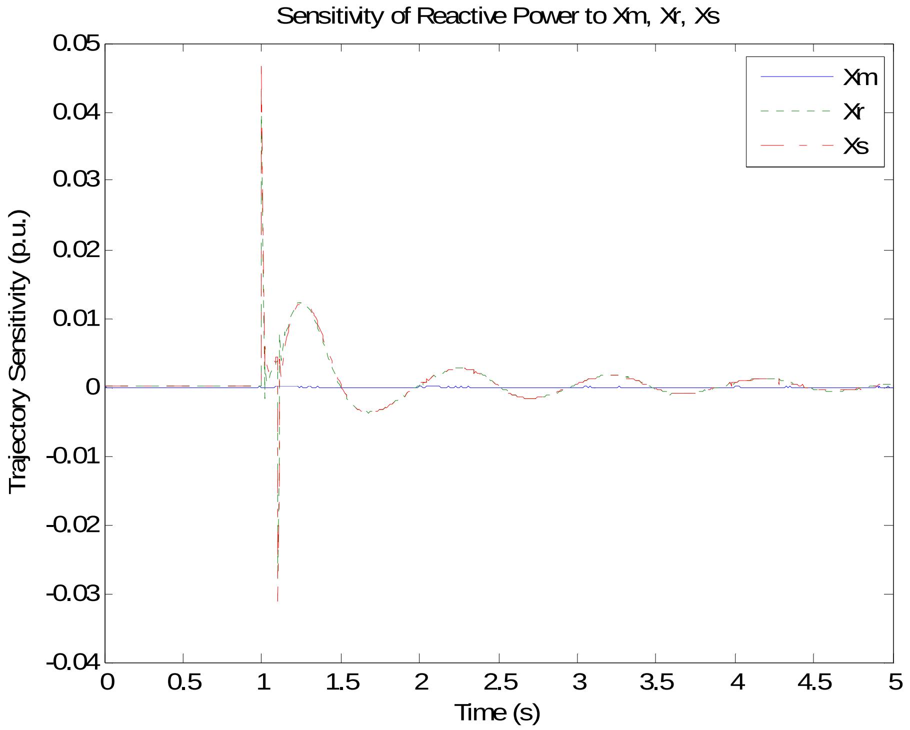

Fig. 5-4. Trajectory sensitivities of parameters *H, Rr, Rs* and *Xm, Xr, Xs*

5.6.2 *Speed Derivation of Equivalent Induction Motor*

5.6.2.1 Speed Derivation using Online Measurements

Equivalent motor speed is derived using voltage and current measurements of the total bus load which is treated as an equivalent induction motor. Based on simplified steady state model (Fig. 5-1 (b)), equivalent impedance $\tilde{Z}_{eq}$ can be derived using measured voltage $\tilde{V}_m$ and current $\tilde{I}_m$ as,

$$\begin{cases} \tilde{V}_m = \tilde{V} \\ \tilde{I}_m = \tilde{I} + \tilde{V} / X_m \\ \tilde{Z}_{eq} = R_{eq} / s + jX_{eq} = \tilde{V} / \tilde{I} \end{cases} \tag{5.10}$$

where $\tilde{V}$ and $\tilde{I}$ represent phasors of V and I. Since magnetizing reactance X_m is usually much larger than equivalent reactance X_{eq} (33 and 10 times larger for Motor I and II in Appendix A), the term $\tilde{V}/X_m$ is ignored and equations (5.10) are rewritten as,

$$\begin{cases} \tilde{V}_m = \tilde{V} \\ \tilde{I}_m = \tilde{I} \\ \tilde{Z}_{eq} = R_{eq} / s + jX_{eq} = \tilde{V} / \tilde{I} = \tilde{V}_m / \tilde{I}_m \end{cases} \tag{5.11}$$

Based on the slip equation and equations (5.11), we can have,

$$\begin{cases} \omega(t) = (1 - s(t)) \cdot \omega_s \\ \dfrac{s(t)}{s_0} = \dfrac{R_{eq} / s_0}{R_{eq} / s(t)} = \dfrac{\operatorname{Re}\left(\tilde{Z}_{eq0}\right)}{\operatorname{Re}\left(\tilde{Z}_{eq}(t)\right)} = \dfrac{\operatorname{Re}\left(\tilde{V}_{m0} / \tilde{I}_{m0}\right)}{\operatorname{Re}\left(\tilde{V}_m(t) / \tilde{I}_m(t)\right)} \end{cases} \tag{5.12}$$

where s_0, $\tilde{Z}_{eq0}$, $\tilde{V}_{m0}$, $\tilde{I}_{m0}$ represent steady state value of slip, impedance, voltage, current and $\operatorname{Re}\left(\tilde{Z}_{eq}\right)$ represents real part of impedance. So, equivalent speed at time t is estimated as,

$$\omega(t) = \left(1 - \frac{s_0 \cdot \mathrm{Re}\left(\tilde{V}_{m0}/\tilde{I}_{m0}\right)}{\mathrm{Re}\left(\tilde{V}_m(t)/\tilde{I}_m(t)\right)}\right) \cdot \omega_s \qquad (5.13)$$

Differentiate (5.13) with respect to t, $d\omega/dt$ is derived as,

$$d\omega(t)/dt = \frac{\lambda \cdot \mathrm{Re}\left(\tilde{V}_{m0}/\tilde{I}_{m0}\right)}{\left(\mathrm{Re}\left(\tilde{V}_m(t)/\tilde{I}_m(t)\right)\right)^2} \cdot \frac{d\,\mathrm{Re}\left(\tilde{V}_m(t)/\tilde{I}_m(t)\right)}{dt} \qquad (5.14)$$

where $\lambda = -s_0\omega_s$ is a constant. Using (5.13) and (5.14), the equivalent speed at time $t+\Delta t$ can be estimated as,

$$\begin{aligned} &\omega(t+\Delta t) = \omega(t) + \Delta t \cdot \frac{d\omega(t)}{dt} = \\ &\omega_s + \frac{\lambda \cdot \mathrm{Re}\left(\tilde{V}_{m0}/\tilde{I}_{m0}\right)}{\mathrm{Re}\left(\tilde{V}_m(t)/\tilde{I}_m(t)\right)}\left(1 + \frac{\Delta t}{\mathrm{Re}\left(\tilde{V}_m(t)/\tilde{I}_m(t)\right)} \cdot \frac{d\,\mathrm{Re}\left(\tilde{V}_m(t)/\tilde{I}_m(t)\right)}{dt}\right) \end{aligned} \qquad (5.15)$$

where Δt is time step. By setting Δt as zero, (5.15) can be used to estimate the current speed as (5.13). Thus, (5.15) is applied to derive equivalent motor speeds in following sections.

5.6.2.2 Transient and Steady-State Motor Input Impedances

Motor steady-state model is shown as Figure 5-5 [68].

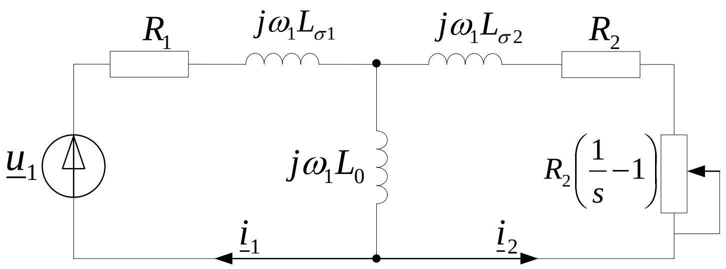

Fig. 5-5. Steady state regime equivalent circuit of induction motor

Using the equation for the rotor loop in Figure 5-5, the rotor current is related to the stator current as

$$\underline{i}_2 = -\frac{j\omega_1 L_0}{R_2/s + j\omega_1 L_2}\underline{i}_1 \tag{5.16}$$

Taking (5.16) into account, from the stator loop we can have,

$$\underline{u}_1 = \left(R_1 + j\omega_1 L_1 \frac{1+j\omega_1 \sigma s \tau_2}{1+j\omega_1 s \tau_2}\right)\underline{i}_1 \tag{5.17}$$

Thus, the input impedance of the circuit as seen from the stator terminals is obtained as

$$Z_1 = R_1 + j\omega_1 L_1 \frac{1+j\omega_1 \sigma s \tau_2}{1+j\omega_1 s \tau_2} \tag{5.18}$$

where, $L_1 = L_0 + L_{\sigma 1}$, $L_2 = L_0 + L_{\sigma 2}$, $\tau_1 = L_1/R_1$, $\tau_2 = L_2/R_2$, $\sigma_1 = L_{\sigma 1}/L_0$, $\sigma_2 = L_{\sigma 2}/L_0$,

$\sigma = 1 - 1/(1+\sigma_1)(1+\sigma_2)$.

The induction motor transient model is shown as Figure 5-6 and can be described by Equations (5.19) – (5.20) [68].

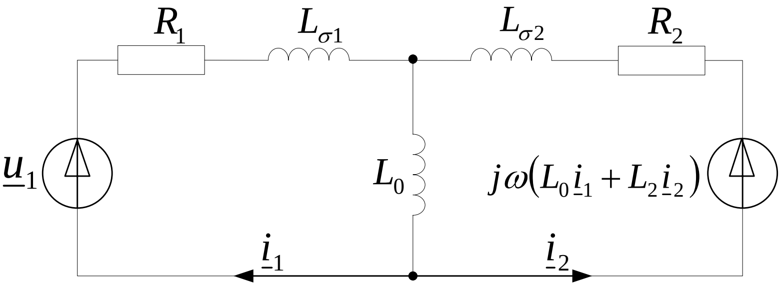

Fig. 5-6. Transient regime equivalent circuit of induction motor

$$\underline{u}_1 = R_1\underline{i}_1 + L_1\frac{d\underline{i}_1}{dt} + L_0\frac{d\underline{i}_2}{dt} \tag{5.19}$$

$$\underline{u}_2 = -j\omega L_0\underline{i}_1 + (R_2 - j\omega L_2)\underline{i}_2 + L_0\frac{d\underline{i}_1}{dt} + L_2\frac{d\underline{i}_2}{dt} \tag{5.20}$$

Using a Laplace transformation, the time domain equivalent circuit shown in Figure 5-6 can be transformed into a linear circuit in the frequency domain, as shown in Figure 5-7. Here the variable “s” stands for “Laplace complex frequency” and should not be confused with “slip”, and $\underline{\psi}_{\sigma 1} = L_{\sigma 1}\underline{i}_1(0)$, $\underline{\psi}_{\sigma 2} = L_{\sigma 2}\underline{i}_2(0)$, and $\underline{\psi}_{1m0} = L_0\underline{i}_1(0) + L_0\underline{i}_2(0)$.

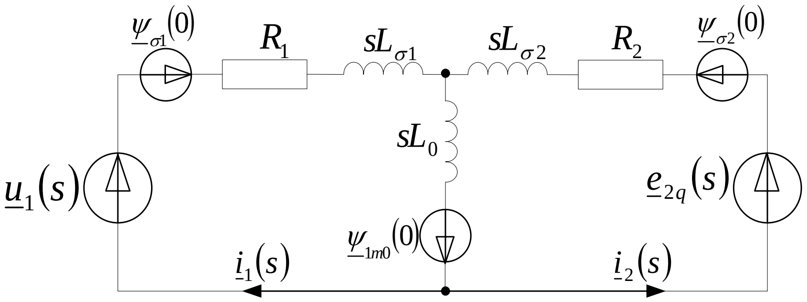

Fig. 5-7. Transient regime frequency domain equivalent circuit

The Thevenin equivalent circuit, which is derived from the frequency-domain circuit shown in Figure 5-7, is shown in Figure 5-8.

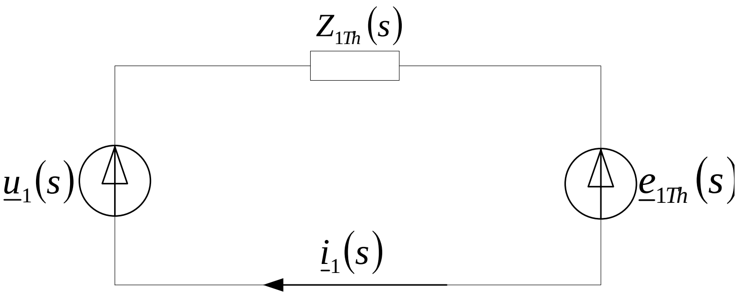

Fig. 5-8. Transient regime frequency domain Thevenin equivalent circuit

The value of the Thevenin input impedance $Z_{1Th}(s)$ and inherent voltage source $\underline{e}_{1Th}(s)$ are given as,

$$Z_{1Th}(s) = R_1 + sL_1 \frac{1+\sigma(s-j\omega)\tau_2}{1+(s-j\omega)\tau_2} \tag{5.21}$$

$$\underline{e}_{1Th}(s) = \frac{s\tau_2}{(1+\sigma_2)[1+\tau_2(s-j\omega)]}\underline{\psi}_{1m1}(0) - \underline{\psi}_{1m2}(0) \tag{5.22}$$

where, $\underline{\psi}_{1m1}(0) = \underline{\psi}_{1m0}(0) + \underline{\psi}_{\sigma 1}(0), \underline{\psi}_{1m2}(0) = \underline{\psi}_{1m0}(0) + \underline{\psi}_{\sigma 2}(0)$.

It is easy to verify that by setting the initial conditions equal to zero and by replacing $s = j\omega_1$ in Equation (5.21) we retrieve the expression for input impedance in the steady-state regime given in Equation (5.18).

5.6.3 *Kinetic Energy Derivation of Equivalent Induction Motor*

Motor kinetic energy is used to drive mechanical loads and it is decided by motor inertia and speed as follows,

$$KE = \frac{1}{2} \cdot 2H \cdot \omega^2 = H\omega^2 \tag{5.23}$$

where KE represents motor kinetic energy. H and ω are to be derived by measurement-based load modeling approach and equation (5.15) respectively using total load measurements.

5.6.4 *Relationship between FIDVR and Motor Kinetic Energy*

Based on the induction motor speed acceleration equation (5.24) and kinetic energy equation (5.23):

$$2H\frac{d\omega}{dt} = T_e - T_{load} \tag{5.24}$$

$$\Delta KE = \int (P_e - P_{load})dt \tag{5.25}$$

where T_e and P_e are electrical torque and power; T_{load} and P_{load} are mechanical torque and power; ΔKE means KE deviation.

Equation (5.25) shows the motor kinetic energy deviation is identical to the integral of power imbalance. When power imbalance is increased, KE deviation will be increased and motor speed will be decreased. Thus, the KE deviation at a bus can indicate the power imbalance caused by motor at that bus. Therefore, the connection between motor kinetic energy and bus voltage recovery has been illustrated and a large KE deviation may imply a severe FIDVR event.

Also, as indicated by NERC's report [38] and SCE's studies [39], there are mainly two critical factors that determine the susceptibility of a transmission system to FIDVR events: (1) the amount of induction motors experiencing sustained low voltage; (2) the reduced load impedance under stalled motor conditions. For factor 2, the reduced load impedance is due to increased slip (decreased speed) when motor is stalling. Seen from section 5.6.2, the motor speed estimation method is based on the calculation of motor impedance which actually takes into account factor 2. For factor 1, since speed estimation uses total load measurements, it can indicate the percentage of induction motors in total load (it will be verified in section 6.5

of chapter 6) which implies factor 1 is also involved in the equivalent kinetic energy. Thus, they further confirm the link between motor KE deviations and FIDVR.

CHAPTER 6 ONLINE DEMAND SIDE CONTROL

6.1 Introduction

In this chapter, an online demand side control strategy making use of the motor kinetic energy is proposed to disconnect the stalling motors at the transmission level. Validations of the proposed methodology are provided to show its effectiveness. The traditional UVLS is also applied to tackle the FIDVR problem as a comparison.

6.2 Online Load Shedding Strategy

According to “system protection and voltage stability” report of IEEE [63], four steps are usually involved in load shedding: (1) determination of the amount of load to be shed (2) selection of loads to be dropped (3) determination of time steps of load shedding (4) determination of voltage level at which shedding begins. For steps 1, 2 and 3, the proposed load shedding strategy applies equivalent KE to determine the amount of load shedding at each selected locations, assuming total amount of load to be shed in each step and time steps are already determined. For step 4, the predicted voltage recovery time instead of voltage level is applied as the condition to trigger load shedding actions.

The proposed load shedding strategy (LSS) applies a centralized scheme to identify the most effective loads (MEL) to shed in each step. By shedding MEL, the time needed for system voltage recovery is the shortest. The centralized scheme first receives system measurements from relays at load buses. Then, MELs are identified based on the derived KE deviations. Finally, the trip signals are sent out to shed calculated load amounts at the locations of MELs.

Two strategies (LSS-I and LSS-II) are proposed. LSS-I sheds total load at the bus with the largest KE deviation in each step; In LSS-II, total amount of load λ to be shed in each step is pre-determined and amount λ_i to be shed at each location is decided by its KE deviation percentage p_i as (6.1),

$$p_i = \Delta KE_i \Big/ \sum_{j=1}^{n} \Delta KE_j \,, \quad \lambda_i = p_i \cdot \lambda, \quad \lambda = \sum_{j=1}^{n} \lambda_j \tag{6.1}$$

Fig. 6-1 shows overall operation logic of the proposed scheme. It should be noted that the equivalent inertia is derived using previous measurements. Measurement-based load modeling is mainly conducted off-line to derive load models for dynamic simulations and it usually requires several minutes to obtain load parameters. However, the proposed scheme is aimed at providing an online fast load shedding solution to mitigate FIDVR which is in the time scale of seconds or few cycles. Therefore, considering that motor inertia has been shown to be not sensitive to variations of disturbances (section 5.6.1 of chapter 5) and relatively constant (will be further validated in section 6.4), the scheme proposes the derived equivalent inertia to calculate the current kinetic energy deviation. It is assumed there is no change of system load compositions between current and previous time.

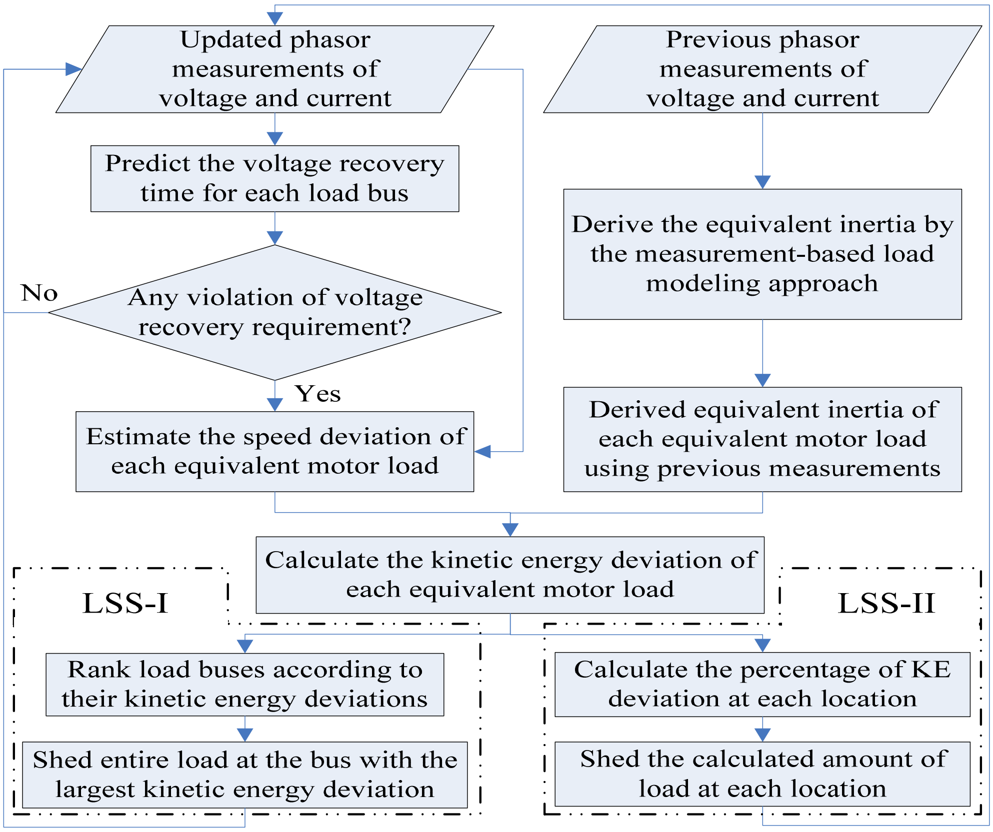

Fig. 6-1. Overall operation logic of the proposed load shedding scheme

6.3 Simulation Conditions

The following sections will elaborate on the system description, simulation objectives, validations of inertia and speed derivations, performance validations of derived kinetic energy and proposed load shedding strategy.

6.3.1 *System Description*

A sample power system in PSS/E was applied to illustrate the proposed methods and strategy. System consists of 6 generators and 23 buses including 7 load buses. Total load is 3200 MW and 1900 MVAr with 1000 MW and 400 MVAr of induction motor loads distributed between buses 153, 203, 3005, 3007 and 3008. Figure 6-2 shows one-line system diagram, whose transmission voltage ranges from 230kV to 500kV. Various shunt compensations with total amount of 950 MVAr are located at different buses throughout the system.

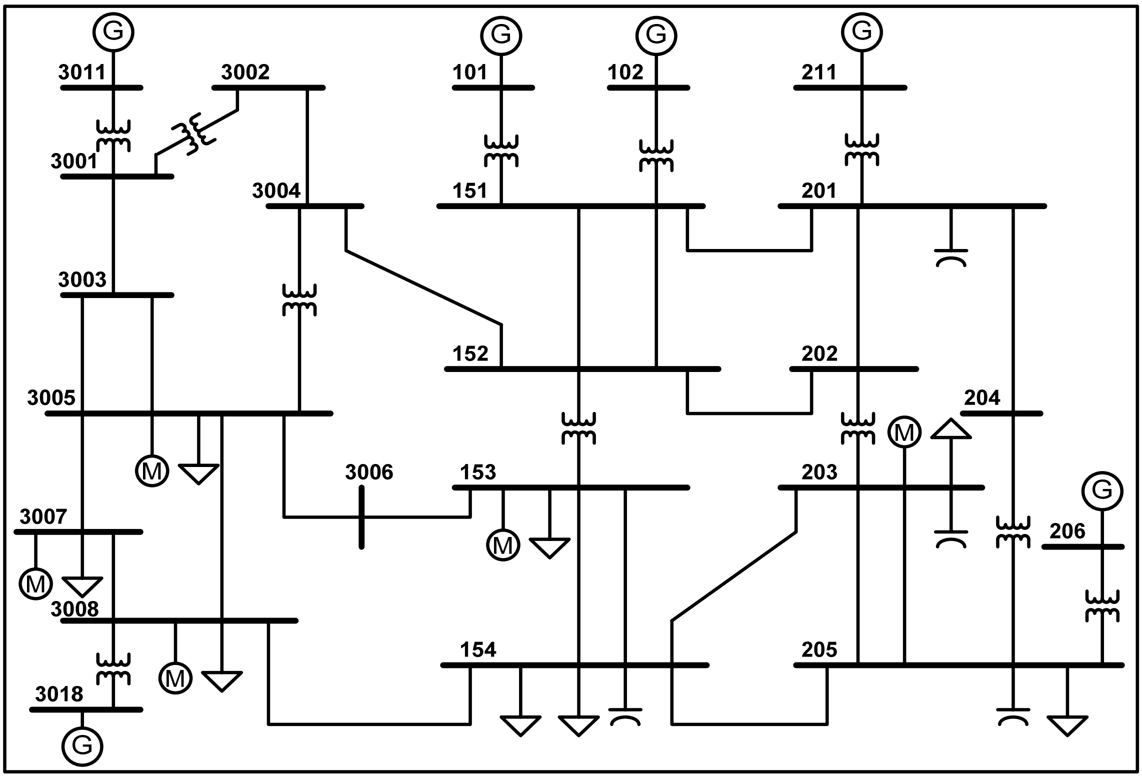

Fig. 6-2. Simulated power system with various induction motor loads

Two types of motors are applied: A/C motor (Motor I) - model C in [64]; weighted aggregate of residential and industrial motors (Motor II) - IEEE typical motor type 6 in [6]. Motor parameters are listed in Appendix A. Each bus also includes static loads modeled as constant current load for real power demand and constant impedance load for reactive power demand. Three cases with different load compositions are created and details are presented in Table 6-1, where c1, c2, and c3 represent case1, case2, and case3; I and II represent Motor I and Motor II; Motor quantity is the number of motors at each bus; each motor is 50 MW and 20 MVAr; c1, c2 and c3 have same motor type at each bus, c2 and c3 have same motor quantity at each bus, c1 and c2 have same total load MW at each bus.

Table 6-1. System load composition for three test cases

Bus No.	Motor type	Motor quantity		Total load MW		Motor percentage in the total load		
	c1,c2,c3	c1	c2,c3	c1,c2	c3	c1	c2	c3
153	I	2	2	200	150	50%	50%	67%
154	--	0	0	600	600	0%	0%	0%
203	I	2	1	200	100	50%	25%	50%
205	--	0	0	1200	800	0%	0%	0%
3005	I	2	3	200	500	50%	75%	30%
3007	II	2	2	200	250	50%	50%	40%
3008	II	2	3	200	400	50%	75%	38%

6.3.2 *Simulation Objectives*

The simulation objectives can be summarized as follows:

- to validate the inertia derivation using the measurement based load modeling approach
- to validate the speed derivation with induction motor measurements and the total load measurements
- to illustrate the incorporation of motor percentages in the speed derivation results with total load measurements
- to validate the performance of the derived kinetic energy in identifying the most effective loads to shed
- to appraise performance of the proposed load shedding strategy comparing with traditional four-stage UVLS

6.4 Validation of Inertia Derivation

Inertia has been derived for the three test cases with four faults (see Appendix B) shown in Table 6-2. Observing the first three rows, the derived inertia for each bus has some variations, which is because three cases have different system load compositions. However, comparing the last two rows, it is found the derived inertia are close to each other and they appear to be relatively constant, which is because they are based on the same system load composition even though associated with different faults. Fig. 6-3 provides load modeling results of simulated and measured load outputs for bus153 based on fault1 and fault2 in case3.

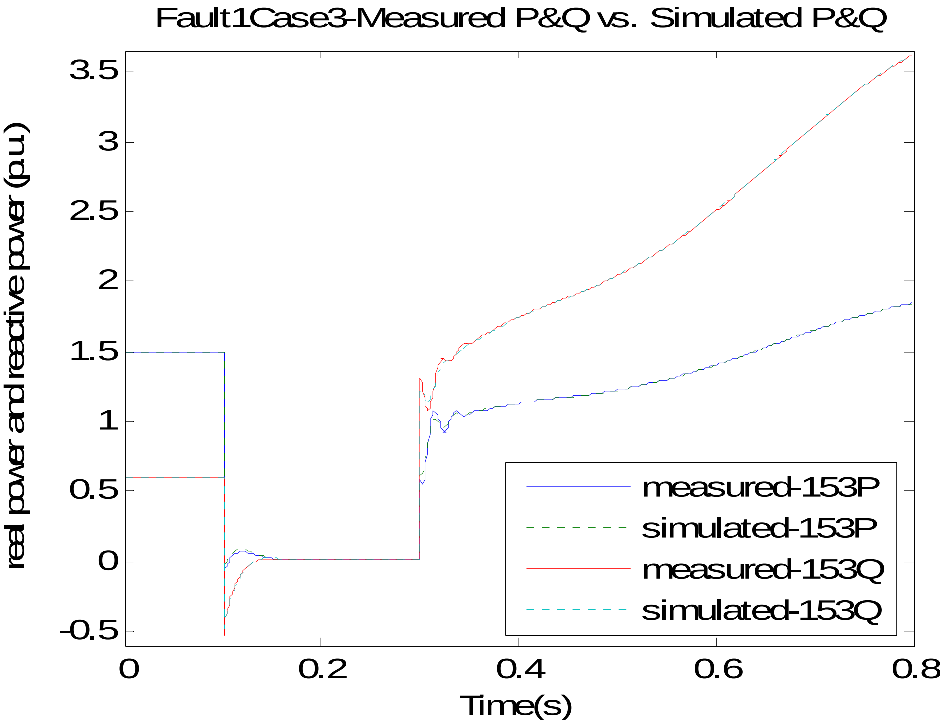

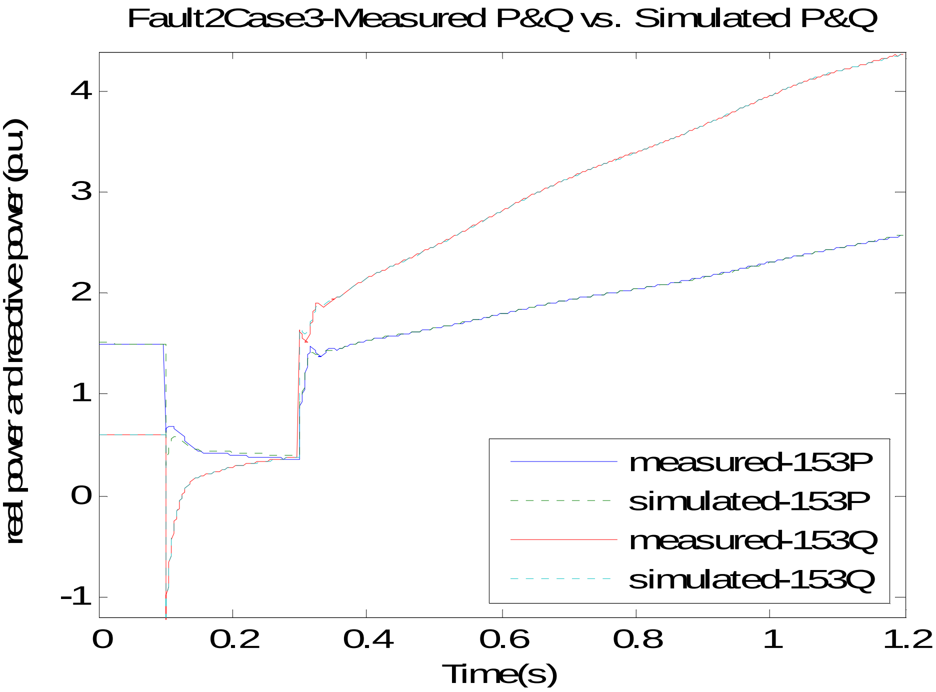

Fig. 6-3. Load modeling results for bus153 based on fault 1 and 2 in case3

Table 6-2. Derived equivalent inertia of each bus load with the four faults

Bus	153	203	3005	3007	3008
H-Case1_fault1	0.2149	0.2082	0.2114	0.8308	0.8341
H-Case2_fault1	0.1457	0.0829	0.2586	0.7006	0.8389
H-Case3_fault1	0.1522	0.0876	0.1860	0.8498	1.1926
H-Case3_fault2	0.1556	0.1175	0.1664	0.8726	1.3058

6.5 Validation of Speed Derivation

Speed was derived using induction motor measurements to validate correctness of the proposed approach and using total load measurements to prove its suitability for practical applications. Also, incorporation of motor percentages in speed derivations is illustrated using total load measurements.

6.5.1 *Speed Estimation with Induction Motor Measurements*

Using fault1 in case1, induction motor measurements of five motors were obtained and applied to derive speeds (to derive KE deviation later, speed deviation was shown instead of speed, where speed=1+speed deviation). Compared with measured motor speeds in Fig. 6-4, the derived speeds in Fig. 6-5 well captured the trend of individual motor speed variation and the relative speed between motors. Magnitudes of the derived speeds do not match the measured values since the derived speeds are approximations using only voltage and current measurements. However, derived speed magnitudes are not essential for the identifications of MELs to shed.

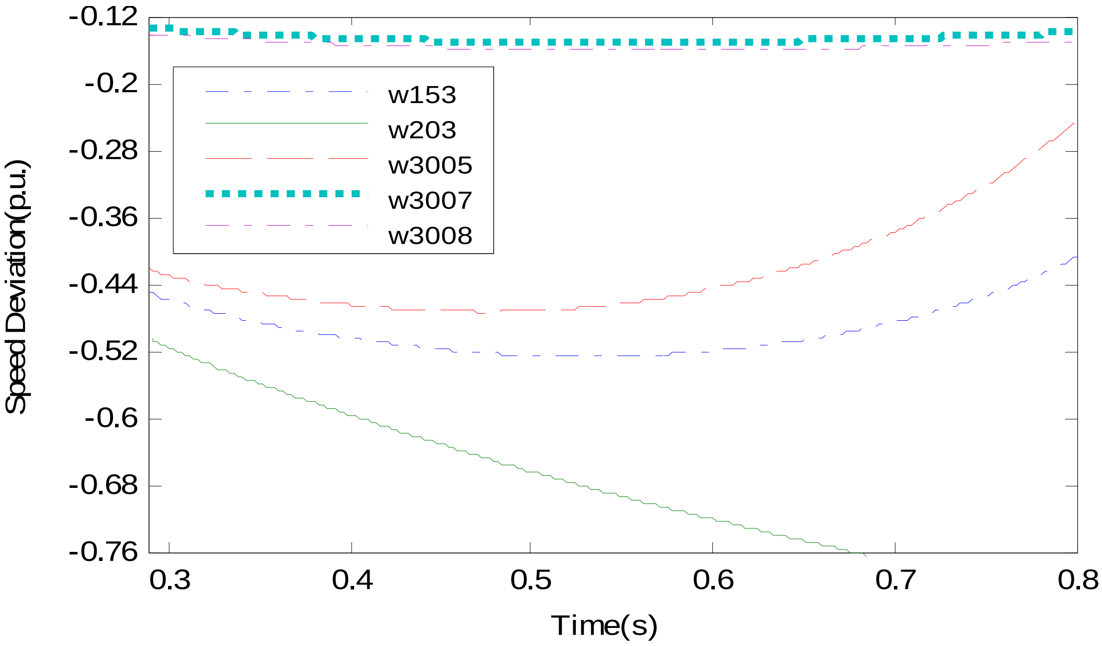

Fig. 6-4. Measured speed after fault clearing with fault1 in case1

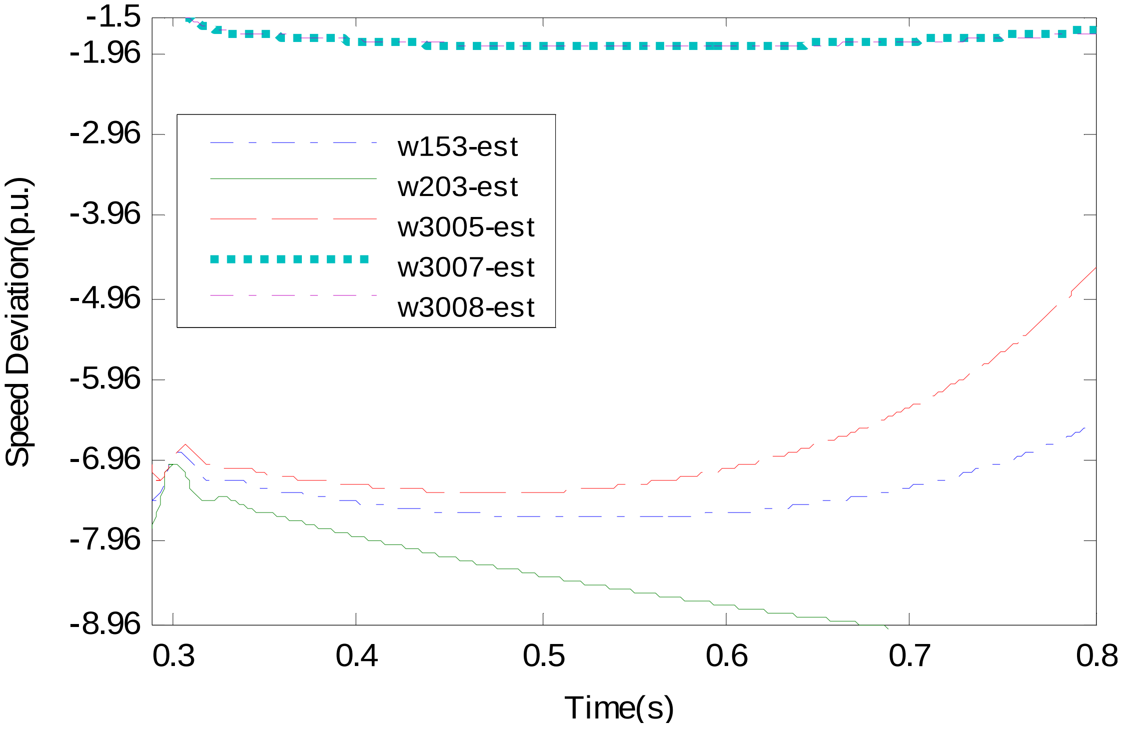

Fig. 6-5. Derived speed with induction motor measurement after fault (f1,c1)

In order to further validate the speed estimation method, following figures (Fig.6-6 to Fig.6-11) provide the measured and estimated speeds using induction motor measurements obtained from *Fault 1 in Case 2*, *Fault 1 in Case 3*, and *Fault 2 in Case 3*.

The figures from Fig.6-6 to Fig.6-11 again illustrate that the proposed speed derivation method, indeed, can well capture the trend of individual motor speed variation and the relative speed between motors. This is adequate for the identification of the most effective loads to shed to mitigate FIDVR events.

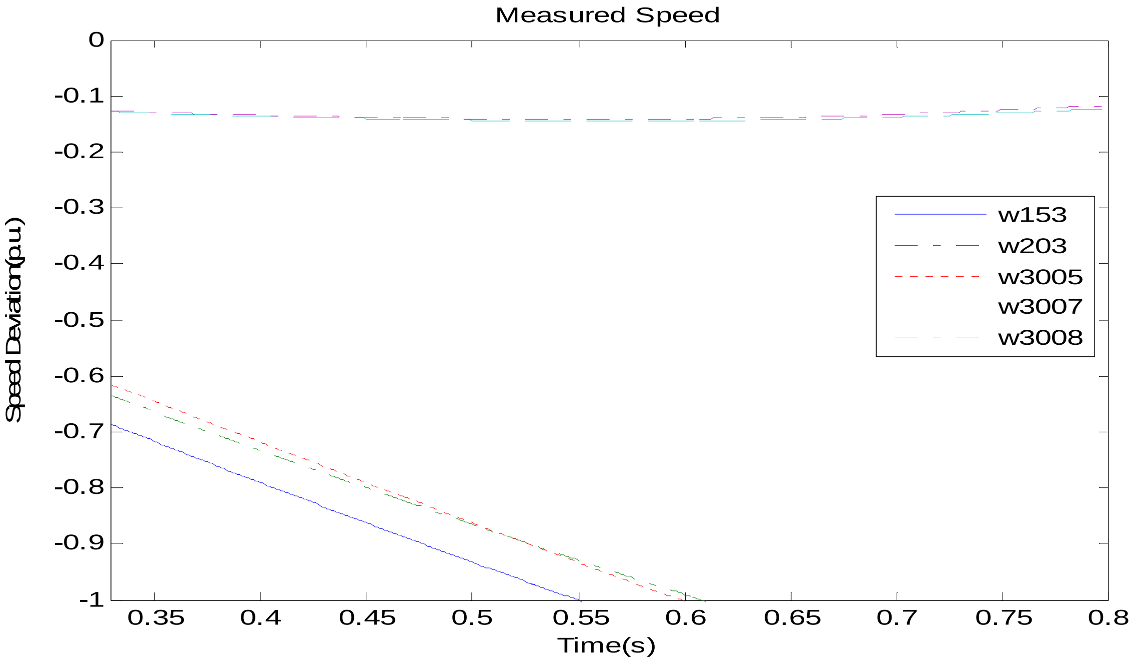

Fig. 6-6. Measured speeds after fault clearing with fault1 in case 2

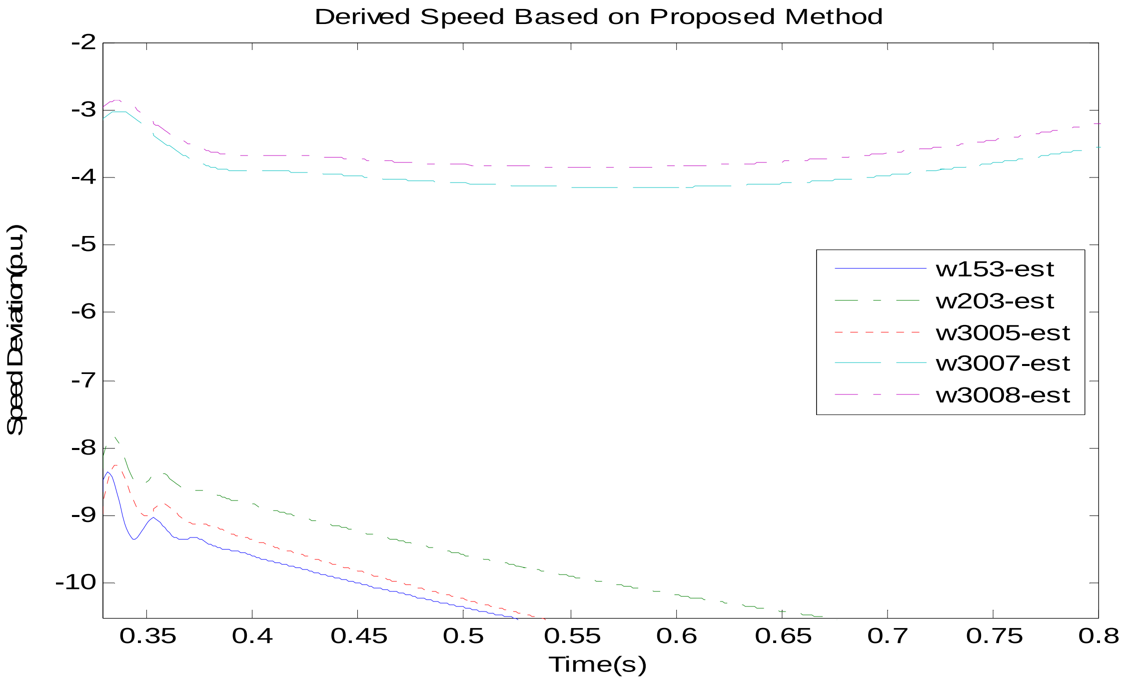

Fig. 6-7. Derived speeds after fault clearing with fault1 in case 2

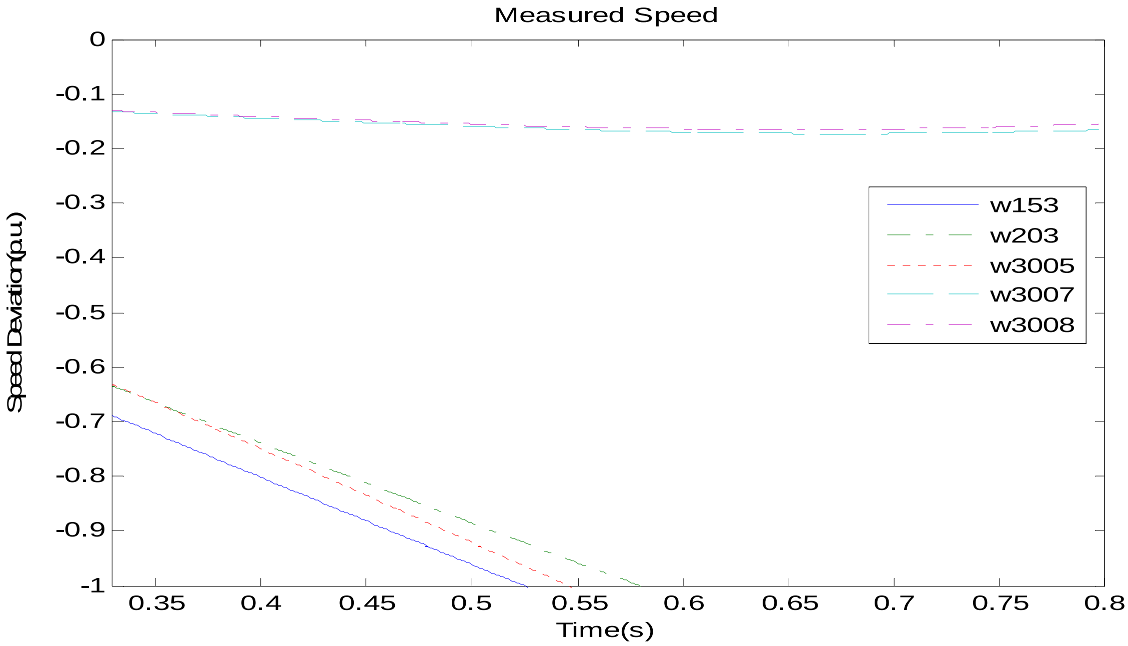

Fig. 6-8. Measured speeds after fault clearing with fault1 in case 3

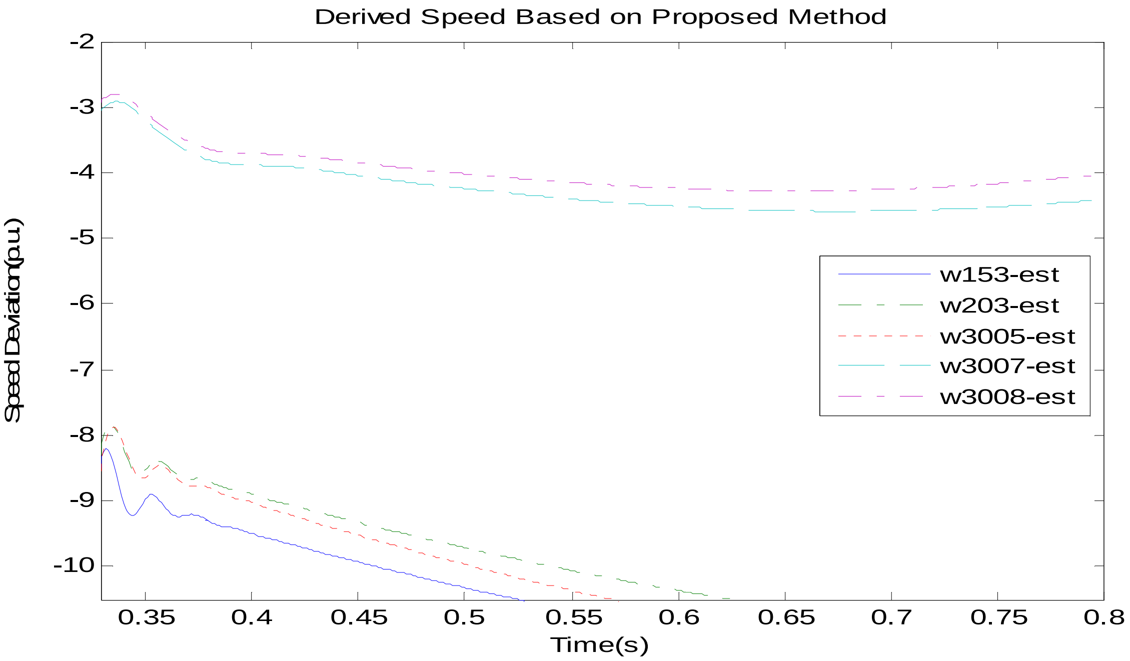

Fig. 6-9. Derived speeds after fault clearing with fault1 in case 3

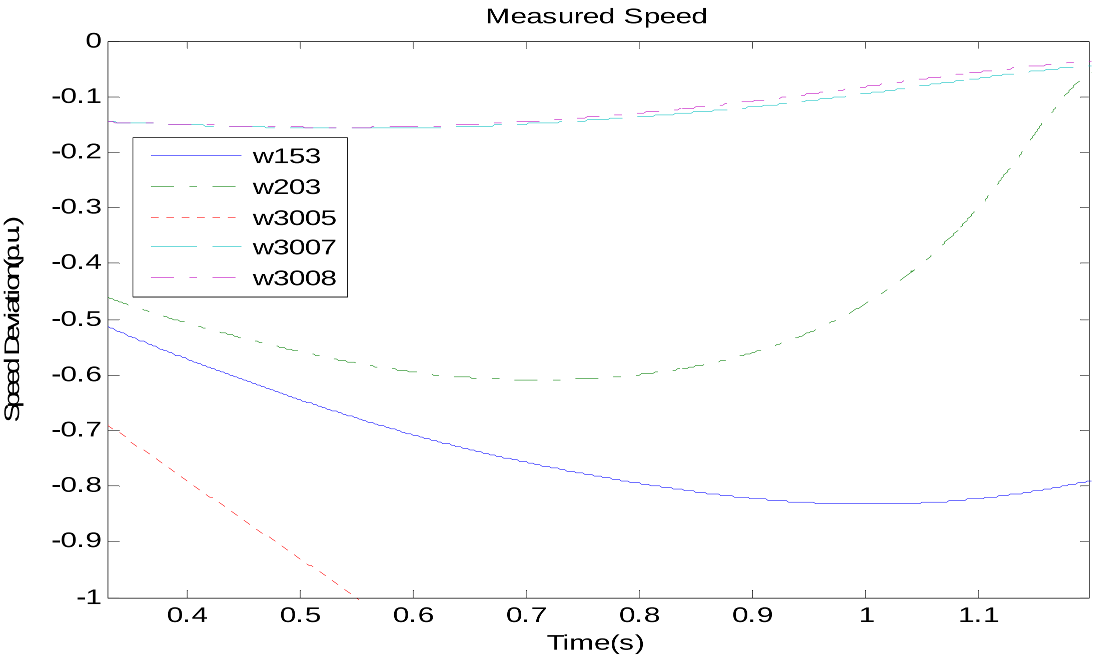

Fig. 6-10. Measured speeds after fault clearing with fault 2 in case 3

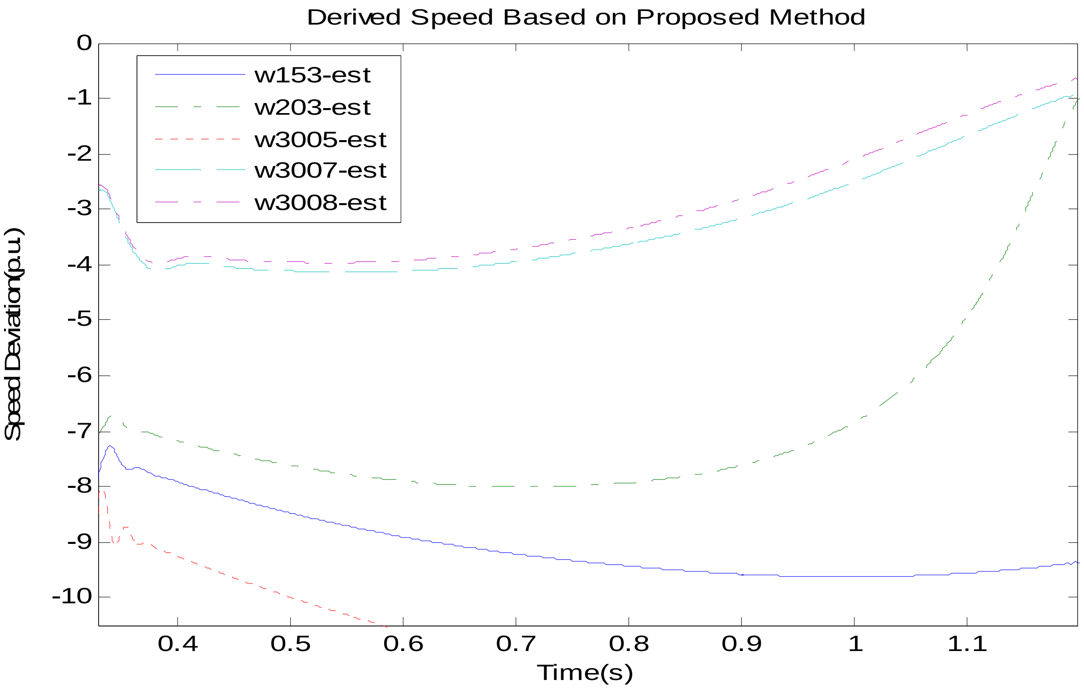

Fig. 6-11. Derived speeds after fault clearing with fault 2 in case 3

6.5.2 *Speed Estimation with Total Load Measurements*

Treating total bus load as an equivalent induction motor, total load measurements (fault1 in case1) including dynamic and static loads at all seven load buses were recorded and used to derive speeds. Fig. 6-12 presents the derived speed deviations for the seven loads before fault (fault was applied at 0.1s) and Table 6-3 provides speed deviation values at time t=0.09s. They show derived speed deviations of bus 154 and 205 are zero, because the two buses do not have any motors and thus real parts of their equivalent impedances keep constant. However, other five buses with motors did show small or large speed deviations since real parts of their equivalent impedances involve slip. Therefore, it is illustrated the derived speed using total load measurements can indicate the load buses which have no motors at all and these load buses normally are not good candidates for MELs to shed.

Fig. 6-13 shows derived speeds using total load measurements after fault clearing. Compared with Figs. 6-4 and 6-5, Fig. 6-13 shows similar trend of individual speed variation and relative speed between motors. This similarity is because each motor bus in case1 has the same load composition.

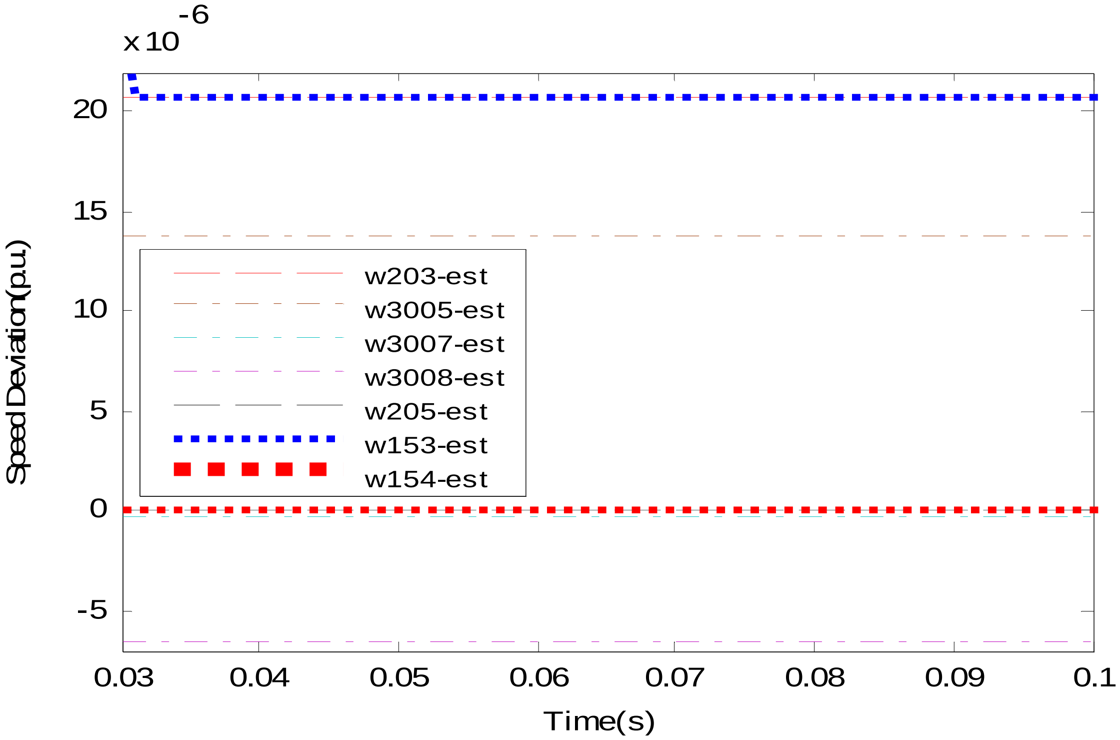

Fig. 6-12. Derived speed with total load measurements before fault (f1, c1)

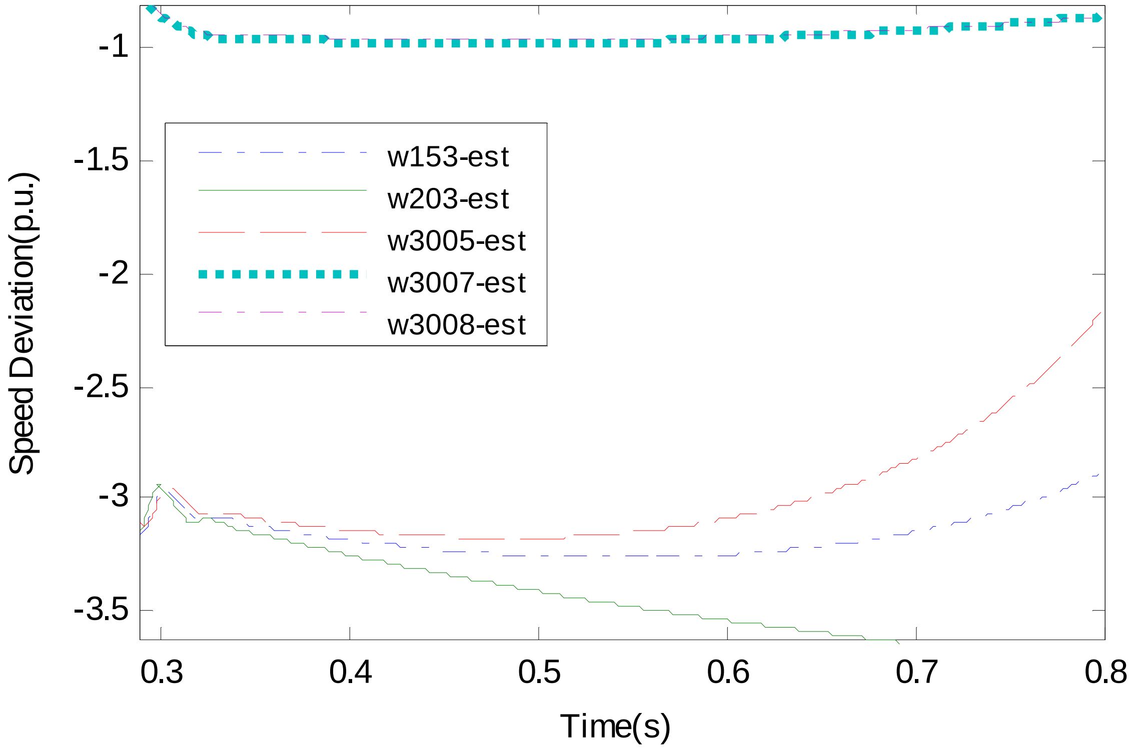

Fig. 6-13. Derived speed with total load measurements after fault (f1, c1)

Table 6-3. Derived speed deviation ϖ at time t=0.09s with fault1 in case1

Bus	153	154	203	205	3005	3007	3008
$\varpi \cdot 10^{-5}$	2.1	0	2.1	0	1.4	-0.035	-0.66

6.5.3 *Incorporation of Motor Percentages in Derived Speeds*

Using fault2 in case3, total load measurements were used to derive speeds. Comparing Fig.6-14 (measured speed) with Fig.6-15 (derived speed), the measured speed deviation of bus 3005 is always larger than that of bus 203 and the two curves have no intersection in Fig. 6-14; however, in Fig. 6-15, derived speed deviation of bus 203 is first larger than that of bus

3005 and became smaller later and the two derived speed curves did show an intersection around 1.1s. Does this mean the derived equivalent motor speeds are not correct? The answer is definitely no. The difference is because bus 203 has larger motor percentage than bus 3005. The speed derivation with total load measurements automatically incorporated the motor percentage information. Therefore, the bus with smaller motor percentage but larger actual speed deviation may have similar derived speed to that of another bus which has larger motor percentage but smaller actual speed deviation.

Above analysis illustrate the equivalent motor speeds using total load measurements. It essentially take into account motor percentages and this will help the equivalent motor KE deviation to identify the most effective loads more efficiently.

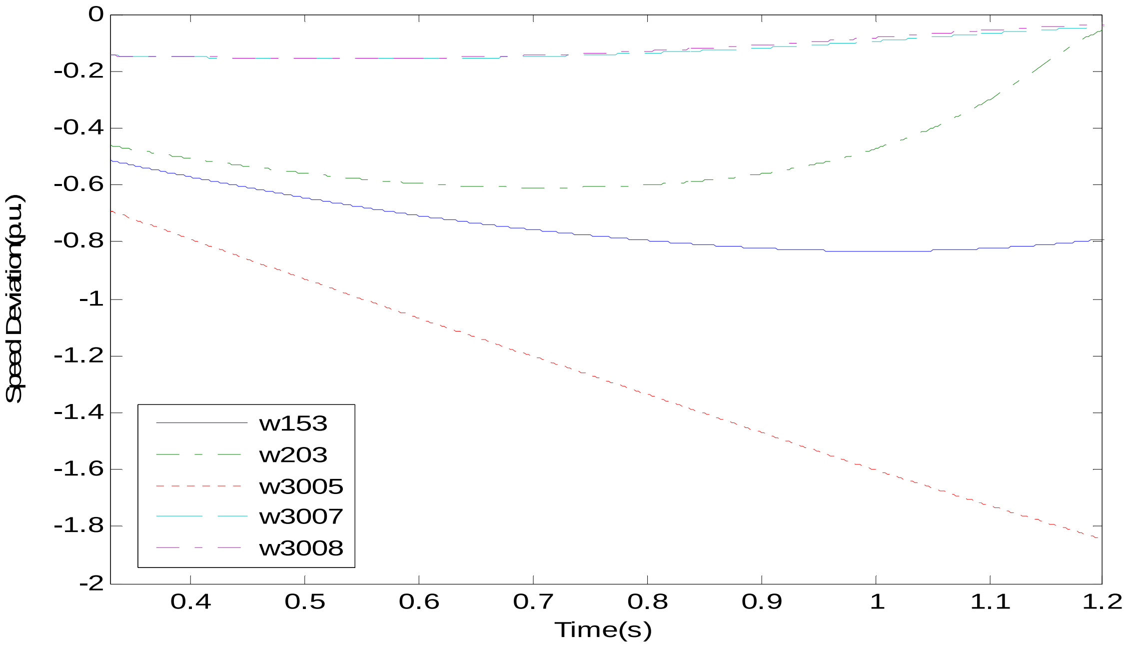

Fig. 6-14. Measured speed after fault clearing with fault2 in case3

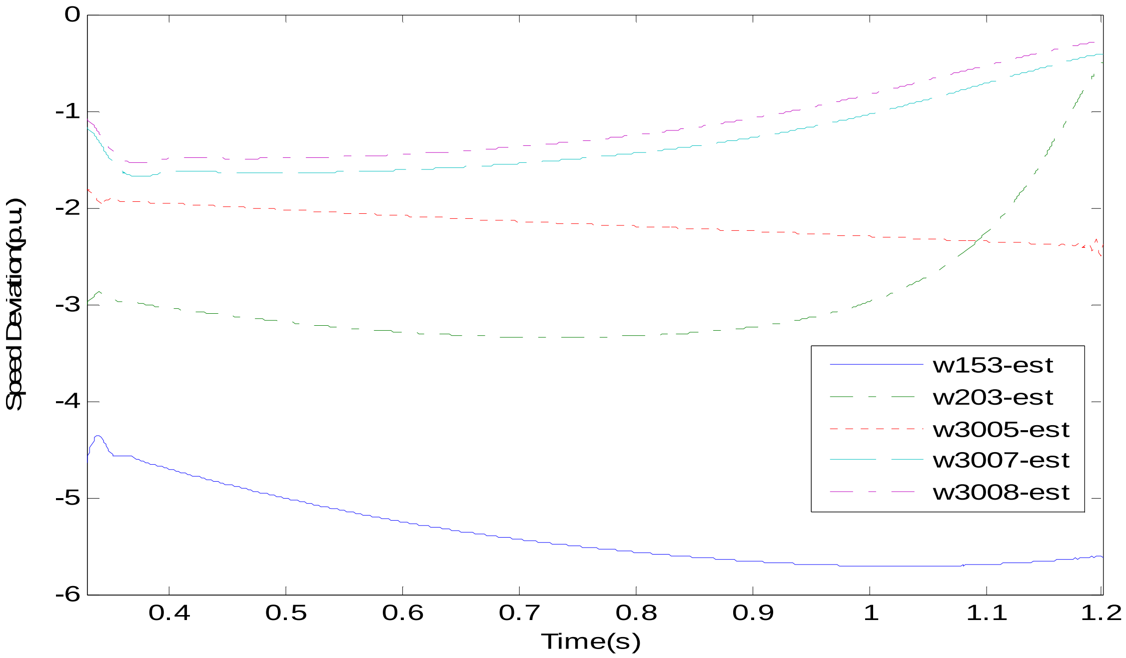

Fig. 6-15. Derived speed with total load measurements after fault (f2, c3)

6.6 Validation of Kinetic Energy Performance

Based on the derived equivalent motor speeds with total load measurements, the kinetic energy of each motor bus was calculated and its performance was illustrated and validated.

6.6.1 *Performance Validation with Fault1 in Case2*

To evaluate voltage recovery, critical recovery time (CRT) is proposed as the time needed for voltage of every load bus to recover to a pre-set value. Smaller CRT means better voltage recovery.

By looking at Figure 6-13, one could argue that the equivalent motor speed also seems to be able to indicate the MEL with fault1 in case1 (refer to “c1” in Table 6-1) where each motor bus has the same amount and percentage of motor loads. This argument will be tested in the following section using another different case.

Various load shedding were applied at 0.48s with fault1 in case2. Table 6-4 provides voltage recovery results based on CRTs. It is shown that loads at bus 3005 and 3008 are the top two MELs to shed and shedding loads at bus 3007 and 153 have the same CRT which are ranked as the third and fourth MEL. Seen from derived speeds in Fig. 6-16, bus153 shows the second largest speed deviation. However, CRT only indicates bus153 as the fourth choice for MEL. Although derived speed was able to indicate MEL with fault1 in case1, test using fault1 in case2 (refer to “c2” in Table 6-1) shows derived speed cannot properly identify MEL when motor amount and percentage of load buses are different.

However, CRT of each bus cannot be obtained for on-line fast load shedding, since it requires time domain simulations. Thus, an indicator is needed which can be derived in online environment and can reflect the CRT information of each bus.

Fig. 6-17 provides the derived KE deviations. They well indicated bus 3005 and 3008 as the top two MELs and bus 3007 and 153 as the third and fourth MEL, which are identical to the CRTs based results. It was also noted that the derived KE deviations of bus 3007 and 153 are very close, which actually is consistent with the fact that bus 3007 and 153 had the same CRT.

In summary, the simulation using fault1 in case2 validated that the derived kinetic energy of equivalent motors are able to indicate the MELs to shed but the other indicator - equivalent speed has been proved to be not appropriate to identify the MELs.

Table 6-4. CRTs of shedding various loads with fault1 in case2

Bus shed	no shed	153	203	3005	3007	3008
CRT(s)	0.897	0.655	0.714	0.586	0.655	0.627

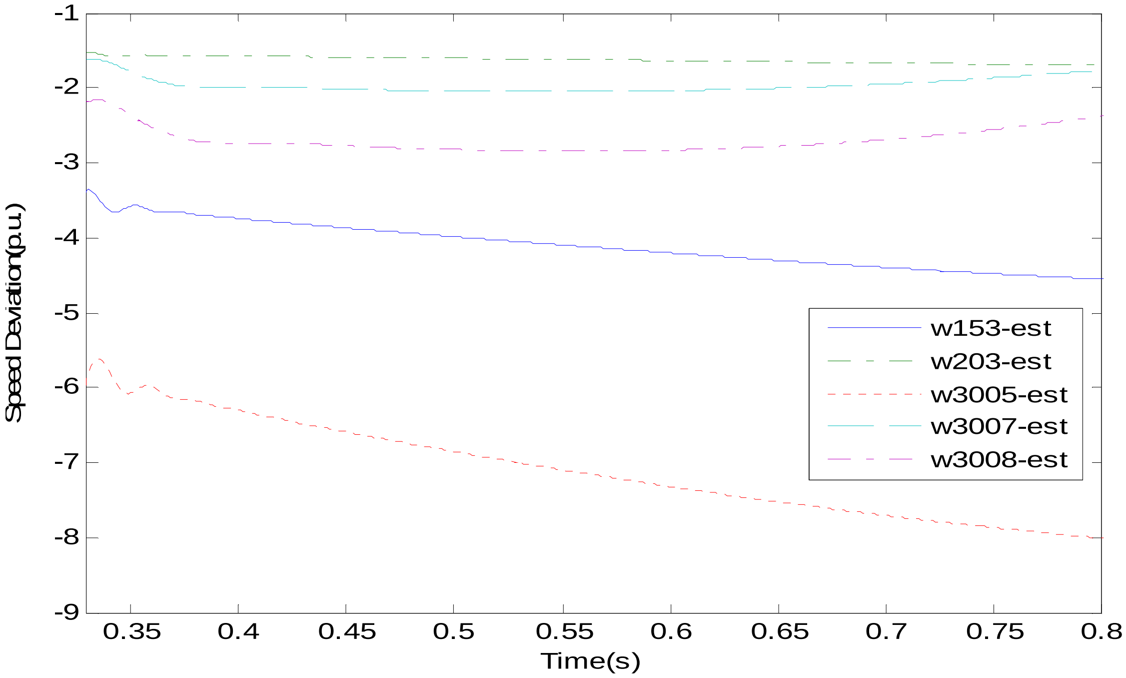

Fig. 6-16. Derived speed with total load measurements after fault (f1, c2)

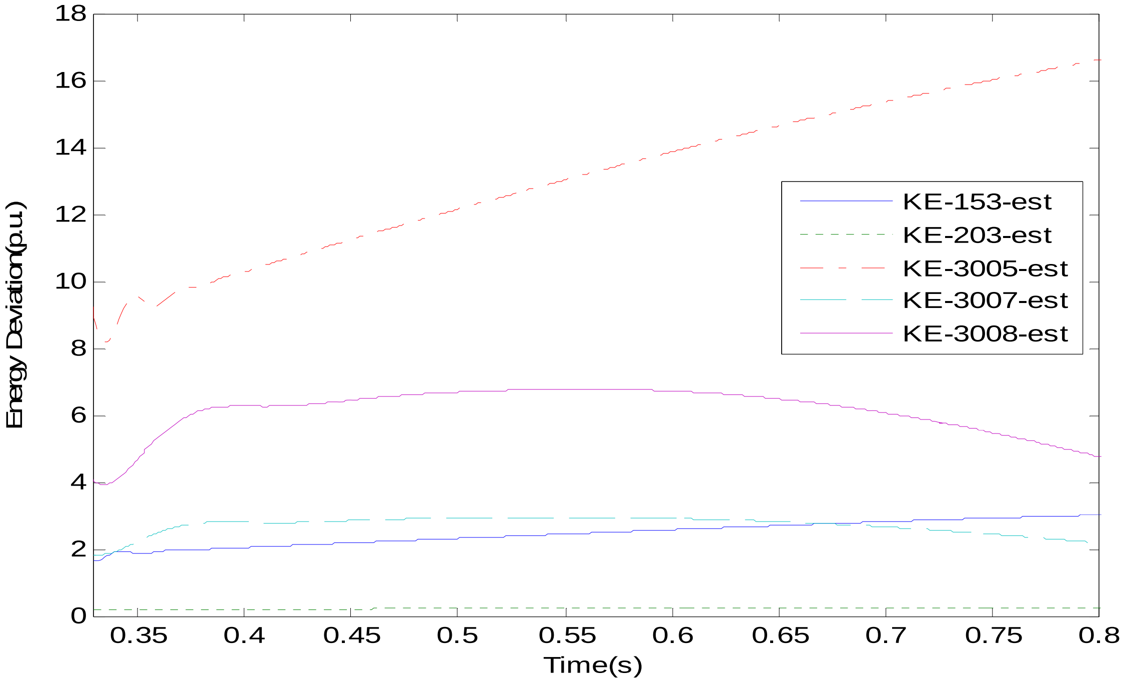

Fig. 6-17. Derived KE deviations after fault clearing with fault1 in case2

6.7 Validation of Proposed Strategy Compared to Traditional UVLS

The derived KE deviation is used to come up with two load shedding strategies to mitigate FIDVR. For comparisons, conventional four-stage UVLS was also applied as follows: Stage 1: up to 10% of area load shedding 0.05s after fault clearing; Stage 2: up to 5% of area load shedding 0.15s after fault clearing; Stages 3 and 4: identical to the second stage, except operating after 0.25s and 0.35s, respectively. Condition of triggering load shedding is similar to [48] which is based on voltage recovery time predicted using linear approximation,

$$T_{re} = T + \frac{\left(V_{set} - V_T\right) \cdot \Delta T}{\left(V_T - V_{T-\Delta T}\right)} \tag{6.20}$$

where T_{re}, T and ΔT are recovery time, current time and time interval respectively. V_T and $V_{T-\Delta T}$ are voltages at T and $T-\Delta T$, V_{set} is voltage setting (0.8 p.u.).

Table 6-5. KE deviation and percentage at t=0.35s with fault1 in case3

Bus	153	203	3005	3007	3008
KE Dev.	4.04	1.33	0.62	2.00	2.55
p_i	38.3%	12.6%	5.9%	19.0%	24.2%

Table 6-6. Results for UVLS, LSS-I and LSS-II with fault1 in case3

	Shed time	T*re*(predicted)	Shed load
UVLS	0.35s	1.1761s	320MW (10%)
	0.45s	0.8090s	160MW (5%)
	0.55s	0.6205s	160MW (5%)
LSS-I	0.35s	1.1761s	150MW (bus153)
	0.45s	0.8486s	400MW (3008)
LSS-II	0.35s	1.1761s	320MW (10%)
	T*re*(with-shed)	T*re*(no-shed)	Total load shed
UVLS	**0.5810s**	1.069s	**640MW**
LSS-I	0.5281s	1.069s	550MW
LSS-II	**0.5883s**	1.069s	**320MW**

T*re*(predicted): first-order predicted recover time before shedding;

T*re*(with-shed): recover time with shedding by time domain simulation;

T*re*(no-shed): recover time without shedding by time domain simulation.

For LSS-II, the fraction λ_i of load to be shed at each location is based on KE deviation percentage p_i from equation (6.1) and p_i are listed in Tables 6-5 and 6-7 for case3. Table 6-6 summarized shedding results of LSS-I, LSS-II and UVLS with fault1 in case3. Based on predicted voltage recovery times, UVLS applied three times of load shedding with total amount 640 MW and voltage recovery time is 0.5810s which meets the transient voltage recovery requirement (Fig. 5-3); LSS-I applied two times with total amount 550MW to get recovery time as 0.5281s and LSS-II applied only one time with total amount 320MW to get recovery time as 0.5883s.

Comparing LSS-II with UVLS, UVLS got the same voltage recovery time as LSS-II but required 100% more load to be shed than LSS-II. Comparing LSS-II with LSS-I, even though LSS-I had a faster voltage recovery (it is not necessary, since LSS-II already met voltage recovery requirement), it shed 71.9% more loads than LSS-II. Fig. 6-18 shows voltage recovery using the three strategies with fault1 in case3.

Similarly, results with fault2 in case3 are provided in Table 6-8 and Fig. 6-19. In Table 6-8, “inf” means the predicted recovery time is infinity, and s1, s2 and s3 correspond to Shed I, Shed II and Shed III in Fig. 6-19. It is shown that LSS-II achieved faster voltage recovery and required 50% less load to be shed than UVLS.

In summary, based on tests with fault1 and fault2 in case3, load shedding results using the three strategies obviously proved that the KE deviation based combined load shedding strategy (LSS-II) is able to achieve faster voltage recovery and require much less load to be shed than the traditional UVLS scheme. Therefore, LSS-II has been validated to be an effective strategy which is better than traditional UVLS scheme for online fast load shedding to mitigate FIDVR.

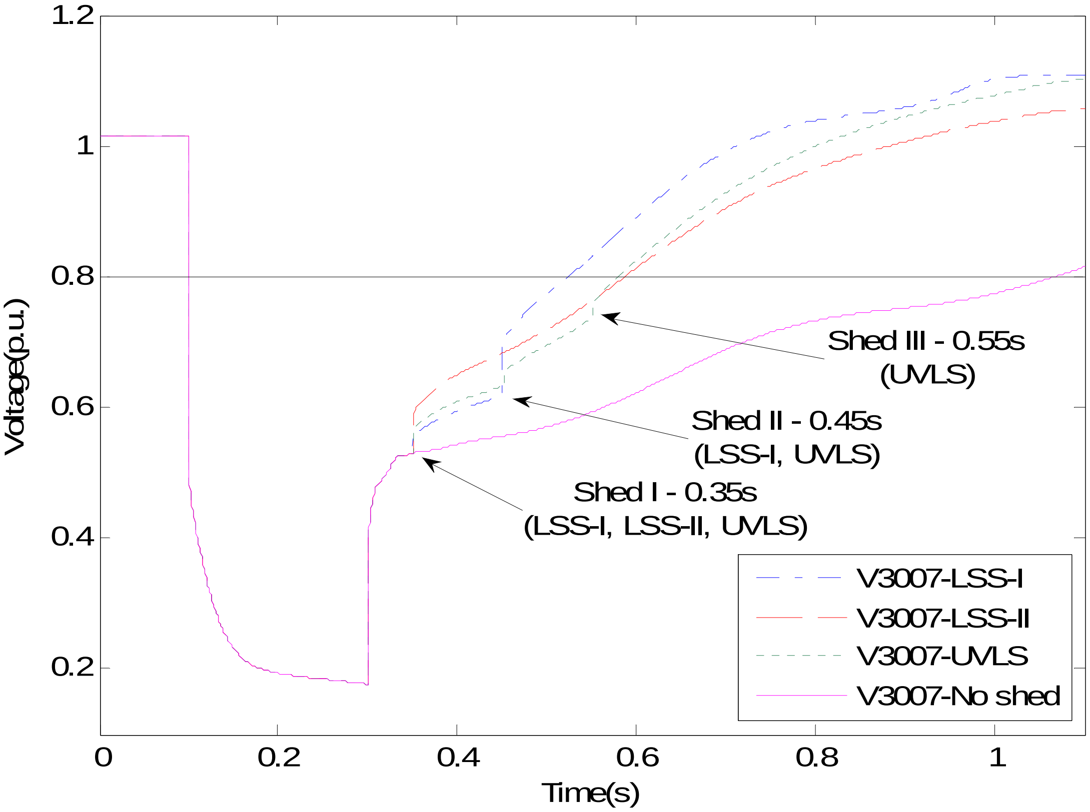

Fig. 6-18. Voltage recovery with LSS-I, LSS-II and UVLS for fault1 in case3

Table 6-7. KE deviation and percentage at t=0.35s with fault2 in case3

Bus	153	203	3005	3007	3008
KE Dev.	3.21	1.01	0.60	1.99	2.56
p_i	34.3%	10.8%	6.4%	21.2%	27.3%

Table 6-8. Results for UVLS, LSS-I and LSS-II with fault2 in case3

	Shed time	T*re*(predicted)	Shed load
UVLS	0.35s (s1)	Inf	160MW (5%)
	0.45s (s2)	0.7921s	160MW (5%)
	0.55s (s3)	0.6229s	160MW (5%)
LSS-I	0.35s	Inf	150MW (bus153)
	0.45s	0.6658s	400MW (3008)
LSS-II	0.35s	Inf	160MW (5%)
	0.45s	0.6894s	160MW (5%)
	T*re*(with-shed)	T*re*(no-shed)	Total load shed
UVLS	**0.5717s**	0.9452s	**480MW**
LSS-I	0.4596s	0.9452s	550MW
LSS-II	**0.5322s**	0.9452s	**320MW**

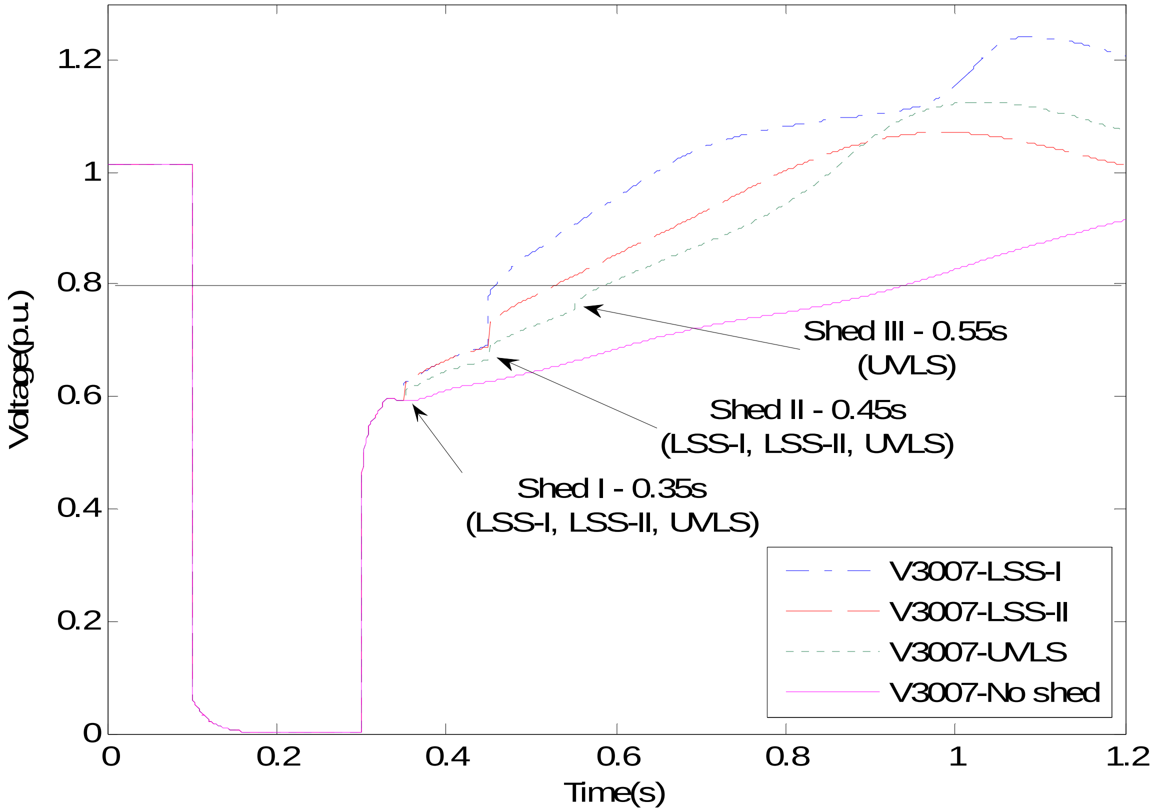

Fig. 6-19. Voltage recovery with LSS-I, LSS-II and UVLS for fault2 in case3

6.8 Summary

Kinetic energy based online load shedding scheme for mitigating fault-induced delayed voltage recovery has been proposed. The kinetic energy is derived using equivalent motor inertia and equivalent motor speed.

Equivalent motor inertia was obtained by measurement based load modeling [59]. Through trajectory sensitivity studies, it has been shown that motor inertia has a very small sensitivity to measurement variations. The derived inertia could be applied over a relatively wide variety of disturbances.

Equivalent motor speed was estimated using motor steady state model. Test with induction motor measurements validated correctness of the proposed approach. Test using total load measurements proved its suitability for practical applications and illustrated that derived speeds automatically took into account motor percentage information.

Analysis has revealed that motor KE deviation is identical to the integral of power imbalance, which indicates the connection between KE deviations and system transient voltage recovery. Furthermore, load shedding results have validated this approach can properly determine MELs to shed.

Two load shedding strategies were proposed: LSS-I sheds entire loads at the bus with the largest KE deviation in each step and LSS-II sheds combined loads at various buses based on their KE deviation percentages in each step. The proposed strategies have been investigated, illustrated, and validated by simulations performed on a sample system. It has been shown that LSS-II is, indeed, able to identify the most effective load shedding locations and load shedding amount at each location for mitigating FIDVR. In comparison with traditional four-stage UVLS scheme, the proposed LSS-II can achieve faster voltage recovery and require much less load to be shed. It provides an effective and efficient online solution using load shedding to mitigate FIDVR events.

This novel online load shedding strategy is a very desirable and valuable complement to fast voltage collapse prevention and short-term voltage stability control.

CHAPTER 7 PRACTICAL APPLICATION TO MITIGATE FIDVR

7.1 Introduction

In this chapter, several issues regarding the practical implementation of the proposed online demand side control for FIDVR mitigation are tackled and discussed. It includes the voltage recovery versus different fault clearing time and fault locations, study of incorporating UVLS relay in large induction motors, load shedding comparison between ZIP and Motor loads, practical implementation of the proposed method to large power systems and comparison with traditional UVLS scheme.

7.2 Voltage Recovery versus Fault Clearing Time and Location

7.2.1 *Simulation System and Load Compositions*

The 9-bus test system was obtained from the small size test system applied by ERCORT for the short-term system stability criteria studies [66], as shown by Fig. 7-1. It includes two generators and three load buses with each bus connected with both static loads and dynamic loads. Adequate reactive power compensation has also been incorporated in the test system. This small test system will be used to study the voltage recovery under different fault conditions and the impact of incorporating UVLS relay in the large industrial induction motors.

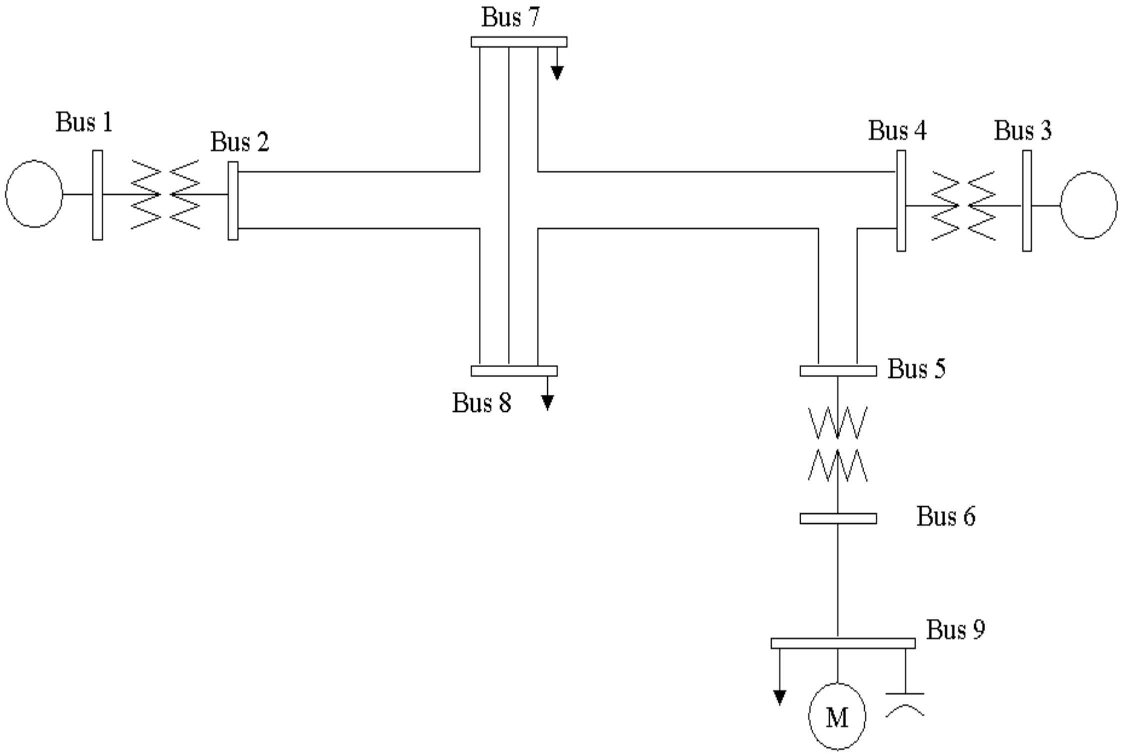

Fig. 7-1. One-line diagram of simulation system

The three load buses all have static loads and induction motor loads. Two types of motors are applied: air conditioner motor (Motor I) - model C in [64]; weighted aggregate of residential and industrial motors (Motor II) - IEEE typical motor type 6 in [6]. The remaining loads at each bus are represented by the constant impedance (Z) load. Bus 7 has both types of induction motor loads (Motor I and II), while bus 8 has motor II connected and bus 9 has motor I connected. The load compositions of the test system are summarized in Table 7-1.

Table 7-1. System load compositions

Bus	Motor Type	Motor MW; Per.	Motor MVar; Per.	Z Load MW; Per.	Z Load MVar; Per.
7	I&II	100; 42%	40; 54%	137; 58%	34; 46%
8	II	50; 42%	20; 54%	69; 58%	17; 46%
9	I	50; 48%	20; 48%	55; 52%	22; 52%

7.2.2 *Voltage Recovery versus Fault Clearing Time*

In order to show the effects of fault clearing time on the voltage response (voltage recovery) after fault is cleared, a three phase short circuit fault was applied at bus 7 and started at 0.05s. Figures 7-2, 7-3 and 7-4 shows the three sets of voltage responses with respect to three different fault clearing time at 0.2s, 0.3s, and 0.4s, respectively. In each set, the voltage recovery trajectories of two generator buses and three load buses are plotted.

As shown in Figure 7-2, the two generator voltages recover to 0.8p.u. in less than 2 seconds with 0.2s fault clearing time and it meets the generator voltage recovery criterion. Thus, the two generators will not be tripped by their protection systems. However, Figures 7-3 and 7-4 show that the longer fault clearing time causes voltage recovery to be delayed further. Therefore, one generator will be tripped with 0.3s fault clearing time and two generators will be tripped with 0.4s fault clearing time.

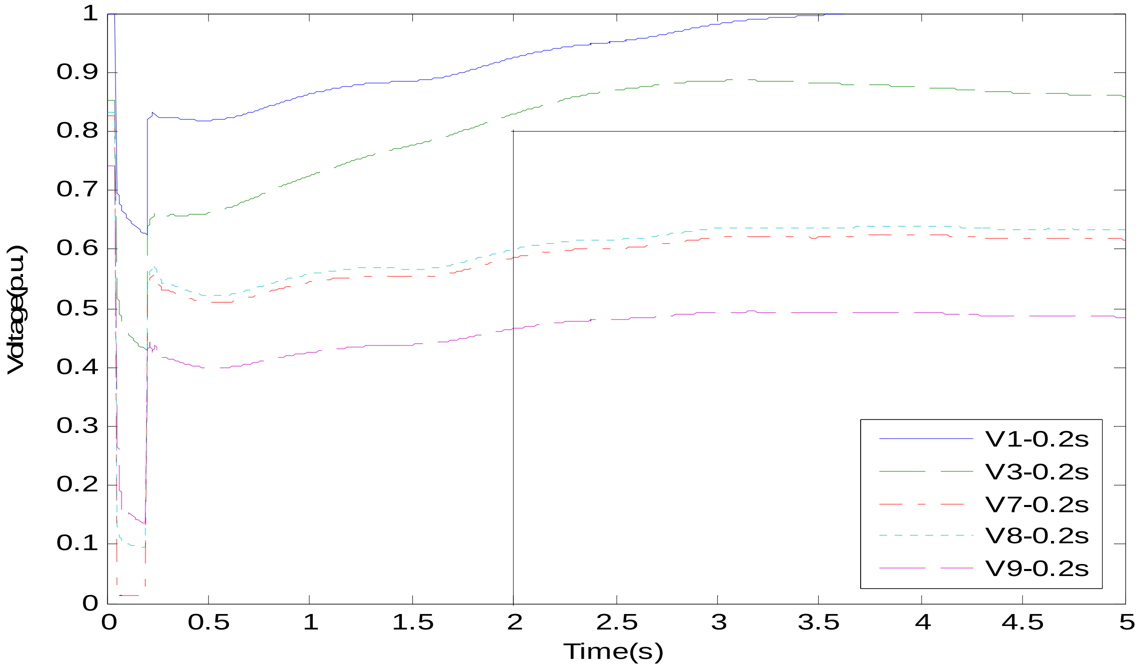

Fig. 7-2. Voltage recovery trajectories with 0.2s fault clearing time

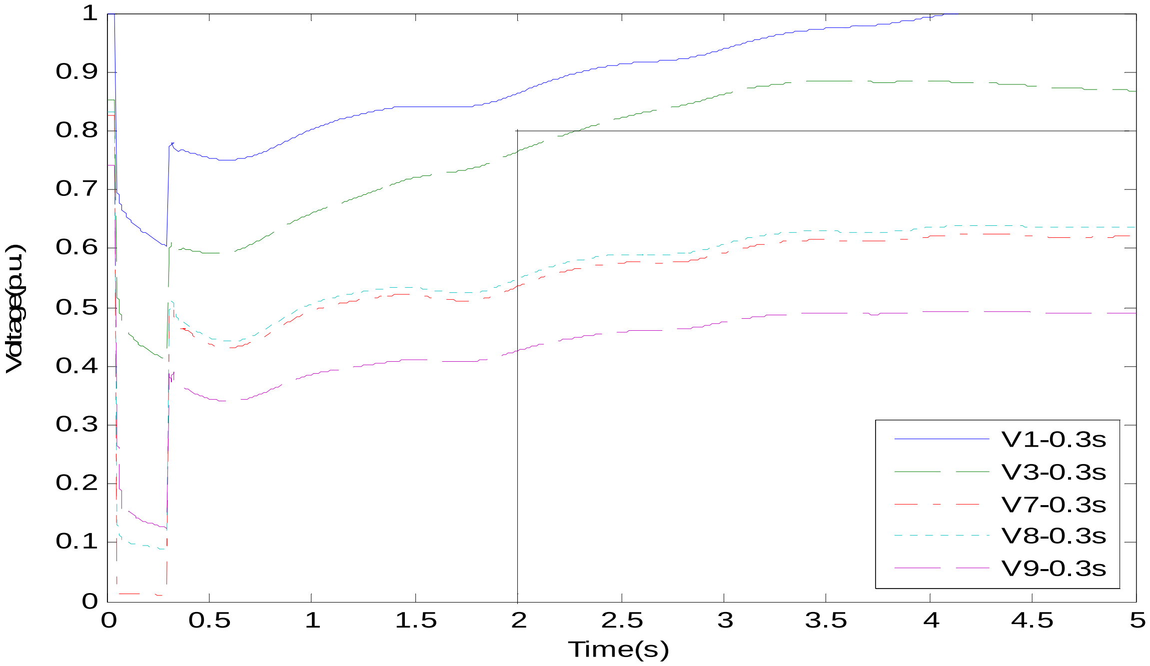

Fig. 7-3. Voltage recovery trajectories with 0.3s fault clearing time

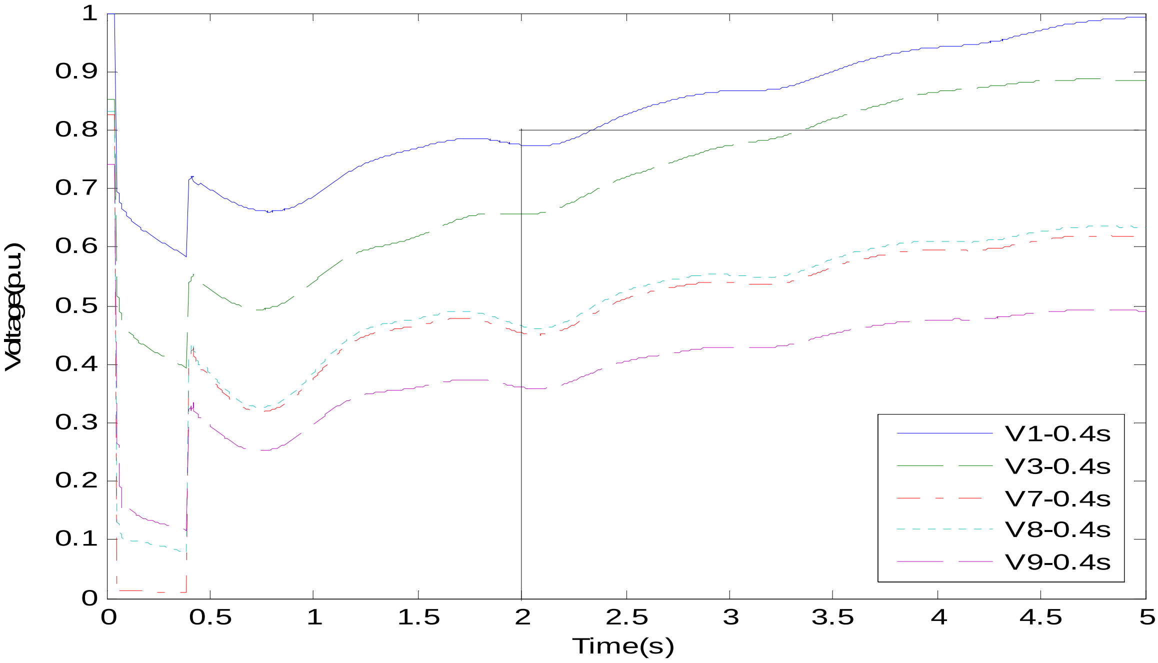

Fig. 7-4. Voltage recovery trajectories with 0.4s fault clearing time

It has been shown that fault clearing time is an important factor to affect the voltage recovery trajectory. Generally, a longer fault clearing time will more severely delay the voltage recovery process. Thus, the fault clearing time should be considered when developing control methods for the real-time online FIDVR mitigation.

7.2.3 *Voltage Recovery versus Fault Location*

Different fault locations can cause fault to occur at different voltage levels, close to generators or loads, at loads with different amounts or load compositions, at different line loading conditions, at buses with different reactive power compensation capabilities.

Therefore, fault location is another key factor to affect voltage responses after fault is cleared and different fault locations usually lead to various voltage recovery situations.

Using the 9-bus test system from ERCOT, three faults at buses 7, 8, and 9 were applied to investigate the effects of fault locations on the voltage recovery. The three faults are the same in terms of the fault starting time, fault clearing time, and fault impedance. However, they are different in term of the fault location, which means that they occurred at different voltage levels (bus 7 and 8 are at 138kV, bus 9 is at 13kV), with different electrical distances to generators (bus 7 and 8 are closer to generators than bus 9), at loads with different amounts and load compositions. Figures 7-5 and 7-6 show the two sets of voltage responses with respect to two different fault locations at bus 8 and 9.

It can be seen that, for the same fault clearing time of 0.4s, with the faults at bus 7 (Fig. 7-4) and bus 8 (Fig. 7-5), the two generators’ voltages could not recovery to 0.8 p.u. within 2 seconds. However, the fault occurred at bus 9 let the voltages of the two generators recover to 0.8p.u. in 2 seconds as seen in Fig. 7-6. Therefore, the fault location indeed can greatly affect the voltage recovery process and should also be tackled in the real-time online FIDVR mitigation.

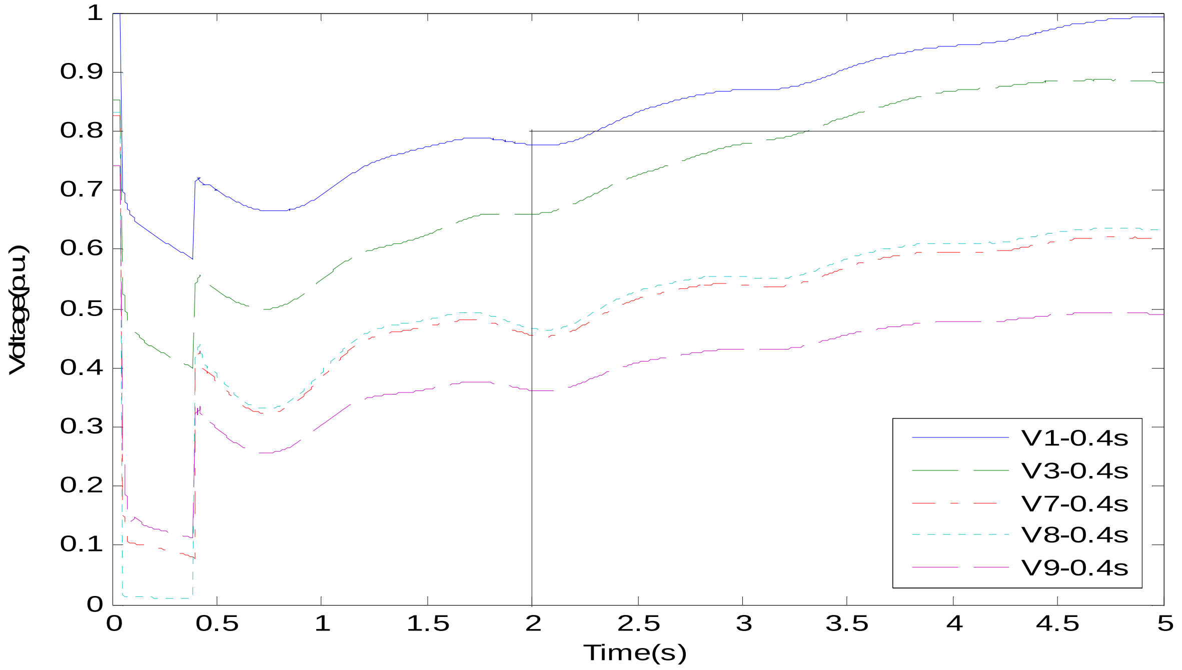

Fig. 7-5. Voltage recovery trajectories with fault location at bus 8

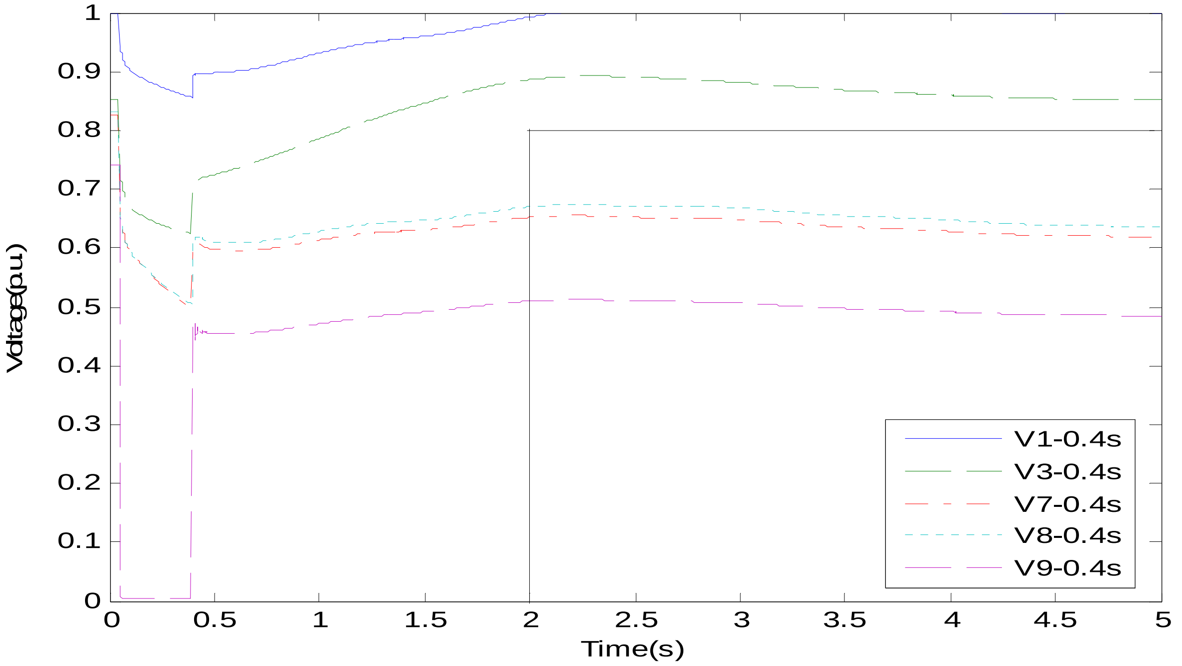

Fig. 7-6. Voltage recovery trajectories with fault location at bus 9

In summary, the above results of studying the voltage recovery trajectory under different fault conditions have shown that the fault clearing times and fault locations can greatly impact the voltage recovery.

Since the proposed online demand side control scheme applies motor kinetic energy information to control the distributed controllers (relays) throughout the system, the timing, location and amount of control can be adjusted according to different fault conditions. This adaptive control feature of the proposed demand side control scheme provides a great advantage over supply side control methods for practical FIDVR mitigation in a real-time online environment.

7.3 Three Phase Induction Motor with UVLS Relay

In the large practical power system, the transmission substation usually connects both 3-phase and single phase induction motors. The typical representative for 3-phase induction motors is the large industrial induction motor which normally includes under-voltage load shedding relay to trip the motor under low voltage conditions. The typical representative for single phase induction motors is the air conditioning motor which does not have under-voltage load shedding relay but only has thermal protection relay.

Since the large three phase induction motors have relatively large inertia and are equipped with UVLS relays, they are not easy to stall and could be disconnected by UVLS relay if stalling occurs. Therefore, the large three phase induction motors usually are not the cause for the delayed voltage recovery events. The real cause of the delayed voltage recovery occurred in many southern states of U.S. is the single phase small induction motors which have relatively small inertia and can stall quickly in response to low voltage conditions. Since these small induction motors only have thermal protection relay, it takes 3 to 20 seconds to trip the motor.

In Chapter 6, both large industrial induction motor (Motor II in Section 6.3.1) and small residential induction motor (Motor I in Section 6.3.1) have been included. However, UVLS relay has not been incorporated in the large industrial induction motors, since Chapter 6 focused on the load shedding strategy using the KE deviation information to identify the most effective load shedding locations and the amount to be shed at each location.

In this chapter, we incorporated the UVLS relay in large induction motor to evaluate the online demand side control for FIDVR mitigation. In order to set the under-voltage load shedding relay equipped within the three phase induction motor, the following criterion from reference [65] is applied. “Based on the typical time-voltage characteristics of an Under-Voltage Relay, for 70% of tap setting, the time ranges from about 0.8 second to about 9 seconds, which is a reasonably wide range for a wide area of applications.” Therefore, the UVLS relay is set to trip the motor if the voltage is sustained below 0.7p.u. for more than 48 cycles (0.8 second) and the operation time for circuit breaker is 3 cycles.

7.3.1 *Simulation Results*

For comparison, the voltage recovery curves with and without the large motor UVLS relays are provided, as shown in Figures 7-7 and 7-8.

Comparing Figure 7-7 with Figure 7-8, we can see that the voltages recover faster with the UVLS relay equipped with the large induction motor. It is because the UVLS relays tripped the large induction motors at buses 7 and 8 in response to the low voltage condition and this avoids the large amount of reactive power demanded by the stalling motors and thus the voltage recovery is faster. On the other hand, since no UVLS relay was equipped with the large motors, additional large amount of reactive power was required from the stalling motors and this greatly delayed the voltage recovery process and increased the risk of fast voltage collapse. Therefore, incorporating the UVLS relay in the large motors will reduce the probability of having delayed voltage recovery events.

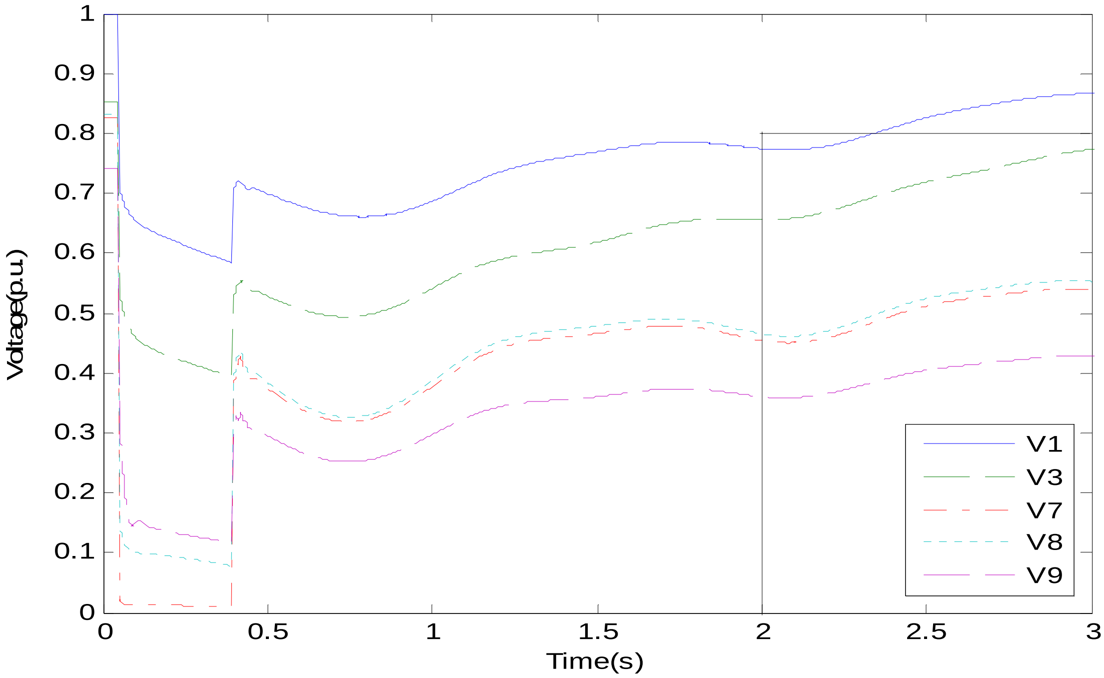

Fig. 7-7. Voltages recovery without UVLS equipped in large motors

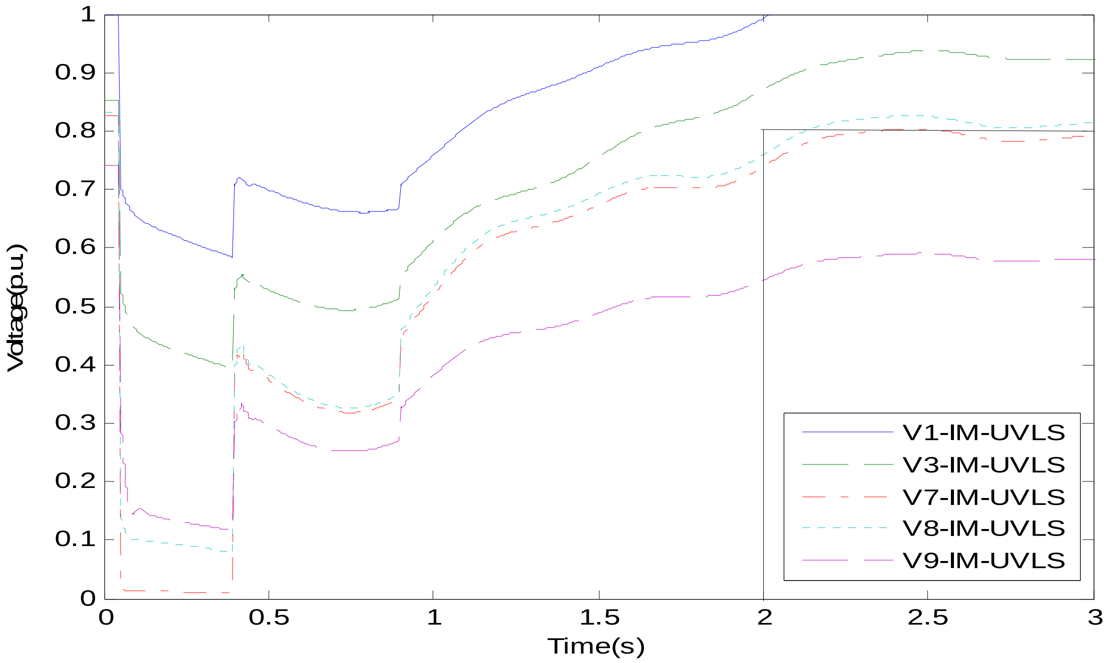

Fig. 7-8. Voltages recovery with UVLS equipped in large motors

7.4 Demand Side Control with Motor UVLS Relay

From Figure 7-8, it can be seen that even though the UVLS relay in large motors tripped them under low voltage conditions, the voltage recoveries of buses 7, 8, and 9 are still delayed. Therefore, the traditional UVLS and proposed online demand side control strategy are applied to mitigate the delayed voltage recovery at buses 7, 8 and 9.

7.4.1 *Simulation Results*

In Figure 7-9, it is shown that the traditional UVLS applies three stages of load shedding to recover the voltage of bus 9 (slowest recovery bus) to 0.7 p.u. in 4s, which did not meet the requirement of recovering to 0.8 p.u. in 4s. Thus, the proposed online demand side control strategy is also applied to mitigate the FIDVR event.

In Figure 7-10, it is shown that the proposed KE based scheme applies only two stages of load shedding to recover the voltage of bus 9 to 0.82 p.u. in 4s, which met the requirement.

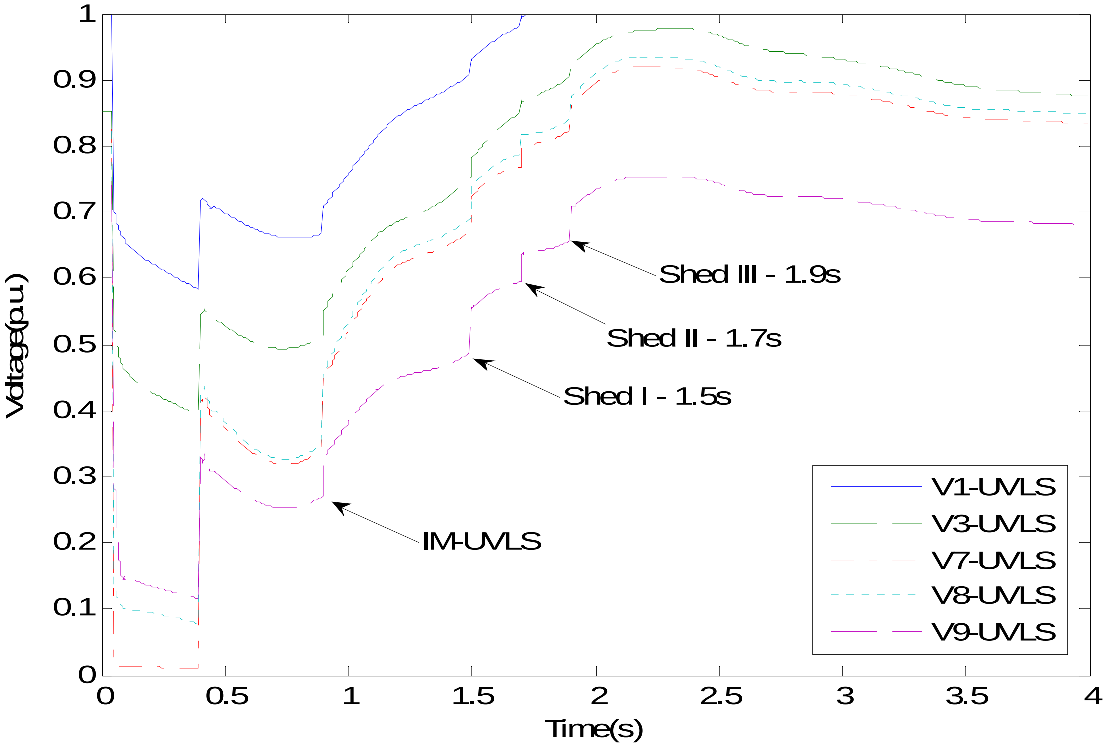

Fig. 7-9. Voltages recovery with IM-UVLS and traditional UVLS

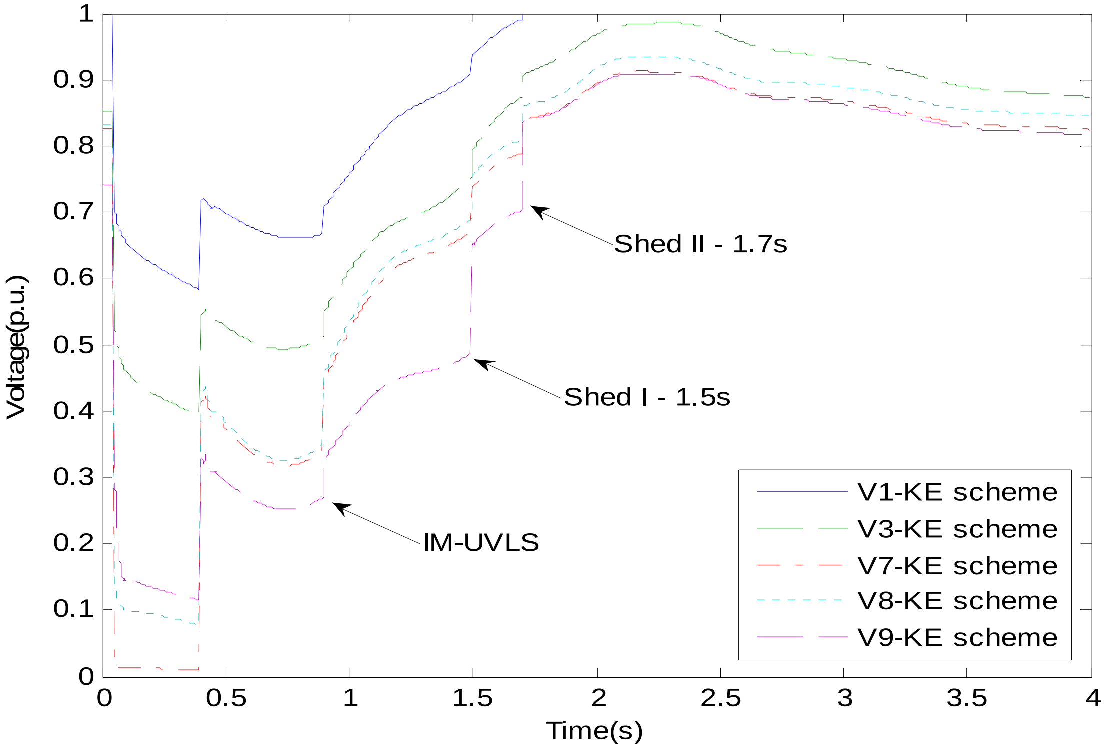

Fig. 7-10. Voltages recovery with IM-UVLS and KE based LSSII

Table 7-2. Results for UVLS and KE based scheme

	Shed time	Shed load	Total shed	V recover
UVLS	1.5s (s1)	92MW (20%)	184 MW	To 0.7 p.u. in 4s
	1.7s (s2)	46MW (10%)		
	1.9s (s3)	46MW (10%)		
KE	1.5s	92MW (20%)	138 MW	To 0.82 p.u. in 4s
scheme	1.7s	46MW (10%)		

Table 7-2 shows that the traditional UVLS shed total load amount of 184 MW without meeting the requirement, but the proposed KE based scheme shed total load amount of 138 MW (25% less) and meet the requirement.

The load shedding results with UVLS relays equipped in three phase motors have further validated that the proposed KE based online demand side control strategy is able to shed much less load and recover system voltage faster comparing to traditional UVLS scheme.

7.4.2 *Impacts of Incorporating Induction Motor UVLS Relay*

Incorporating UVLS relay in three phase motor actually helps the proposed KE deviation based scheme to identify the most effective loads (MEL) to shed , since all the stalling three phase large motors were already tripped by the UVLS relays and thus only the stalling single phase induction motors are still connected to the power grid. Therefore, the complexity of the system load compositions is reduced. It is always easier for the scheme to identify the MELs to shed in the system with single type of induction motors than in the system with multiple types of induction motors.

The impact of incorporating the UVLS relay in large induction motors to our proposed methodology is that the total amount of load shedding by our proposed scheme is less. Since the UVLS relay trips the stalling three phase motor, the fault-induced delayed voltage recovery becomes less severe and thus less loads are needed to be shed for meeting the voltage recovery criterion.

7.5 Load Shedding Comparison between ZIP and Motor Loads

7.5.1 *Motivation*

In practical power systems, both ZIP loads and induction motor loads take large percentages in the entire system loads. ZIP loads are commonly classified as the static load which is composed of constant impedance load, constant current load and constant power load. Induction motor loads are usually considered as dynamic loads whose real power and reactive power consumption vary according to different system operating conditions. In order to practically mitigate FIDVR events in an online environment, it is necessary to evaluate and compare the load shedding effects at ZIP loads and induction motor loads.

As shown in the previous sections in this chapter, the fault location and fault duration time can greatly impact the system voltage recovery process. Also, different fault could make the load shedding effects at ZIP and induction motor loads different. Even though it is known that the FIDVR problem is normally caused by the induction motor stalling phenomenon, it is desired to compare the load shedding results at ZIP and induction motor loads in some particular situations, such as the fault in the location very close to the ZIP load and relatively far away from the induction motor loads.

The sample power system used in Section 6.3.1 is applied as the test system to compare the ZIP and induction motor load shedding effects. A three phase short circuit fault was applied at bus 154 in the test system with fault clearing time of 0.16s. The details of this fault can be found in Appendix B and it is referred as fault 1 in case 1. According to Table 6.1, there are totally 7 load buses, among which only bus 154 and bus 205 do not have any induction motor loads connected. Bus 154 and bus 205 have only ZIP load connected and the percentages of constant impedance, constant current and constant power loads in the ZIP load are 30%, 30% and 40%.

Normally, it is true that the voltage will recover faster when the load is shed at the location closer to the faulted bus. However, it is also recognized that the root cause of FIDVR problem is the motor stalling. Since the applied three phase fault situated right at the bus 154, it will be interesting to compare the load shedding results between ZIP and induction motor loads.

7.5.2 *Load Shedding Effect Comparison between ZIP and Motor Loads*

After the three phase short circuit fault at bus 154 is cleared, it takes 0.7356s for the system voltage to recover to 0.8p.u. and no load shedding action was applied. This system voltage recovery time is measured by the voltage recovery time at the slowest recovery bus 154 and it violated the recovery criterion (see Fig.5-3).

The system loads are classified as three groups to evaluate the load shedding effects. The three groups include ZIP loads, induction motor (IM) loads, and multi induction motor loads. The load shedding actions were applied to each of the three groups at time 0.4s, which is 0.14s after the three phase fault at bus 154 is cleared. After load shedding actions were taken, the system voltage recovery time was derived using time domain simulation. The system voltage recovery time is then used to evaluate the load shedding effect of each load group.

Table 7-3 summarized the time domain simulation based voltage recovery time for shedding total load at different load groups.

Table 7-3. Load shedding effect comparison between ZIP and motor loads

ZIP Loads	no shed		Bus154	Bus205	
Shed Amount	0MW		600MW	1200MW	
Recovery Time(s)	0.736s		0.429s	0.407s	
Motor Loads	Bus153	Bus203	Bus3005	Bus3007	Bus3008
Shed Amount	200MW	200MW	200MW	200MW	200MW
Recovery Time(s)	0.494s	0.478s	0.500s	0.556s	0.553s
Multi Motor Loads	Bus 203&153			Bus 203&153&3005	
Shed Amount	400MW			600MW	
Recovery Time(s)	0.410s			0.401s	

As shown in table 7-3, for ZIP loads (first group), voltage is recovered by 0.429s with 600MW shed at bus 154, by 0.407s with 1200MW shed at bus 205, and by 0.736s with no load shedding.

Regarding the induction motor (second group), the same amount of load (200MW) was shed at each induction motor load bus. After load shedding at each motor bus, the fastest voltage recovery is by 0.478s with load shed at bus 203 and the slowest voltage recovery is by 0.556s with load shed at bus 3007.

By only looking at the voltage recovery time after load shedding, it can be found that the voltage recovered faster with loads shed at ZIP load (0.429s and 0.407s) than that shed at induction motor loads (0.478s as the fastest). However, it should be noticed that the load shedding amount at the ZIP loads are much larger than those at the induction motor loads

(1800MW vs 1000MW). Therefore, the comparable load shedding amount was applied at multiple induction motor loads (third group) to evaluate the voltage recovery time.

As shown in Table 7-3, for multi-motor load case, If loads at buses 203 and 153 are shed (totally 400MW), the voltage recovery time is 0.410s which is smaller than voltage recovery time 0.429s obtained by shedding loads at bus154 (600MW). Similarly, if loads at buses 203, 153 and 3005 are shed (totally 600MW), the voltage recovery time 0.401s is smaller than voltage recovery time 0.407s of shedding loads at bus205 (1200MW).

Using this test case with a three phase fault applied at ZIP load (bus 154), it has been shown that the system voltage recovers faster with the same amount of load being shed at induction motor loads than that shed at ZIP loads. In this test, even though the fault was applied right on the ZIP load bus and thus relatively far away from motor loads, the induction motor loads still show much better load shedding effect than the ZIP loads. Therefore, it can be concluded that the induction motor load is indeed the better candidate than the ZIP loads to be shed for mitigating FIDVR events.

7.5.3 *Evaluate Voltage as an Indicator for FIDVR Mitigation*

Based on the load shedding effect evaluation results, it is also interesting to see whether voltage magnitude can be used as a reliable indicator for selecting loads to be shed to mitigate FIDVR. Fig. 7-11 shows voltage recovery after clearing the three phase fault at bus 154.

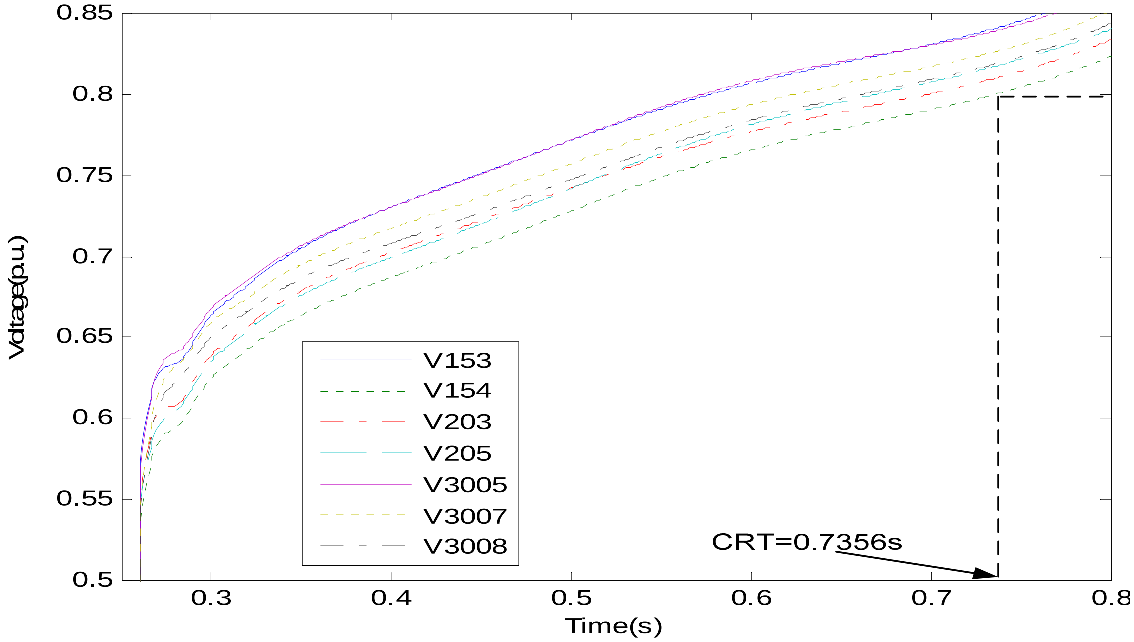

Fig. 7-11. System voltage recovery after fault clearing at bus 154

As shown in Fig. 7-11, the load bus ranking using voltage deviation is 154>205>203>3008>3007>3005>153. Therefore, if bus magnitude is used as the indicator for selecting loads to shed to mitigate FIDVR, load at bus 154 and load at bus 205 will be the top two candidates.

However, compare to the time domain simulation based voltage recovery results shown in Table 7-3, the above bus voltage magnitude based load shedding selections clearly indicate that the bus voltage deviation information is not suitable for identifying the most effective load to shed for FIDVR mitigation.

7.5.4 *KE Deviation as an Indicator for FIDVR Mitigation*

For comparison purpose, the kinetic energy information is also derived here for selecting most effective loads to shed. Figure 7-12 provides the derived KE deviation of each motor load bus using obtained speed deviation and equivalent motor inertia. It shows that the top three buses with the largest KE deviations are buses 203, 153 and 3005 which are identical to the time domain simulation based voltage recovery results shown in Table 7-3.

Thus, it is again shown that motor kinetic energy can properly indicate the most effective loads to shed for FIDVR mitigation.

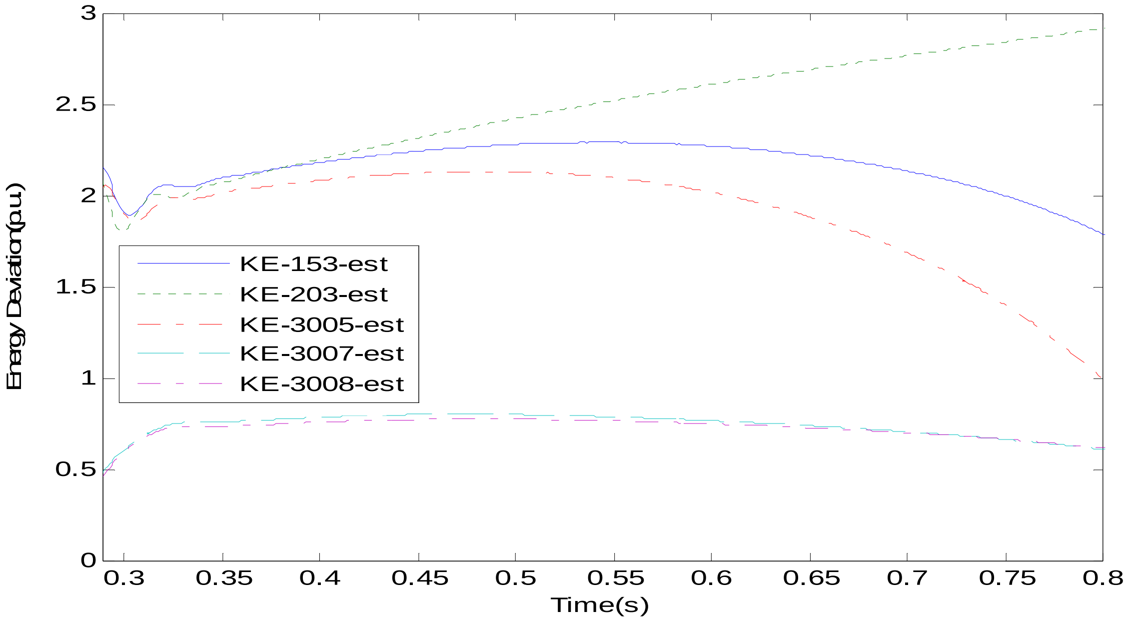

Fig. 7-12. Derived KE deviations after fault clearing at bus 154

7.6 Evaluate Reactive Power Demand as an Indicator for FIDVR Mitigation

In this section, the reactive power consumption of load will be evaluated as an indicator for determining the load shedding location and amout for FIDVR mitigation. The sample power system used in Section 6.3.1 is applied again as the test system to conduct this study.

Generally, the gap between system reactive power demand and supply after a system contingency is the main factor to drive system voltage decreasing or lead to delayed voltage recovery. Also, as shown and discussed in the previous study results of induction motor stalling characteristics, the reactive power consumption could be greatly increased when the low voltage is sustained beyond a certaint time. Therefore, it is necessary to evaluate the effectiveness of using load reactive power demand for FIDVR mitigation.

The applied fault in the test system is the fault 1 in case 1 and the details of this fault can be found in Appendix B. The reactive power demand of all the seven load buses after fault is cleared are plotted in Fig. 7-13. It can be seen that the reactive power demand of the seven load buses can be divided into three groups in term of their reactive power consumption amount. The first group includes loads at bus 154 and bus 205 which have the largest reactive power demands. The second group includes loads at bus 153, bus 3005 and bus 203. The third group includes loads at bus 3008 and bus 3007 which has the smallest reactive power demands. Therefore, if reactive power demand of load is applied as an indicator for choosing load shedding location and amount, the first group (loads at bus 154 and 205) will be the best choice for load shedding in this study case. However, the CRT results of shedding various loads summarized in Table 7-4 indicate that the most effective candidate for load shedding is to shed the combined loads at bus 203, bus 153 and bus 3005. Thus, the time domain simulation based results clearly prove that the load reactive power demand is not proper for identifying the most effective loads to shed to mitigate FIDVR problems.

The main reason for the ineffectiveness of using reactive power demand as an indicator is that reactive power demand is affected by the load amount connected at each load bus and it does not necessarily reflect the gap between reactive power demand and supply. Therfore, shedding loads at the location which has a relatively larger reactive power demand is not as effective as the proposed KE based scheme for mitigating the delayed voltage recovery problem. Also, it has been shown in the section 7.5 that induction motor loads generally are better candidates for load shedding than ZIP loads. In this study case, the loads at bus 154 and bus 205 are pure ZIP loads and the load amounts at these two buses are much larger than the load amounts at those induciton motor loads. Thus, it further proves that the reactive power demand is not an effective indicator for determining the load shedding location and amount for FIDVR mitigation.

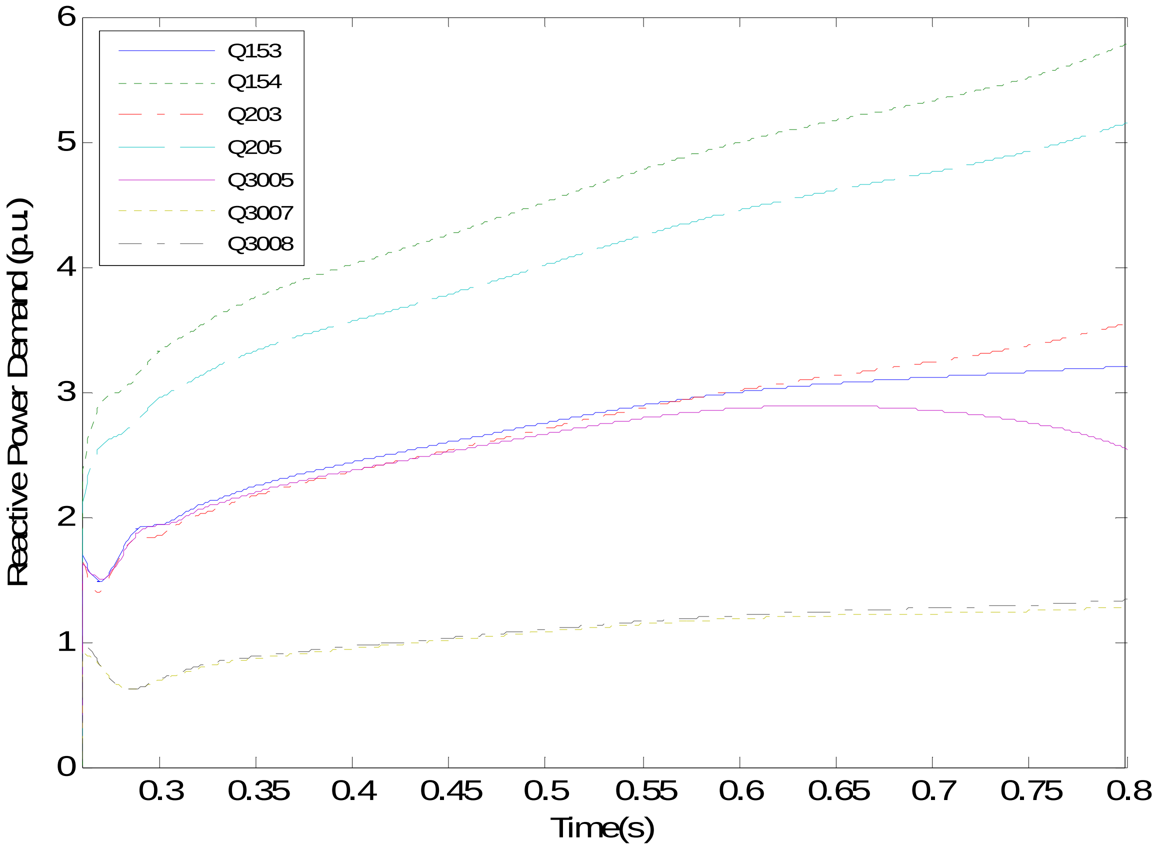

Fig. 7-13. Reactive power demand of each load bus after clearing fault1 in case1

Table 7-4. CRTs of shedding various loads with fault1 in case1

Bus shed	no shed	153	154	203	205	3005
CRT(s)	0.736	0.494	0.429	0.478	0.407	0.500
Bus shed	3007	3008	203&153		203&153&3005	
CRT(s)	0.556	0.553	0.410		0.401	

7.7 Supply Side Response during FIDVR Event

Fault induced delayed voltage recovery is essentially caused by the imbalance between reactive power supply and demand. The stalling induction motor requires 4-6 times its steady state reactive power consumption and drives the generators and SVCs to supply more reactive power to meet the demand. However, all the reactive power compensation devices in the systems are planned according to some preassumed contingency scenarios, and the installed capacity of the devices usually cannot meet the large reactive power demand due to stalling motors. In the previous sections of this dissertation, we have studied the reactive power demand during motor stalling and proposed the demand side control method for mitigating FIDVR problems. In this section, the supply side responses (reactive power generation) during FIDVR event will be presented and analyzed.

The simplified 9-bus test system from ERCOT will be also used here to identify the supply side responses. In this study, the UVLS relay is also equipped in the large induction motors in the system. The three-phase short circuit fault was applied at bus7 and was lasting for 0.4s. The voltage trajectories of all the generator buses and load buses can be seen in Fig. 7-8. The reactive power generation from generators at bus1 and bus3 were presented in Fig. 7-14. It can be seen that the reactive power generation was greatly increased after the fault was applied at 0.05s and was obviously reduced at 0.4s in response to the fault clearing. Then, all the two generators started to increase the reactive power output due to the demand from motors trying to accelerate. At 0.7s, the UVLS relay tripped two large induction motors at bus7 and bus8 since the low voltage has been sustained beyond the threshod, and the reactive power generation was reduced for the seond time in response to this motor tripping. From then on, the voltages of generators and loads began to recover slowly (see Fig. 7-8), and the reactive power output from the two generators also increased trying to accelerate the voltage recovery process. However, both generators at bus1 and bus3 achieved their maximum reactive power output limits at 2s and 2.4s respectively, and their outputs began to decrease after the maximum points (see Fig. 7-14).

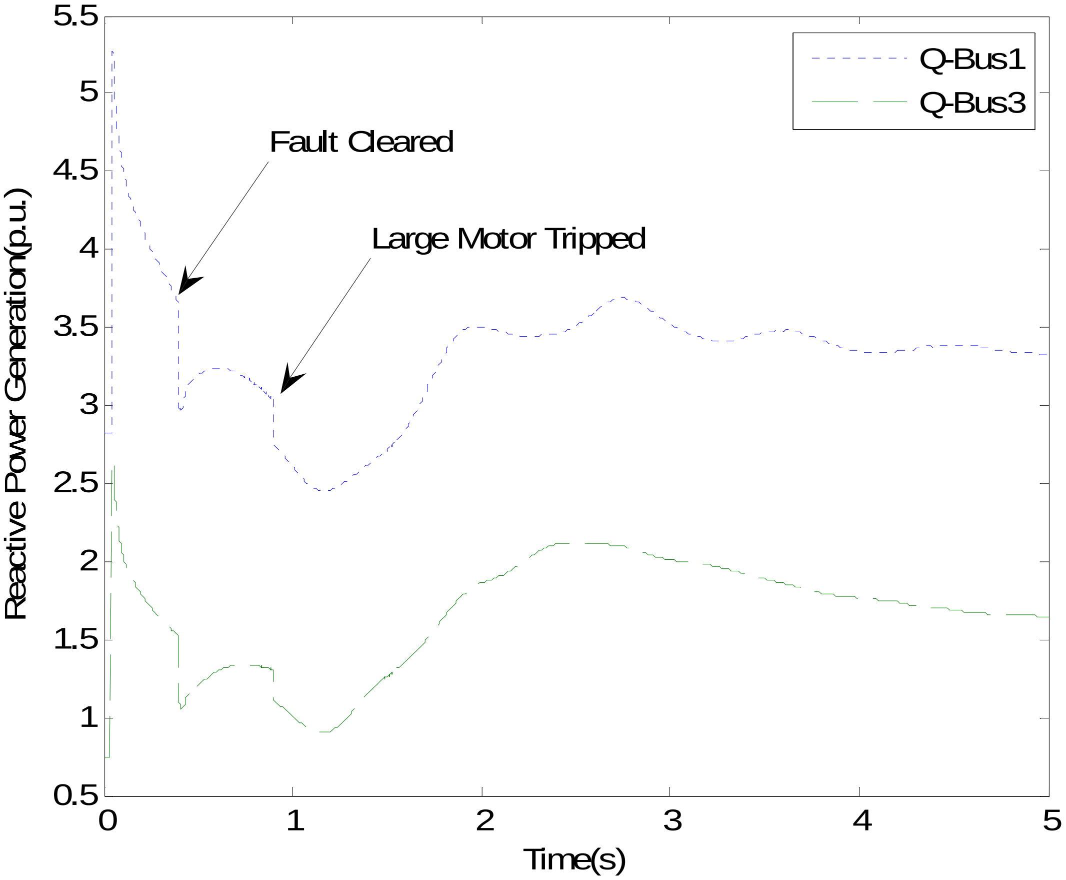

Fig. 7-14. Reactive power generation by generators at Bus1 and Bus3

Supply side responses of the two generators in this test case illustrate that FIDVR events usually follow the phenomenon that system reactive power resources are exhausted. Since stalling motor demands 4-6 times the steady state reactive power and the power system reactive power planning normally does not require this much reserve due to economic concerns, the supply side method alone may not be sufficient to prevent FIDVR events. Therefore, it is necessary and important to develop the demand side method as the last defense of the power system to mitigate FIDVR problem.

7.8 Practical Implementation to Large Power Systems

The proposed load shedding scheme applies a centralized scheme to shed loads at the transmission level. Due to the huge number of motor loads connected to the power grid, it is not practical to monitor each motor load or trip it separately. Therefore, in the proposed scheme, the aggregated load at the transmission substation is monitored and will be tripped when it is necessary.

In practical power systems, it is true that each feeder supplies both static loads and dynamic loads. Since it is not feasible to separate dynamic and static loads under -4one transmission substation of practical power systems, the total load at one transmission substation is treated as an equivalent induction motor in order to evaluate each load bus's contribution in the FIDVR event.

Measurements of the total bus load are used to derive the equivalent motor inertia and motor speed. The derived equivalent motor speed can provide three types of information about the aggregated load at one transmission substation: (1) whether there is induction motor connected at the substation, (2) percentage of the induction motor at the substation, (3) the speed deviation of the equivalent induction motor (aggregated load). In the section 6.5.2, it has been illustrated that the derived speed using total load measurements can indicate the load buses which have no motors at all. These load buses normally are not good candidates for the most effective loads (MEL) to shed. In the section 6.5.3, it has been illustrated that the bus with smaller motor percentage and larger motor speed could have similar equivalent aggregated speed to that of another bus which has larger motor percentage and smaller motor speed. This validates the equivalent motor speed using total load measurement can take into account induction motor percentages. Therefore, equivalent motor kinetic energy deviation calculated based on the derived inertia and speed is used to identify the MEL to shed. By shedding MEL, the time needed for system voltage recovery is the shortest.

In implementation of the proposed online load shedding scheme to a practical power system, the centralized scheme first receives system measurements from relays or system monitoring devices at the transmission substations. Then, MELs are identified based on the derived KE deviation at each transmission substation. Finally, the trip signals are sent out to shed the calculated load amounts at the locations (transmission substations) of MELs. Actually, after the load shedding amount is determined for each transmission substation, the relay will shed the same percentage of load at each distribution feeder under the transmission substation, no matter whether the distribution feeder has motor load connected or not.

7.8.1 *System Monitoring Requirement*

For implementing the proposed online demand side control to large power systems, it is not required to monitor every bus in the system.

Considering the huge number of motor loads connected to the power grid, it is not practical to monitor each motor load or trip it separately. Therefore, in Chapter 6, we proposed to monitor and control the aggregated load at each transmission bus (high voltage level). The derived equivalent motor speed can provide three types of information about the aggregated load at one transmission substation: (1) whether there is induction motor connected at the substation, (2) percentage of the induction motor at the substation, (3) the speed deviation of the equivalent induction motor (aggregated load). After SCADA or EMS collects system measurements, the equivalent motor inertia and speed can be derived using the proposed methods and thus the KE deviation of the aggregated load at each transmission bus can be obtained. Based on this KE deviation information, the load shedding locations and amount at each location can be determined.

Since the delayed voltage recovery problem happens frequently in the areas predominated by motor loads, only a part of the entire transmission system needs to be monitored. Thus, only the measurement data of some transmission substations is needed to be sent to SCADA or EMS for calculating the KE deviation of each monitored transmission bus. Therefore, the data communication will also not be a problem for real-time implementation of the proposed scheme. From the KE derivation process presented in Chapter 6, it can be seen that the KE deviation information can be obtained almost simultaneously after measurement data are received. Therefore, it enables the decisions regarding load shedding locations and amount at each location to be made fast enough for on-line real-time load shedding.

7.8.2 *The Assumption for Practical Implementation*

There is only one assumption regarding the implementation of the proposed method for mitigating FIDVR event in large power systems. The assumption is that "there is no change in load composition between current and previous time". According to reference [59], the time needed for deriving motor inertia is about 1-2 minutes with the hybrid learning algorithm. According to references [7] and [67], the time frame of the load composition change at the transmission level (where the loads served from a large number of distribution transformers are aggregated as an equivalent one) is relatively large. Thus, the time needed for deriving the inertia (1-2 minutes) should be within the time frame of the load composition change at the transmission level. Therefore, this assumption is reasonable for implementing the proposed method to practical power systems.

Based on the above analysis, it can be concluded that the proposed load shedding scheme is practical to be implemented in a large power system.

7.9 Practical Implementation Comparision With Traditional UVLS

The comparisons between the proposed online demand side control strategy and the traditional UVLS scheme in terms of the real-time implementations are provided as follows.

Similar to the traditional four-stage UVLS scheme, the proposed strategy involves multiple steps to shed loads. Also, total amount of load to be shed in each step and time steps are predetermined based on the system requirements.

The main difference between the proposed load shedding scheme and traditional UVLS scheme is that the proposed scheme applies equivalent motor kinetic energy information to identify the most effective locations to shed load and determine the amount of load shedding at each selected location. Another difference is that the proposed scheme applies both the predicted voltage recovery time and voltage level as the conditions to trigger load shedding actions.

Comparing the field implementation, the traditional UVLS scheme just requires installing the UVLS relays in the system with fixed voltage setting and time delay setting. It is indeed very simple to implement. However, it is also because of this simplicity, the traditional UVLS is not effective and efficient to mitigate the FIDVR event as shown in the numerical simulation part in Chapter 6. On the other hand, the proposed scheme requires having one central controller to collect the measurements of each monitored bus, make load shedding decisions based on the calculated kinetic energy information, and send out load shedding signals. However, considering the existing implementations of SCADA and EMS in the practical power systems, the required central controller in our proposed scheme can be substituted with the SCADA. In other words, the proposed scheme can be implemented in the existing SCADA system requiring no additional system monitoring devices or data communication channels.

The proposed scheme only requires traditional load measurements including bus voltage, load real power and load reactive power to derive the kinetic energy deviation information at each monitored bus. Then, the most effective load shedding locations and the load shedding amount at each location can be obtained based on the derived kinetic energy deviation information. As shown in the Section 6.7 of Chapter 6, the proposed scheme can indeed shed much less load to recover the system voltage faster than the traditional UVLS scheme.

Summarizing the advantages of the proposed scheme over the traditional UVLS scheme in mitigating real-time FIDVR events, the proposed scheme can be easily implemented in the existing SCADA system requiring no additional system monitoring devices or data communication channels and it can indeed provide a more effective and efficient way to mitigate FIDVR events by identifying the most effective load shedding locations and the load shedding amount at each location.

CHAPTER 8 CONCLUSION

8.1 Contributions

This dissertation proposes advanced aggregate load modeling and online demand side control techniques that can be applied to mitigate fault-induced delayed voltage recovery in power systems subject to severe disturbances. The proposed methods cover systematic load modeling methodology and efficient load parameter identification technique, and provide a real-time motor kinetic energy derivation scheme and online load shedding strategy to improve power system short-term voltage stability.

The main contributions of the dissertation can be summarized as:

- Systematic methodology is proposed to derive aggregate load models using measurement based approach at the high voltage level (transmission system level). In the absence of precise load information, measurement based approach is preferred since it directly measures dynamic system behavior that can be used to derive accurate load parameters. Thus the systematic methodology including load modeling structure selection, load parameter identification procedure and load parameter search space analysis is important for better load modeling.
- A novel parameter identification technique, hybrid learning algorithm, is proposed for deriving load model parameters. The hybrid learning algorithm combines the genetic algorithm (GA) and the nonlinear Levenberg–Marquardt algorithm. It takes

advantages of the global search ability of GA and the local search ability of Levenberg–Marquardt algorithm, which is a more powerful search technique.

- The mechanism of FIDVR is investigated by studying the stalling characteristics of induction motors and the relationship between FIDVR and motor kinetic energy. Analysis has revealed that motor KE deviation is identical to the integral of power imbalance, which indicates the connection between KE deviations and system transient voltage recovery. A methodology is proposed to obtain equivalent motor inertia and speed through online measurements for motor kinetic energy derivation.
- An online demand side control strategy making use of the motor kinetic energy is proposed to disconnect the stalling motors at the transmission level, which will avoid the large amount of additional reactive power required by stalling motors. Through various validations and comparison with traditional UVLS scheme, the proposed demand side control method has been proven to be an effective and efficient online solution to mitigate FIDVR events.

8.2 Further Research Directions

Further research might be done in a variety of directions based on the proposed research work in the dissertation. Follows summarize some potential research areas.

- Study responses of induction motor based load model (3-phase positive sequence model) to measurements obtained by single phase or two-phase faults.
- Investigate whether it would be beneficial to divide the induction motor model structure into two parts to represent small motors and large motors.

- Design an integrated control scheme which effectively combines both demand side control (shed stalling motors) and supply side control (install reactive power compensations) to mitigate FIDVR events.
- Integrate the proposed load modeling and online demand side control methods into the framework of developing power system smart grid.

APPENDIX A: PARAMETERS OF APPLIED INDUCTION MOTOR MODELS

Load parameters of Motor I and II are listed in Table A-1.

Table A-1. Parameters of the two applied induction motor models

	Motor I	Motor II
Stator resistance - R_s	0.025	0.035
Stator leakage reactance - X_s	0.08	0.094
Magnetizing reactance - X_m	5.0	2.8
Rotor resistance - R_{r1}	0.028	0.048
Rotor leakage reactance - X_{r1}	0.04	0.163
Rotor resistance - R_{r2}	0.07	-
Rotor leakage reactance - X_{r2}	0.03	-
Rotor inertia constant - H	0.28	0.93

APPENDIX B: DETAILS OF THE FOUR FAULTS IN THE THREE TEST CASES

The applied four faults were all three phase bus faults occurred at different buses with different time durations. Details of the four faults are summarized in Table B-1.

Table B-1. Details of the four faults in three test cases

	Faulted bus	Initial time	End time
Case1-fault1	154	0.1s	0.26s
Case2-fault1	152	0.1s	0.3s
Case3-fault1	152	0.1s	0.3s
Case3-fault2	3008&3005	0.1s	0.3s

BIBLIOGRAPHY

[1] C. W. Taylor, Power System Voltage Stability. New York: McGraw-Hill, 1994..

[2] John Diaz de Leon II, and Carson Taylor, “Understanding and Solving Short-term Voltage Stability Problems” Proceedings of the IEEE/PES, 2002 Summer Meeting.

[3] IEEE Task Force on Load Representation for Dynamic Performance, “Load representation for dynamic performance analysis,” IEEE Trans. Power Syst., vol. 8, no. 2, pp. 472–482, May 1993.

[4] Y. Makarov, V. Maslennikov, and D. Hill, “Revealing loads having the biggest influence on power system small disturbance stability,” IEEE Trans. Power Syst., vol. 11, pp. 2018–2023, Nov. 1996.

[5] R. H. Craven, T. George, G. B. Price, P. O. Wright, and I. A. Hiskens, “Validation of dynamic modeling methods against power system response to small and large disturbances,” in Proceedings of CIGRÉ General Session, Paris, Aug. 1994

[6] IEEE Task Force on Load Representation for Dynamic Performance, “Standard load models for power flow and dynamic performance simulation,” IEEE Trans. Power Syst., vol. 10, no. 3, Aug. 1995.

[7] P. Kundur, Power System Stability and Control. New York: McGraw-Hill, 1993.

[8] I. A. Hiskens and J. V. Milanovic, “Load modeling in studies of power system damping,” IEEE Trans, Power syst., vol. 10, no. 4, pp.1781-1788, Nov. 1995.

[9] D. N. Kosterev, C. W. Taylor, and W. A. Mittelstadt, “Model validation for the August 10, 1996 WSCC system outage,” IEEE Trans, Power syst., vol. 14, no. 3, pp. 967-979, Aug. 1999.

[10] W.-S. Kao, C.-J. Lin, C.-T. Huang, Y.-T. Chen, and C.-Y. Chiou, “Comparison of simulated power system dynamics applying various load models with actual recorded data,” IEEE Trans, Power syst., vol. 9, no. 1, pp. 248-254, Feb. 1994.

[11] Load Model Parameter Derivation Based on Measurement, EPRI, Palo Alto, CA: 2006. 1014402.

[12] "Determining load characteristics for transient performances," EPRI EL-849, Vol. 3, Project 849-3, Final report, May 1979.

[13] General Electric Company, “Load Modeling for Power Flow and Transient Stability Computer Studies,” EPRI, Rep., vol. 1-4, Jan. 1987.

[14] Lin, C.-J.; Chen, A.Y.-T.; Chiou, C.-Y.; Huang, C.-H.; Chiang, H.-D.; Wang, J.-C.; Fekih-Ahmed, L., “Dynamic load models in power systems using the measurement approach,” IEEE Trans. Power Syst., vol. 8, Issue 1, pp. 309–315, Feb. 1993.

[15] O. Nelles, Nonlinear System Identification: From Classical Approaches to Neural Networks and Fuzzy Models. Germany: Springer, 2001.

[16] P. Shackshaft, et al., “General purpose model of power system loads,” Proc. IEE, vol. 124, pp. 715-723, 1977.

[17] Q. S. Liu, Y. P. Chen, D. F. Duan, “The Load Modeling and Parameter Identification for Voltage Stability Analysis,” Proc. Int. Conf. Power System Technology, 2002, pp. 2030–2033.

[18] I. A. Hiskens, “Nonlinear Dynamic Model Evaluation from Disturbance Measurements,” IEEE Trans. Power syst., vol. 16, no. 4, pp. 702-710, Nov. 2001.

[19] V. Knyazkin, C. Caizares, and L. Sder, “On the Parameter Estimation and Modeling of Aggregate Power System Loads,” IEEE Trans, Power syst., vol. 19, no. 2, pp. 1023-1031, May. 2004.

[20] P. Jazayeri, W. Rosehart, D. T. Westwick, “A Multistage Algorithm for Identification of Nonlinear Aggregate Power System Loads,” IEEE Trans. Power Syst., vol. 22, pp. 1072 - 1079, Aug. 2007.

[21] S. Z. Zhu, J. H. Zheng, S. D. Shen, G. M. Luo, “Effect of load modeling on voltage stability,” IEEE Power Engineering Society Summer Meeting, vol. 1, pp. 395 – 400, 2000.

[22] S. Kamoun and R. P. Malham6, “Convergence characteristics of a maximum likelihood load model identification scheme,” Automatica, vol. 28, no. 5, pp. 885-896, Sept. 1992.

[23] J. A. de Kock, F. S. van der Merwe, H. J. Vermeulen, “Induction Motor Parameter Estimation through an Output Error Technique,” IEEE Trans, Energy Conv., vol. 9, no. 1, pp. 69-76, Mar. 1994.

[24] J. T. Ma and Q. H. Wu, “Generator parameter identification using evolutionary programming,” Int. J. Electr. Power Energy Syst., vol. 17, no. 6, pp. 417-423, 1995.

[25] D. Karlsson, D. J. Hill, “Modeling and identification of nonlinear dynamic loads in power systems,” IEEE Trans. Power Syst., vol. 9, pp. 157 - 166, Feb. 1994.

[26] T. Hiyama, M. Tokieda, W. Hubbi, “Artificial Neural Network Based Dynamic Load Modeling,” IEEE Trans. Power Syst., vol. 12, no. 4, pp. 1576-1583, Nov. 1997.

[27] H. Renmu, M. Jin, D. J. Hill, “Composite load modeling via measurement approach,” IEEE Trans. Power Syst., vol. 21, pp. 663–672, May 2006.

[28] P. Ju, E. Handschin, D. Karlsson, “Nonlinear Dynamic Load Modeling: Model and Parameter Estimation,” IEEE Trans, Power syst., vol. 11, no. 4, pp. 1689-1697, Nov. 1996.

[29] J. Y. Wen, L. Jiang, Q. H. Wu, S. J. Cheng, “Power system load modeling by learning based on system measurements,” IEEE Trans. Power Deli., vol.18, no. 2, pp. 364–371, Apr. 2003.

[30] S. Zhu, Z. Dong, K. P. Wong, and Z. Wang, “Power system dynamic load identification and stability,” in Proc. Int. Conf. Power System Technology, Dec. 2000, pp. 13-18.

[31] A. Gebreselassie and J. H. Chow, “Investigation of the effects of load models and generator voltage regulators on voltage stability,” Int. J. Elect. Power Energy Syst., vol. 16, no. 2, pp. 83-89, 1994.

[32] D. Kosterev, B. Mittelstadt, M. Viles, B. Tuck, J. Burns, M. Kwok, J. Jardim, and G. Garnett. Model Validation and Analysis of WSCC System Oscillations following Alberta Separation on August 4, 2000. Final Report, January 2001.

[33] D. E. Goldberg, Genetic Algorithms in Search, Optimization and Machine Learning. Reading, MA: Addison-Wesley, 1989.

[34] N. Krasnogor and J. E. Smith, “A tutorial for competent memetic algorithms: Model, taxonomy, and design issues,” IEEE Trans. Evol. Comput., vol. 9, no. 5, pp. 474–488, Oct. 2005.

[35] K. Deb and T. Goel, “A hybrid multi-objective evolutionary approach to engineering shape design,” in Proc. 1st Int. Conf. Evolutionary Multi-Criterion Optimization, Zurich, Switzerland, Mar. 2001, pp. 385–399.

[36] D. Marquardt, “An algorithm for least-squares estimation of non-linear parameters,” J. Soc. Ind. Appl. Math., vol. 11, pp. 431-441,1963.

[37] U. S. Department of Energy Workshop, "On the Role of Residential AC Units in Contributing to Fault-Induced Delayed Voltage Recovery," Westin Dallas Fort Worth Airport, April 22, 2008.

[38] NERC transmission issues subcommittee, “NERC planning committee White Paper of Delayed Voltage Recovery – Cause, Risk and Mitigation,” March 18, 2009.

[39] B. R. Williams, W. R. Schmus, and D. C. Dawson, “Transmission voltage recovery delayed by stalled air conditioner compressors,” IEEE Trans. Power Syst., vol. 7, no. 3, pp. 1173–1181, Aug. 1992.

[40] G. K. Stefopoulos and A. P. Meliopoulos, “Induction motor load dynamics: Impact on voltage recovery phenomena,” in Proc. IEEE Power Eng. Soc. General Meeting, Jun. 2006.

[41] I. A. Hamzah and J. A. Yasin, “Static var compensators (SVC) required to solve the problem of delayed voltage recovery following faults in the power system of the

saudi electricity company, western region (SEC-WR),” in Proc. 2003 IEEE PowerTech Conf., Italy, Jun. 23–26, 2003.

[42] L. Y. Taylor and S.-M. Hsu, “Transmission voltage recovery following a fault event in the metro Atlanta area,” in Proc. IEEE Power Eng. Soc. Summer Meeting, Jul. 2000.

[43] L. Y. Taylor, R. A. Jones, and S. M. Halpin, “Development of load models for fault induced delayed voltage recovery dynamic studies,” in Proc. IEEE Power Eng. Soc. General Meeting, Jul. 2008.

[44] P. Pourbeik and B. Agrawal, “A hybrid model for representing air-conditioner compressor motor behavior in power system studies,” in Proc. IEEE Power Eng. Soc. Summer Meeting, Jul. 2008.

[45] V. Stewart and E. H. Camm, “Modeling of stalled motor loads for power system short-term voltage stability analysis,” in Proc. IEEE Power Eng. Soc. General Meeting, Jun. 2005.

[46] G. Chinn, “Modeling Stalled Induction Motors,” in Proc. of 2006 PES Transmission and Distribution Conference and Exhibition, Dallas, TX.

[47] C. D. Vournas and G. A. Manos, “Modeling of stalling motors during voltage stability studies,” IEEE Trans. Power Syst., vol. 13, No. 3, pp. 775–781, Aug. 1998.

[48] S. M. Halpin, K. A. Harley, R. A. Jones, and L. Y. Taylor, “Slope-permissive under-voltage load shed relay for delayed voltage recovery mitigation,” IEEE Trans. Power Syst., vol. 23, No. 3, pp. 1205–1210, Aug. 2008.

[49] S. M. Halpin, R. A. Jones, and L. Y. Taylor, “The MVA-Volt index: a screening tool for predicting fault-induced low voltage problems on bulk transmission systems,” IEEE Trans. Power Syst., vol. 23, No. 3, pp. 1205–1210, Aug. 2008.

[50] N. Lu, B. Yang, Z. Huang, and R. Bravo, “The system impact of air conditioner under-voltage protection schemes,” in Proc. IEEE Power Eng. Soc. General Meeting, Jul. 2009.

[51] D. Sullivan, et al., “Managing fault-induced delayed voltage recovery in metro Atlanta with the Barrow County SVC,” in Proc. IEEE Power Eng. Soc. General Meeting, Jul. 2009.

[52] A. P. S. Meliopoulos, G. Cokkinides, and G. Stefopoulos, “Voltage stability and voltage recovery: Load dynamics and dynamic VAR sources,” in Proc. IEEE Power Eng. Soc. General Meeting, Jun. 2006.

[53] D. Sullivan, et al., “Design and Application of a Static VAR Compensator for Voltage Support in the Dublin, Georgia Area,” in Proc. of 2006 PES Transmission and Distribution Conference and Exhibition, Dallas, TX.

[54] A. H. Al-Mubarak, S. M. Bamsak, et al., “Preventing voltage collapse by large SVCs at power system faults,” in Proc. IEEE Power Eng. Soc. General Meeting, Jul. 2009.

[55] M. Du, M. Han, Z. Cao, F. Chu, and M. EI-kady, “Utilizing STATCON to resolve delayed voltage recovery problem in SEC-WR,” in Proc. IEEE Power Eng. Soc. General Meeting, Jul. 2009.

[56] J. Machowski J. W. Bialek, and J. R. Bumby, Power System Dynamics and Stability, John Wiley Press, 1997.

[57] M. Connolly, "Center point energy", FERC Technical Conference on Principles for Efficient and Reliable Reactive Power Supply and Consumption, March 8, 2005.

[58] PJM Transmission Planning Department, "EXELON Transmission Planning Criteria", March 11, 2009.

[59] H. Bai, P. Zhang, V. Ajjarapu, “A Novel Parameter Identification Approach via Hybrid Learning for Aggregate Load Modeling,” IEEE Trans. Power Syst., vol. 24, No. 3, pp. 1145–1154, Aug. 2009.

[60] J. Ma, D. Han, R. M. He, Z. Y. Dong and D. J. Hill, “Reducing identified parameters of measurement-based composite load model,” IEEE Trans. Power Syst., vol. 23, No. 1, pp. 76–83, Feb. 2008.

[61] I. A. Hiskens and M. A. Pai, “Trajectory sensitivity analysis of hybrid systems—part I : Fundamental theory and applications,” IEEE Trans. Circuit Syst., vol. 47, no. 2, pp. 204–220, Feb. 2000.

[62] I. A. Hiskens and J. Alseddiqui, “Sensitivity, approximation, and uncertainty in power system dynamic simulation,” IEEE Trans. Power Syst., vol. 21, no. 4, pp. 1808–1820, Nov. 2006.

[63] M. Begovic, et al., “Summary of System Protection and Voltage Stability,” IEEE Trans. Power Delivery, vol. 10, No. 2, pp. 631-637, April 1995.

[64] J. W. Shaffer, “Air conditioner response to transmission faults,” IEEE Trans. Power Syst., vol. 12, No. 2, pp. 614–619, May 1997.

[65] ANSI/IEEE Std 242-1986, "American National Standard IEEE Recommended Practice for Protection and Coordination of Industrial and Commercial Power Systems".

[66] *ERCOT Transient Voltage Security Criteria Development (Part I)*, ERCOT DYNAMICS WORKING GROUP, September 9, 2003.

[67] Willis, H.L., Power Distribution Planning Reference Book, 2004, Marcel Dekker, Chapter 2,3, pp 47-102.

[68] Bahram Amin, Induction Motors: Analysis and Torque Control, 2002, Springer, Chapter 5.3, pp 96-102.

ACKNOWLEDGEMENTS

First and foremost I offer my sincerest gratitude to my supervisor, Dr. Venkataramana Ajjarapu, who has supported me throughout my Ph.D. study with his patience and knowledge whilst allowing me the room to work in my own way. I attribute the level of my Ph.D. degree to his encouragement and effort and without him this dissertation, too, would not have been completed or written. One simply could not wish for a better or friendlier supervisor.

I would like to acknowledge my committee members, Dr. Chen-Ching Liu, Dr. Manimaran Govindarasu, Dr. Li-Zhi Wang and Dr. John R. Schroeter for their encouragements, insightful comments and all the contributions to this work.

I am grateful to all my friends in Iowa State University for helping me get through the difficult time, and for all the emotional support, entertainment, and caring they provided.

Most importantly, I wish to thank my grandparents, Gonghu Pan and Li Gong, my parents, Xueshan Bai and Weihong Pan. They bore me, raised me, supported me, taught me, and loved me. To them I dedicate this dissertation.

Lastly, I want to thank my wife, Katie Dou for her patience, understanding, encouragement, and love. If I wrote down everything I ever wanted in a wife and best friend, I would not have believed I could meet someone better.